5-2005

Motion Control for a Tracking Fluoroscope System

Gabriel Rinaldo Preliasco
University of Tennessee - Knoxville

Recommended Citation

Preliasco, Gabriel Rinaldo, "Motion Control for a Tracking Fluoroscope System. " Master's Thesis, University of Tennessee, 2005.
https://trace.tennessee.edu/utk_gradthes/2295

To the Graduate Council:

I am submitting herewith a thesis written by Gabriel Rinaldo Preliasco entitled "Motion Control for a Tracking Fluoroscope System." I have examined the final electronic copy of this thesis for form and content and recommend that it be accepted in partial fulfillment of the requirements for the degree of Master of Science, with a major in Mechanical Engineering.

William R. Hamel, Major Professor

We have read this thesis and recommend its acceptance:

Richard Komistek, G. V. Smith

Accepted for the Council:
Carolyn R. Hodges

Vice Provost and Dean of the Graduate School

(Original signatures are on file with official student records.)

To the Graduate Council:

I am submitting herewith a thesis written by Gabriel Rinaldo Preliasco entitled "Motion control for a tracking fluoroscope system." I have examined the final electronic copy of this thesis for form and content and recommend that it be accepted in partial fulfillment of the requirements for the degree of Master of Science, with a major in Mechanical Engineering.

William R. Hamel
Major Professor

We have read this thesis
and recommend its acceptance:

Richard Komistek

G. V. Smith

Accepted for the Council:

Anne Mayhew
Vice Chancellor and
Dean of Graduate Studies

(Original signatures are on file with official student records.)

Motion control for a tracking fluoroscope system

A Thesis
Presented for the
Master of Science
Degree
The University of Tennessee, Knoxville

Gabriel Rinaldo Preliasco
May 2005

To my parents,
wife,
family,
friends,
and country

Acknowledgments

First of all, I would like to thank the organizations and people that made truth my dream of doing my graduate studies here, my second home. I would like to thanks Senator J. William Fulbright, who had the outstanding idea of an international exchange program for the hopeful of the human kind trough the mutual understanding between people from different countries. This program, that took his name, was established in 1946 after the Second World War. Thanks to the U.S. department of State and the Uruguayan government to keep this bilateral exchanges program real. Specially thanks to the Organization of American States for its trust and extraordinary economic support. Thanks to the American Society of Mechanical Engineers Auxiliary for their support with The Rice-Cullimore Scholarship. Finally, special thanks to Dr. William R. Hamel, who in March of 2003, before I got the OAS and the ASME scholarships, wrote a recommendation letter to the Mechanical, Aerospace and Biomedical Engineering Department, which offered me a graduate assistantship that made it possible for me to study at the University of Tennessee.

Secondly, I would like to thank all the people that helped me in this research; my advisor Dr. William Hamel for his guidance not only in my thesis but in my professional career too, Dr. Jeffrey Freeman for his collaboration in the dynamic models, Dr. David K. Irick for his time and cooperation. Thanks to Rinaldo Preliasco and Roberto Gimenez for their help, time and points of views. I want to specially thank Dennis W. Higdon, who continuously guided and taught me the electrical concepts I required for the development of this research. Finally, thanks to all people who worked in this research: Fie Liu, Dr Sewoong Kim, and especial thanks to Brad Cunningham for his continuous cooperation in the research and reading this thesis. I want to express my gratefulness to Dr Richard Komistek and Dr William Hamel who trusted on me for this research.

Finally, thanks Jesus Christ, God, since without you nothing would be possible.

Abstract

The tracking fluoroscope system (TFS), patent pending serial No.: 60/606,480; is a vehicle carrying a fluoroscope to take x-rays movies of person's joints. Fluoroscope, composed by a radiation source and image intensifier, is moved by a total of four servomotors following a subject's joint. At the same time, vehicle has to follow the subject using two driving-steering servomotor wheels. This thesis is the result of internal research developed at the Mechanical Aerospace Biomedical Engineering Department at the University of Tennessee.

The thesis objective is to determine the best control system for TFS subject tracking function in linear translational mode. Kinematic and dynamic models of the system are presented. The kinematic and dynamic control systems are simulated, tested, and compared. A simplified dynamic model is introduced to compare its results with the kinematic model and evaluate if an extensive dynamic model is required. The dynamic model incorporates a tire friction model. Various tests are then carried out to compute the tire model parameters. To overcome some disadvantages presented by the dynamic and kinematic control systems, a stand-off distance controller is introduced and tested. The stand-off distance controller exhibits better performance than the other control systems proposed. Finally, a special setup process is developed and tested to rotate the vehicle in place.

Index

List of tables

List of figures

Nomenclature

CG	center of gravity, also designated as GC
D	stand-off distance or tracking error distance; motor load drag coefficient
DS1	driving servomotor of wheel 1
DS3	driving servomotor of wheel 3
F''_{1F} , F''_{2F} , F''_{3F} , F''_{4F}	Forward Friction/Traction Forces on each wheel
F''_{1L} , F''_{2L} , F''_{3L} , F''_{4L}	Lateral Friction Forces on each wheel
F'_{1F} , F'_{2F} ,F'_{3F} , F'_{4F}	Friction Forces on each wheel in the direction of x_{rel}
F'_{1L} , F'_{2L} ,F'_{3L} , F'_{4L}	Friction Forces on each wheel in the direction of y_{rel}
Ff	forward coordinate of wheel 3 in the relative frame
FGC	forward coordinate of center of gravity in the relative frame
F_N	normal force at wheel
Fr	forward coordinate of wheel 1 in the relative frame; wheel friction force
F_X, F_Y	Resultant friction forces expressed in the absolute frame
ICR	instantaneous center of rotation or curvature ICC
I_{GC}	platform moment of inertia at the center of gravity in the Z_{rel} direction
J	total inertia seen by motor
K_e	motor electromotive constant
K_t	motor torque constant
Lf	lateral coordinate of wheel 3 in the relative frame
LGC	lateral coordinate of center of gravity in the relative frame
Lr	lateral coordinate of wheel 1 in the relative frame
L_a	motor armature inductance
P	platform position, subject desired position
R	distance from ICR to point P
R1	distance from ICR to wheel 1
R3	distance from ICR to wheel 3

R_a	motor armature resistance
SS1	steering servomotor of wheel 1
SS3	steering servomotor of wheel 3
T	motor shaft torque
T	motor torque after gear box
T_{ext}	motor external friction torque
V	wheel velocity in its longitudinal direction
V_a	input motor armature voltage
V_{emf}	back electromotive force
X, Y	platform coordinates, P, in the absolute frame
X_{abs}	absolute X-axis, fixed to the room
X_{GC}, Y_{GC}	center of gravity coordinates in the absolute frame
X_{rel}	relative X-axis, fixed to the platform frame, forward direction
Y_{abs}	absolute Y-axis, fixed to the room
Y_{rel}	relative Y-axis, fixed to the platform frame, lateral direction
Z_{rel}	relative Z-axis, fixed to the platform frame, normal to the ground
d1	wheel 1 traveled distance in platform rotation
d3	wheel 3 traveled distance in platform rotation
i_a	motor armature current
k	vector normal to the ground
m	platform mass
r	gear box ratio
r_{P1}	vector from P to wheel 1
r_{P3}	vector from P to wheel 3
s	wheel slip
u	absolute platform forward velocity expressed in the relative frame
v	platform translational speed (kinematic model); absolute platform lateral velocity expressed in the relative frame (dynamic model)
v1	driving speed of wheel 1

v_{1X}	component of v1 in the direction of X_{rel}
v_{1Y}	component of v1 in the direction of Y_{rel}
v3	driving speed of wheel 3
v_{3X}	component of v3 in the direction of X_{rel}
v_{3Y}	component of v3 in the direction of Y_{rel}
v_r	wheel-platform relative velocity
v_R	relative velocity between subject and platform
α	subject-platform angle, orientation error
$\alpha 1$	steering angle of wheel 1
$\alpha 2$	steering angle of wheel 2
$\alpha 3$	steering angle of wheel 3
$\alpha 4$	steering angle of wheel 4
β	angle between X_{rel} and vector wheel1-wheel3
γ	platform rotation angle
$\varphi 1$	angle traveled by wheel 1 when doing distance d1
$\varphi 3$	angle traveled by wheel 3 when doing distance d3
θ	platform rotation angle, yaw angle
$\theta 1$	angle between X_{rel} and r_{P1}
$\theta 3$	angle between X_{rel} and r_{P3}
ρ 3	distance from ICR to wheel 3
$\rho 1$	distance from ICR to wheel 1
ω	platform rotation speed or yaw rate angular; motor shaft speed; angular wheel speed

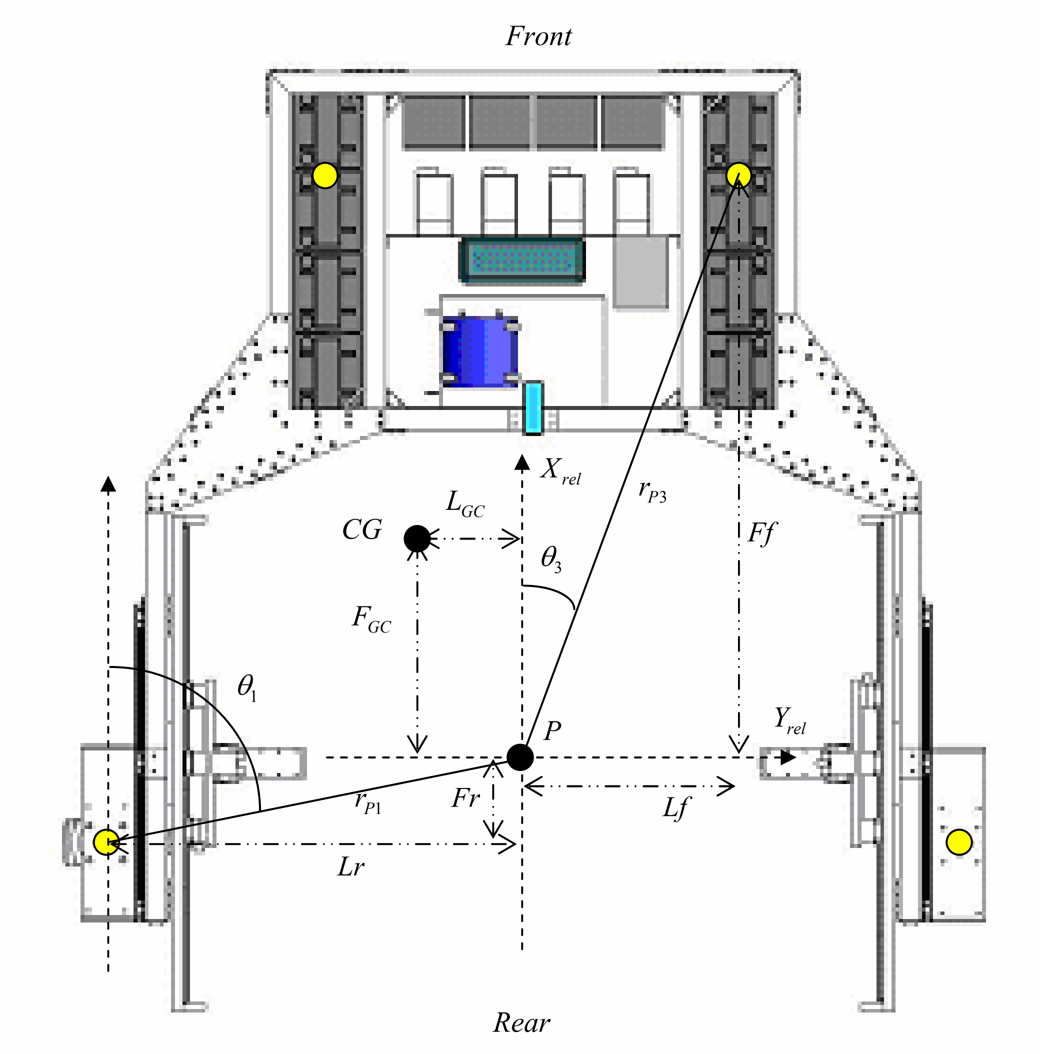

Figure xvii.1 Nomenclature definition

Chapter 1. Introduction

The tracking fluoroscope system, TFS, is a first time device that takes X-ray images of knee, ankle or hip while a subject walks in a common surface. The TFS is designed to follow the subject and take its joint images in any common surface. It can run over inclined surface, trough 3-4 step staircases with an actual maximum speed of 2 m/s. With some motor and structural modifications it would go up to 10 m/s or more.

The TFS will let biomedical researches to investigate, study, and analyze human movements in a common surface. Studies can be made in various surfaces with different hardness and then diverse impact conditions. Lateral and front views of the human joints will be taken at frequencies of about or over 30 Hz. Those movies will make it possible to see patient joint movements, rotation angles, speeds, and accelerations. Subsequently, by Kane's dynamics calculate forces at each joint to better design joint implants. Not only limited to that, it can also be used to test athletes' movements to see for example the efficacy of sport equipments that reduce joint impact.

The TFS, is compounded by an x-ray device that take the images, two vertical tables moved by 2 rotary and 2 linear servomotors designed to carry the x-ray emitter and intensifier, a PC controller, and a moving platform that carries all these elements following a subject.

The platform is moved by two motor-in-wheel-drives with integrated steering unit. Thus, platform can move in any direction over a plain surface, and then follow a subject in free motion mode. To follow a person over a straight line it only needs a distance sensor as main feedback. To do that in any direction, the platform will need to include a laser sensor scanner or similar device to measure distance and subject orientation. In lack of such device, this thesis deals with lateral and forward translational modes. However, the kinematic approach to control the platform in free motion mode is still presented.

Platform can be controlled either by kinematic or dynamic algorithms. Wheeled mobile robots control algorithms have been previously addressed. Dynamic and kinematic control algorithms have been implemented, and kinematic implementations are preferred. The special characteristics of this research make it difficult to apply the dynamic and kinematic algorithms developed in the literature to the TFS. The TFS weights 1000 pounds supported by two caster wheels and the two motor-in-wheel-drives previously mentioned. Besides, the two motor-in-wheel-drives are placed in diagonal positions, architecture not addressed yet. Furthermore, the control techniques used in the literature are being applied to small-wheeled mobile robots focus in path following cases instead of subject tracking.

This thesis tries to address, from the very basic kinematic and dynamics, the best control scheme to reduce the settling time and steady state tracking error for the TFS. Finally, this thesis will develop, simulate and test the kinematic and dynamic control systems for TFS subject tracking function.

Chapter 2. Platform kinematic and dynamic models

This chapter is divided in four sections. In the first part of the chapter the driving system is described, and then three study cases are established depending on the subject-walking pattern. In the second part of the chapter, the kinematic study of the moving platform is presented for each of the mentioned cases. The third section of the chapter deals with the dynamic model of the platform. Finally, platform setup is described.

2.1 DESCRIPTION OF DRIVING SYSTEM

Several devices compose a tracking fluoroscope system, TFS. A complete description of the TSF is given in chapter 6. This section gives a brief introduction to the subject tracking system. Subsequently, three cases of study that depend on the subject-platform moving configuration are presented. Figure 2.1 shows a general view of the subject and platform.

The platform has a prismatic structure in its front to carry the main processing unit, motor amplifiers, and power units. The fluoroscope components, emitter and image intensifier, are mounted on 2 XZ tables placed in platform lateral sides, which are moved by 2 linear and 2 rotary servomotors. Finally, platform moves with the help of two caster wheels and two Schabmüller motor-in-wheel-drive wheels. Each powered wheel is omni-directional with two servomotors, one for driving and one for steering capabilities. Figure 2.2 is a bottom view of the platform, showing the caster wheels and the servomotors.

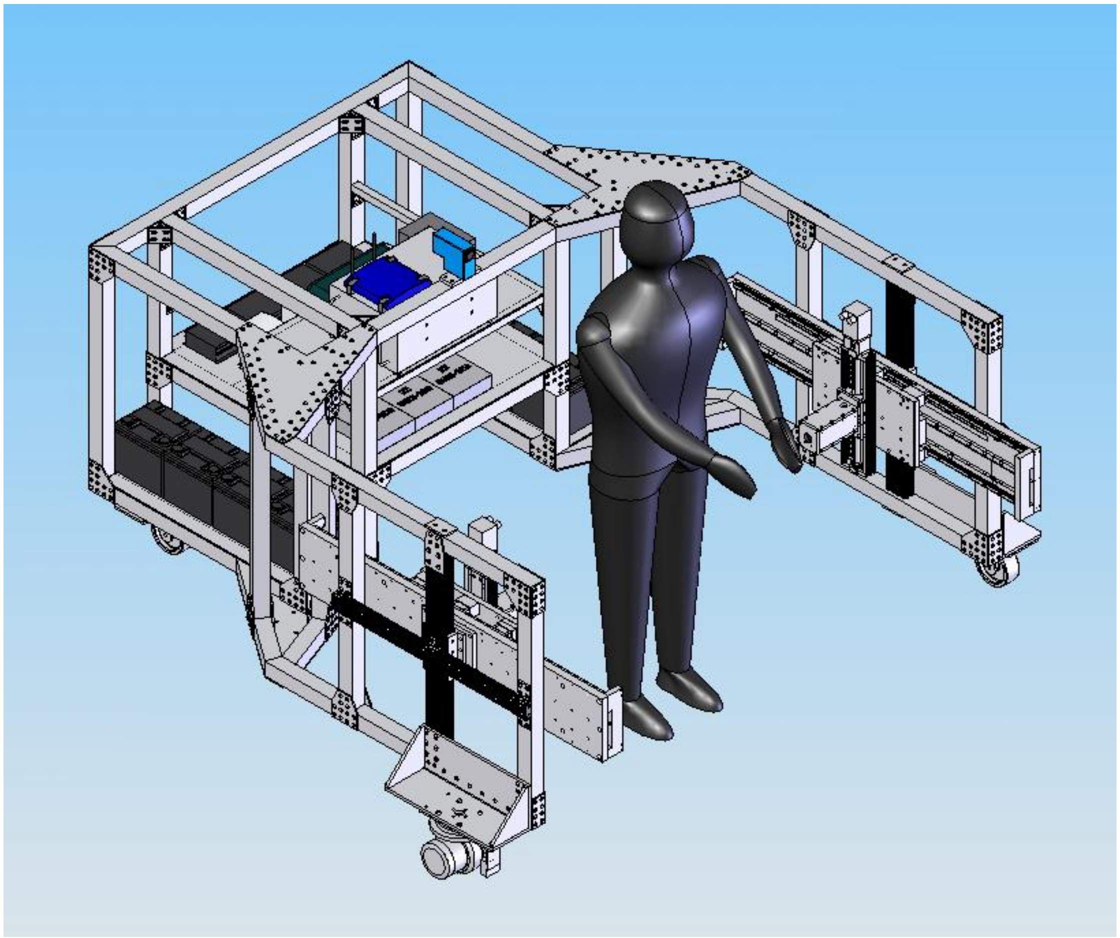

Figure 2.1 Tracking Fluoroscope Systems

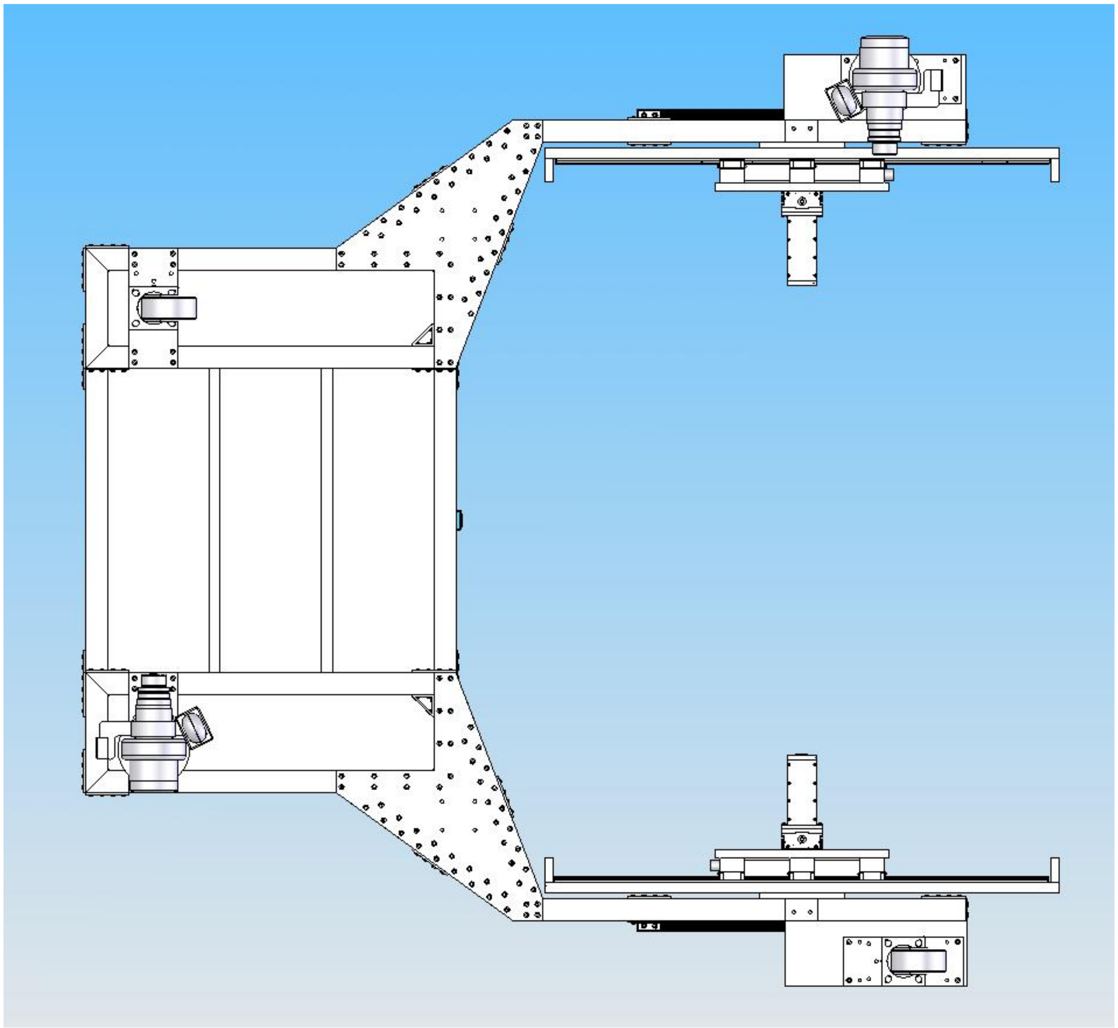

Figure 2.2 Platform bottom view

To set a reference, looking the platform from the top view, wheels are going to be numerated in a clockwise direction as showed in Figure 2.3. Point P, in Figure 2.3, is defined as the platform position point. Point P is a virtual platform point, fixed to the platform and distant to any other platform point by constant distance. This location is equally distanced from left and right XZ tables, and it is in the middle of the X linear servomotor way. Besides, point P is the best place where the subject could be, to take the X-ray image. Therefore, platform position, P, is also defined as the subject desired position.

Subject real position is represented in Figure 2.3 as point H. Since the platform must follow the subject, then the control scheme objective is to move the platform from point P to point H, making platform position the same as subject position. Distance between H and P is the tracking error distance that must be controlled to 0 by the tracking control system.

Figure 2.4 defines the platform relative frame fixed to the platform and placed at P. Platform movements in the x-direction are considered reverse and forward movements. In the same way, platform movements in the y-direction are considered lateral left and right movements. Three cases are going to be studied depending on the subject path and subject-platform orientation.

CASE 1: FORWARD TRANSLATIONAL MODE

In the first case the subject walks in a straight line in the X-axis direction. Subject and platform have the same orientation, as showed by Figure 2.5 This backward/forward platform movement, for simplicity is called forward translational mode without any restriction on the walking direction, backward or forward.

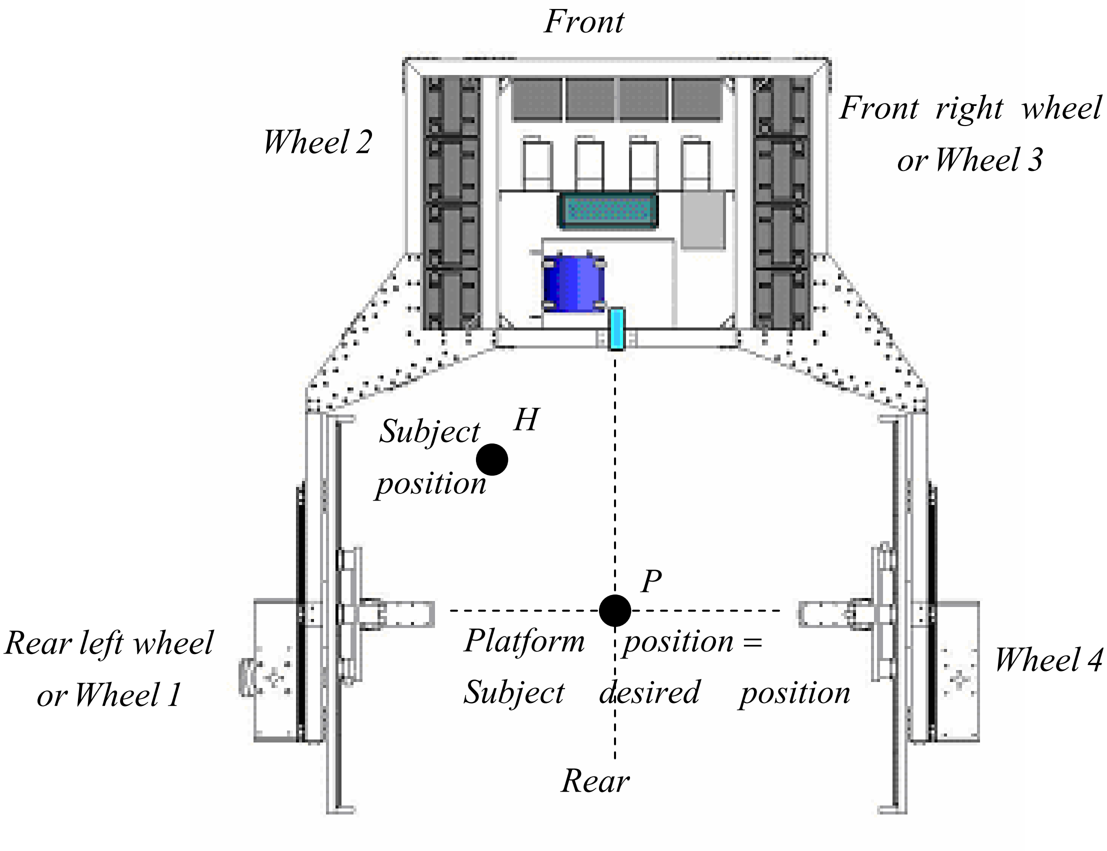

Figure 2.3 Platform top view

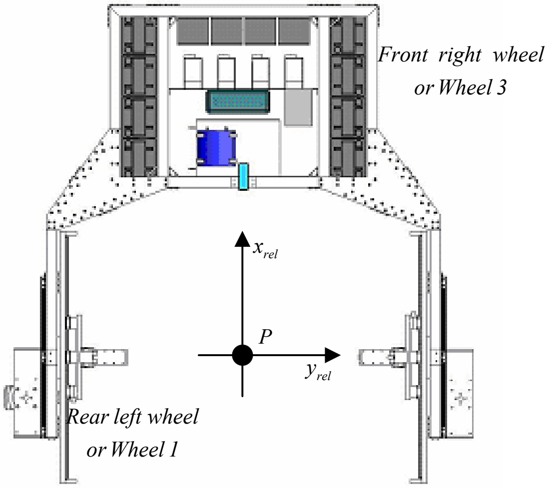

Figure 2.4 Platform relative frame

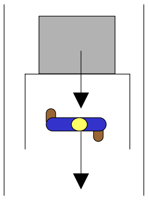

Figure 2.5 Case 1: forward translational mode

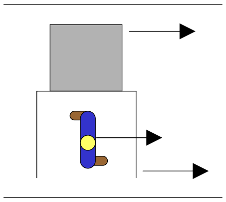

Figure 2.6 Case 2: lateral translational mode

CASE 2: LATERAL TRANSLATIONAL MODE

In the second case the subject also walks in a straight line. However, the platform and subject orientations are perpendicular, as showed by Figure 2.6. In this case, the subject walks in the direction of the Y-axis, left/right movement. The platform has to follow her/him maintaining the constant stand-off distance, and the 90 degrees orientation. This case has nearly the same control scheme of the first case, but with platform wheels home positions rotated 90 degrees relative to the vehicle frame.

CASE 3: FREE MOTION MODE

Finally in the third case the platform must follow the subject in any arbitrary direction while maintaining the same orientation, and stand-off distance with respect to the subject subject. Figure 2.7 exemplifies this case.

The control system must be capable of smoothly following the subject in any direction. Then, as the subject walks at different speeds and directions, the platform must also maintain desired stand-off distances between the lateral and front side of the platform. Since the system is intended to image body joints, it is very important to

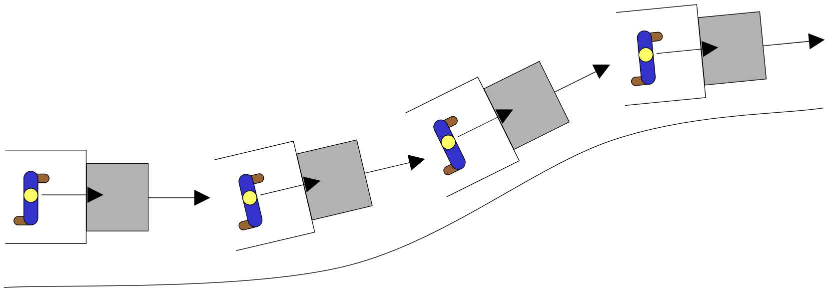

Figure 2.7 Case 3: free motion mode

keep the platform orientation error as low as possible. To assure that the X-ray line of sight remains essentially fixed with respect to the subject.

The first and second cases are comparatively straightforward control schemes compared to the third case, assuming drive wheel slipping and measured subject orientation errors are negligible. In the case, that these errors exist, the control scheme for the third case could be also applied to first and second case.

Two approaches have been considered for controlling the platform. In robotics' field the common approach is the kinematic [1], [2], [4]. The control problem can be also attacked from the dynamic point of view [5]. For a good discussion about dynamics and kinematic models of wheeled mobile robots please refer to [3]. The kinematic approach has the advantage of being easy to compute while having the disadvantage of tracking errors due to no compensation for the slip phenomena. The dynamic approach has the potential advantage of being more precise. However, it has some disadvantages since it requires accurate knowledge of the platform and wheel speeds, and also mass and platform inertia. The main difficulty at this point is the knowledge of platform inertia. The fluoroscope components, emitter and image intensifier, are mounted on 2 XZ tables placed in platform lateral sides, which are moved with 2 linear and 2 rotary servomotors as Figure 2.8 shows. These high-elevation mass elements affect the Z platform's inertia moment significantly. The linear (mounted horizontally) and rotary (mounted vertically) servomotors move the XZ table with 2g

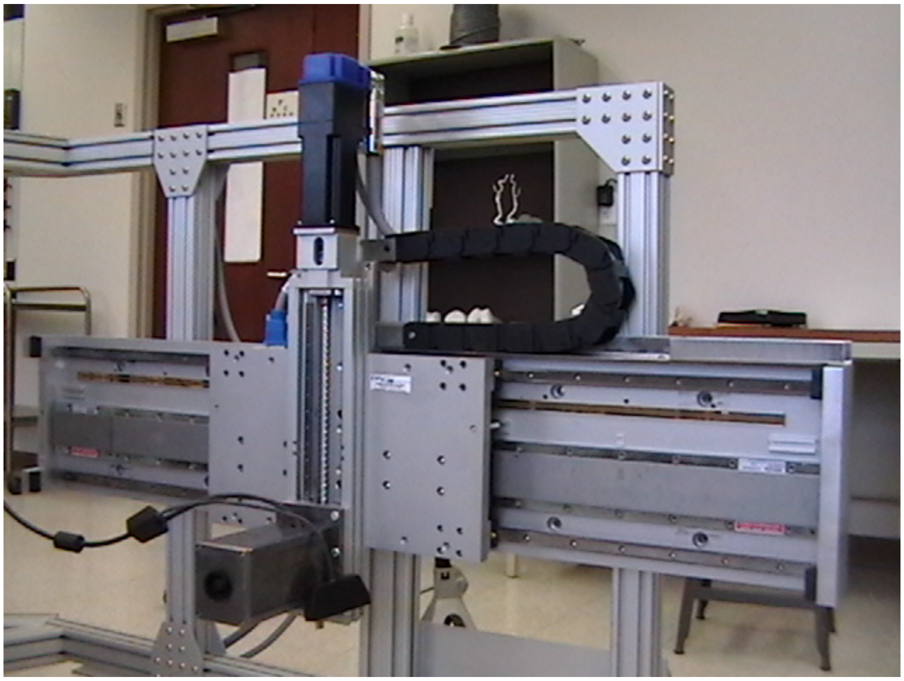

Figure 2.8 XZ table

accelerations making the real-time computing of inertia moment hard to achieve. The next sections present the kinematic and the dynamic models for the platform.

2.2 TRACKING KINEMATIC

Three tracking cases have been previously established. In this case slipping is assumed negligible, which means that wheels' speed is equivalent to platform's speed. Since, in the first and second cases the subject walks over a straight line, and no slipping is expected, then steering would not be required in those cases. Hence, kinematic only involves driving motors' speed calculation. Figures 2.9 and 2.10s show Case 1 and Case 2 representations.

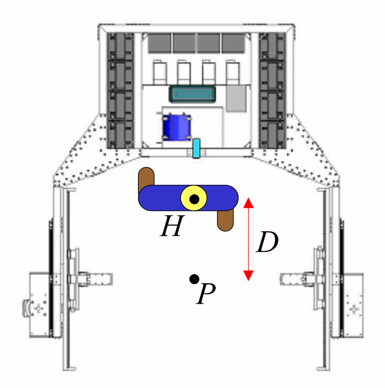

Figure 2.9 Case 1

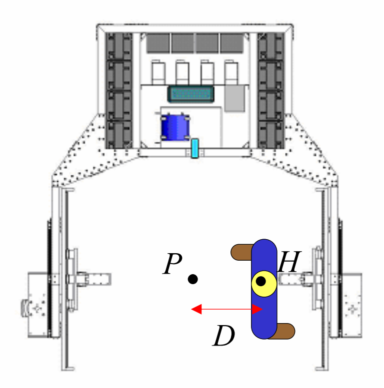

Figure 2.10 Case 2

The subject-platform stand-off distance, D, is the error to overcome by control algorithms. Differentiating D respect to the time, the relative velocity between the platform and the subject is obtained.

$$v_R = \frac{dD}{dt} \qquad \text{Eq. 2.1}$$

Adding or subtracting this relative velocity to the previously absolute velocity, the new driving servomotor absolute velocity is calculated. It is worth mentioning that for these two cases, the speed set point is the same for both driving wheel servomotors.

Let’s now consider the general case, case 3, in which subject walking direction changes or the platform slips, likely generating a subject-platform orientation error, α. The subject-platform angle, α, and the subject-platform stand-off distance, D, are measurable, and both must minimized. Figure 2.11 shows this case.

In this case, it is assumed that the subject and platform orientations are the same as their movement directions respectively. Thus, parallel movements as shown in Figure 2.12 are discarded.

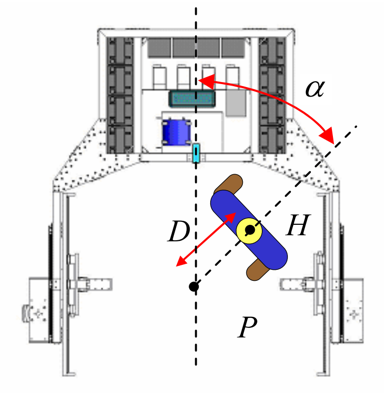

Figure 2.11 Case 3

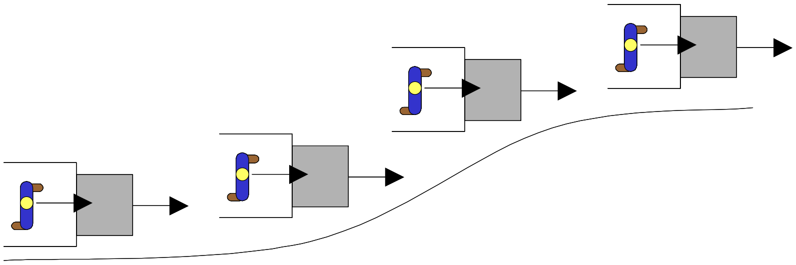

Figure 2.12 Parallel movement

From system inputs D and α, the servocontrol input set points must be determined. The system has two driving-steering wheels previously named wheel 1 and wheel 3. Each of those wheels has two servomotors, a steering and a driving servomotor. Then, their names are defined as follow:

DS1= Driving servomotor of wheel 1
SS1= Steering servomotor of wheel 1
DS3= Driving servomotor of wheel 3
SS3= Steering servomotor of wheel 3

The servomotors' input variables are the speed and direction angle of driving and steering servomotors respectively. Therefore, α1, v1, α3, and v3 have to be calculated from D and α. To do that, the classical rigid body approach will be used. First consider when the subject and platform are moving in the same direction with α being 0 and subject placed in the desired position. Then, consider the subject changes his/her direction to an angle α respect to the platform orientation, and also moves producing a distance error, D, as shown in Figure 2.13. The subject movement can be seen as a rotation of angle α and a relative translation of distance D. In the same way, the platform must rotate an angle α along vertical axis at point P and then translate a distance D resulting in null orientation and stand-off distance error. Using rigid body kinematic, equation 2.3, wheel 1 and wheel 3 parameters are calculated based on the previous movement description.

The yaw rate can be either measured or calculated differentiating the rotation angle with respect to the time. In the same way, the relative velocity between the platform and the subject can be either measured or calculated differentiating D respect to time.

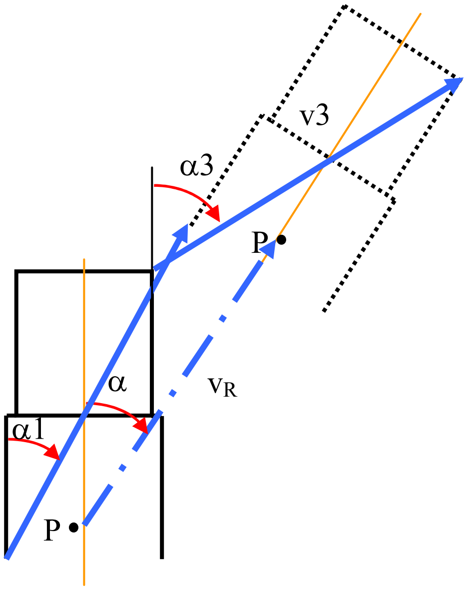

Figure 2.13 Actual and next platform positions

$$\dot{\alpha} = \frac{d\alpha}{dt}$$

$$\vec{v}_R = \frac{d\vec{D}}{dt} \qquad \text{Eq. 2.2}$$

The relative velocity of each wheel is calculated using next equations.

$$\vec{v}_1 = \vec{v}_R + \vec{r}_{P1} \times \dot{\alpha}\vec{k} \text{ and } \vec{v}_3 = \vec{v}_R + \vec{r}_{P3} \times \dot{\alpha}\vec{k} \qquad \text{Eq. 2.3}$$

Figure 2.13 shows the orientation of those vectors. Vectors r_{P1} and r_{P3} are the vectors from the center of rotation, P, to wheel 1 and to wheel 3 respectively.

Figure 2.14 shows the vectors r_{P1} and r_{P3}. X_{rel} is the direction of the platform in a translation condition that is going to be the most common one. The angles that form vectors r_{P1} and r_{P3} with the platform direction X_{rel} are θ1 and θ3 respectively.

Since v1 and v3 are vector variables calculated by equation 2.3, angles and norms α1, v1, α3, and v3 can be calculated as follow.

$$v_3 = norm(\vec{v}_3) \qquad \alpha_3 = ATAN\left(\frac{v_{3Y}}{v_{3X}}\right) \qquad \text{Eq. 2.4}$$

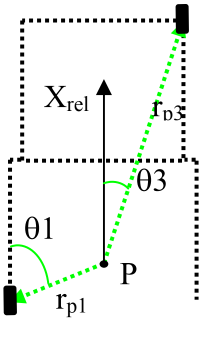

Figure 2.14 Vectors r_{P1} and r_{P3}

$$v_1 = norm(\vec{v}_1) \qquad \alpha_1 = ATAN\left(\frac{v_{1Y}}{v_{1X}}\right) \qquad \text{Eq. 2.5}$$

where v_{3X}, v_{3Y}, v_{1X} and v_{1Y} are the components of v_3 and v_1 in the direction of the platform and the direction perpendicular to the platform.

Applying the sine theorem to triangles showed in Figure 2.15, which are conformed by the translation, rotational and total speed of each wheel, the next equations are obtained.

$$\frac{r_{P1} * \dot{\alpha}}{\sin(\alpha - \alpha 1)} = \frac{v1}{\sin(90 - \alpha + \theta 1)} = \frac{v}{\sin(90 + \alpha 1 - \theta 1)} \qquad \text{Eq. 2.6}$$

$$\frac{r_{P3} * \dot{\alpha}}{\sin(\alpha 3 - \alpha)} = \frac{v3}{\sin(90 + \alpha - \theta 3)} = \frac{v}{\sin(90 - \alpha 3 + \theta 3)} \qquad \text{Eq. 2.7}$$

Finally, Figure 2.16 shows a detailed and comprehensive diagram of platform kinematic and the accomplishment with Ackerman's steering principle. Although, this principle is commonly used when moving a vehicle over a known curve since the ICR position is always known, for the subject tracking case the rigid body method is a better option. Ackerman's steering principle is presented here to show its concordance with the rigid body method that is going to be used. For the correct movement of the platform, it must instantly rotate over the instant center of rotation, ICR. Then, each platform point has an instant velocity perpendicular to ICR-platform vector, and has a velocity norm equal to the platform rotational speed, ω, multiplied by the ICR-platform distance. Therefore, Ackerman's steering principle states that the driving speed is equal to the platform rotational speed, ω, multiplied by the ICR-wheel distance. The steering angle is determined by the Xrel axis and the line perpendicular to ICR-wheel vector.

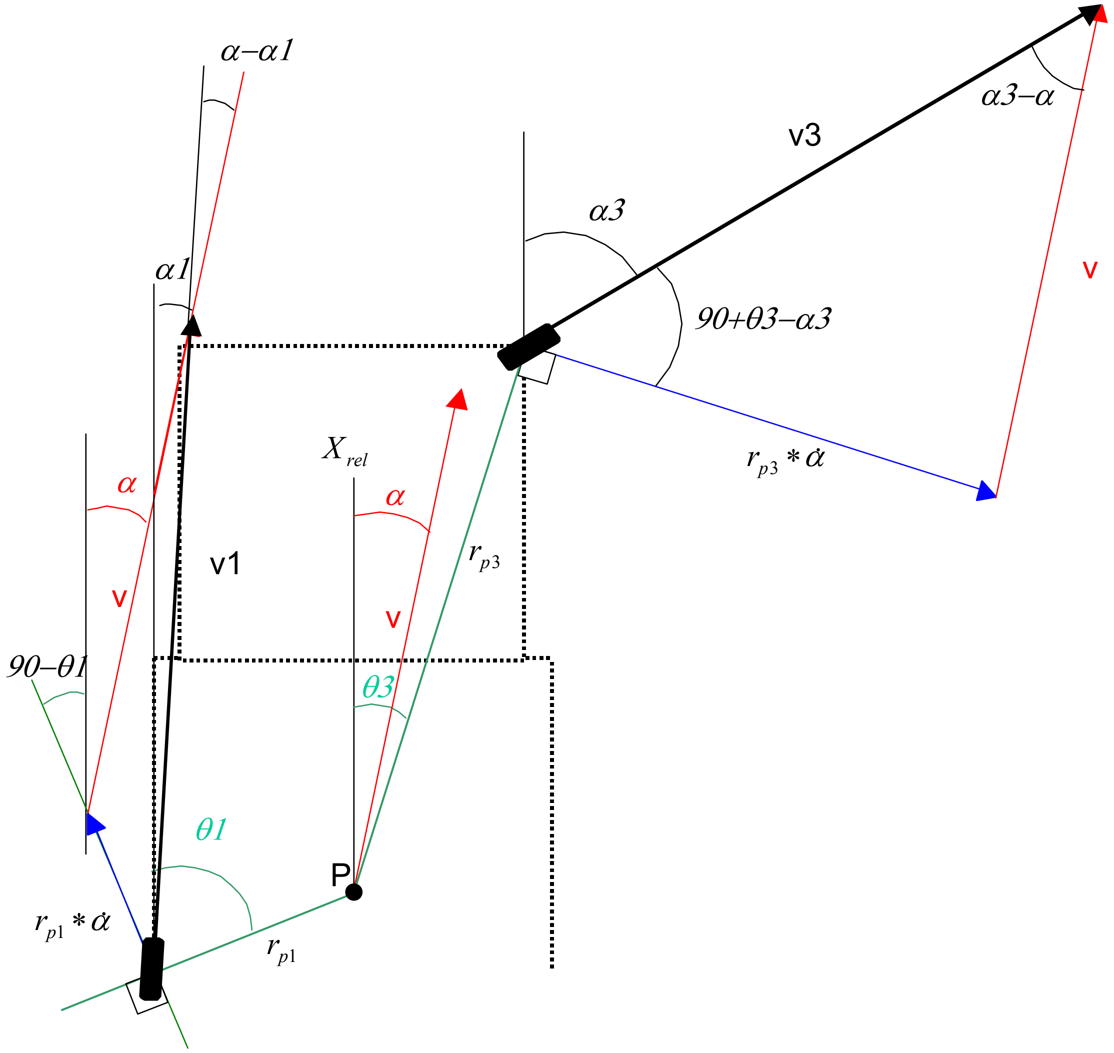

Figure 2.15 Wheel 1 and 3 speeds calculation

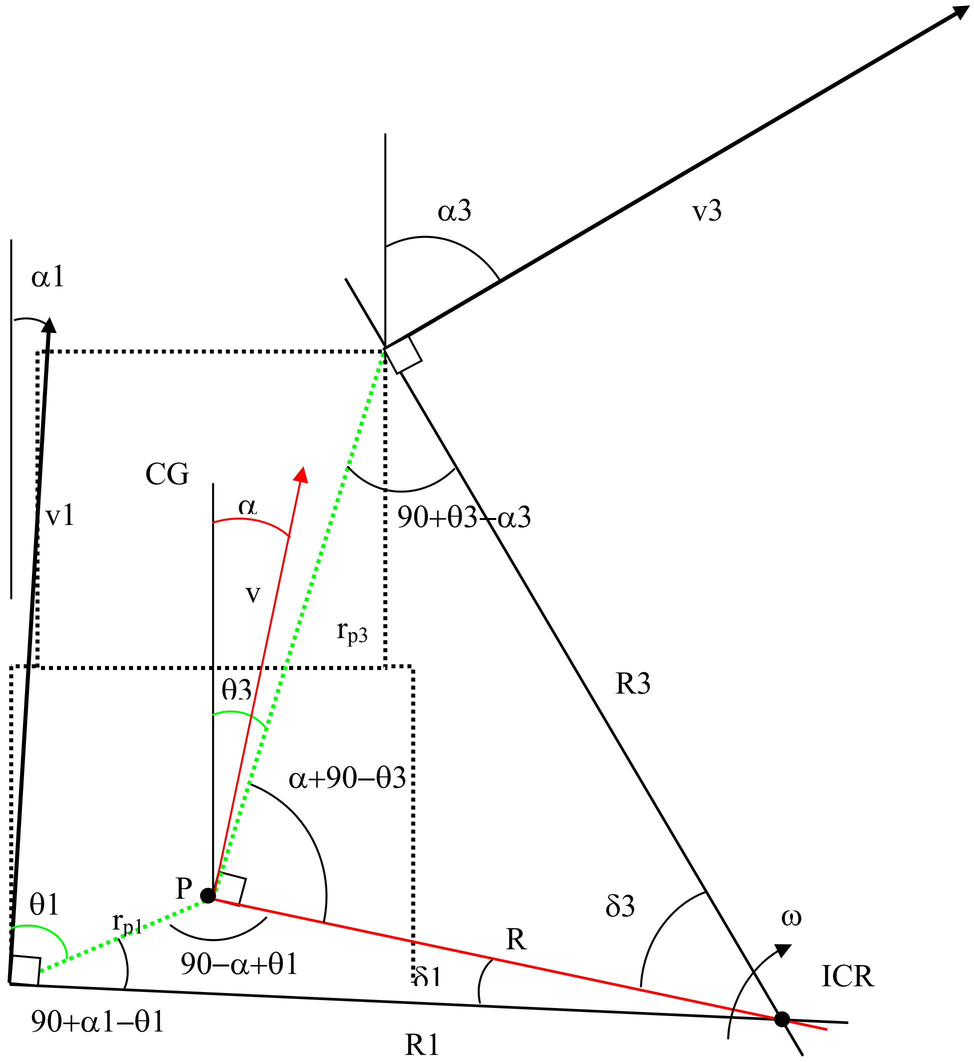

Figure 2.16 Instant Center of Rotation

Analyzing triangles R-r_{p3}-R3 and R1-r_{p1}-R in Figure 2.16:

$\delta1=180-(90+\alpha1-\theta1)-(90-\alpha+\theta1)=\alpha-\alpha1$ Eq. 2.8

$\delta3=180-(90-\alpha3+\theta3)-(90+\alpha-\theta3)=\alpha3-\alpha$ Eq. 2.9

The following equations are obtained using sine theorem applied to triangles R-r_{p3}-R3 and R1-r_{p1}-R.

$$\frac{r_{p1}}{\sin(\delta 1)}=\frac{R1}{\sin(90-\alpha+\theta 1)}=\frac{R}{\sin(90+\alpha 1-\theta 1)} \qquad \text{Eq. 2.10}$$

$$\frac{r_{p3}}{\sin(\delta 3)}=\frac{R3}{\sin(90+\alpha-\theta 3)}=\frac{R}{\sin(90-\alpha 3+\theta 3)} \qquad \text{Eq. 2.11}$$

Multiplying by the rotational speed ω; also considering v1=ω*R1 and v3=ω*R3.

$$\frac{r_{p1}*\omega}{\sin(\alpha-\alpha 1)}=\frac{v1}{\sin(90-\alpha+\theta 1)}=\frac{v}{\sin(90+\alpha 1-\theta 1)} \qquad \text{Eq. 2.12}$$

$$\frac{r_{p3}*\omega}{\sin(\alpha 3-\alpha)}=\frac{v3}{\sin(90+\alpha-\theta 3)}=\frac{v}{\sin(90-\alpha 3+\theta 3)} \qquad \text{Eq. 2.13}$$

Equations 2.12 and 2.13 are equal to equations 2.6 and 2.7 obtained calculating wheels' speed with rigid body method. The instant center of rotation method is generally used when its position is previously known, for example in path planning when trying to follow straight and curve lines. However, for a tracking system the ICR position is unknown, then the rigid body method is ideal for speed calculation in the tracking fluoroscope system.

2.3 TRACKING DYNAMICS

The advantages and disadvantages of using a dynamic model for the platform control were previously addressed. This section presents the dynamic model of the platform for the three cases established. The free motion mode is sketched first, and then a simplified model for the forward and translational modes is studied.

2.3.1 Free Motion Mode

Figure 2.17 shows a free-body diagram for the platform, where each term is defined in Table 2.1. Rolling friction was disregard since platform moves at low speeds making that term insignificant respect to traction/friction forces.

Next chapter gives the model to calculate the lateral and forward forces on each wheel. The next step at this point is to transform these forces into the relative platform frame, defined by Figure 2.4 and showed in Figure 2.17.

Figure 2.18 serves not only for force calculation at wheel 3, but also is also a typical of force calculation for the other wheels. As Figure 2.18 shows, the wheel frame is rotated and angle α3 respect to the platform frame. Then the lateral and forward forces can be represented at the platform relative frame as:

$$\begin{aligned} F'_{3X} &= F''_{3F} * \cos(\alpha 3) - F''_{3L} * \sin(\alpha 3) \\ F'_{3Y} &= F''_{3F} * \sin(\alpha 3) + F''_{3L} * \cos(\alpha 3) \end{aligned} \qquad \text{Eq. 2.14}$$

Writing equation 2.14 in a matrix notation, then:

$$\begin{pmatrix} F'_{3X} \\ F'_{3Y} \end{pmatrix} = \begin{bmatrix} \cos(\alpha 3) & -\sin(\alpha 3) \\ \sin(\alpha 3) & \cos(\alpha 3) \end{bmatrix} \begin{pmatrix} F''_{3F} \\ F''_{3L} \end{pmatrix} \qquad \text{Eq. 2.15}$$

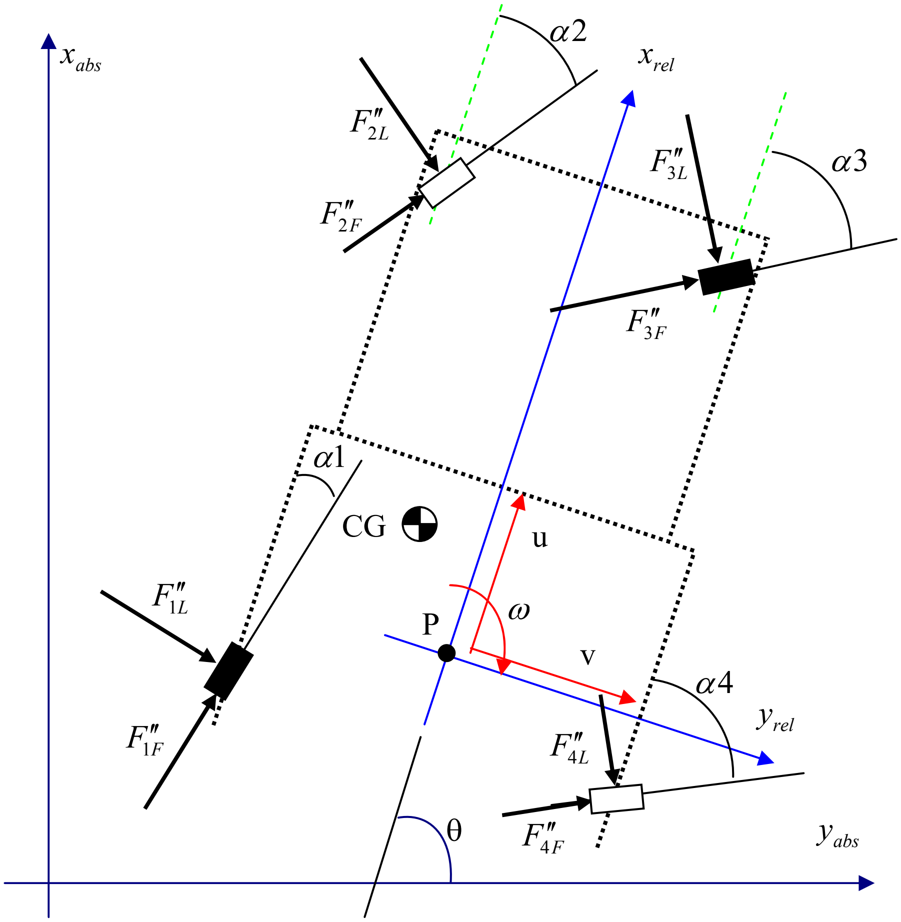

Figure 2.17 Platform Dynamic Model

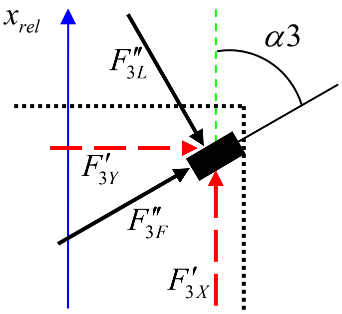

Figure 2.18 Forces at platform frame

Table 2.1 Dynamic model parameters

CG	Platform Center of gravity
F''_{1L} , F''_{2L} , F''_{3L} , F''_{4L}	Lateral Friction Forces on each wheel
F''_{1F} , F''_{2F} , F''_{3F} , F''_{4F}	Forward Friction/Traction Forces on each wheel
F'_{1L} , F'_{2L} , F'_{3L} , F'_{4L}	Friction Forces on each wheel in the direction of y_{rel}
F'_{1F} , F'_{2F} , F'_{3F} , F'_{4F}	Friction Forces on each wheel in the direction of x_{rel}
F_X, F_Y	Resultant friction forces expressed in the absolute frame
$\alpha 1$, $\alpha 2$, $\alpha 3$, $\alpha 4$	Steering angle at each wheel
u	Forward velocity
v	Lateral velocity
$\ddot{\theta}$	Rotational acceleration
$\omega = \dot{\theta}$	Rotational velocity or yaw rate
θ	Rotational angle ($\int \omega dt$)
x_{abs}, y_{abs}	Absolute frame axes, fixed respect to room
x_{rel}, y_{rel}	Relative frame axes, fixed respect to platform

By the same procedure the forces at the other wheels can be rewritten as:

$$\left.\begin{array}{l}
\begin{pmatrix} F'_{1X} \\ F'_{1Y} \end{pmatrix} = \begin{bmatrix} \cos(\alpha 1) & -\sin(\alpha 1) \\ \sin(\alpha 1) & \cos(\alpha 1) \end{bmatrix} \begin{pmatrix} F''_{1F} \\ F''_{1L} \end{pmatrix} \\
\begin{pmatrix} F'_{2X} \\ F'_{2Y} \end{pmatrix} = \begin{bmatrix} \cos(\alpha 2) & \sin(\alpha 2) \\ \sin(\alpha 2) & -\cos(\alpha 2) \end{bmatrix} \begin{pmatrix} F''_{2F} \\ F''_{2L} \end{pmatrix} \\
\begin{pmatrix} F'_{4X} \\ F'_{4Y} \end{pmatrix} = \begin{bmatrix} \cos(\alpha 4) & \sin(\alpha 4) \\ \sin(\alpha 4) & -\cos(\alpha 4) \end{bmatrix} \begin{pmatrix} F''_{4F} \\ F''_{4L} \end{pmatrix}
\end{array}\right\} \qquad \text{Eq. 2.16}$$

Figure 2.19 shows the new force diagram, and Figure 2.20 illustrates platform geometric parameters.

The system considers point P as a reference point to track the subject. The on-board sensor will measure the distance between itself and the actual subject position. Since the distance from the on-board sensor to P is known, then the stand-off distance error, D, can be easily computed. The algorithms will calculate the platform acceleration necessary to decrease the subject-platform distance error. Thus, the dynamic equations take P as a reference point to calculate platform speeds, instead of taking the center of gravity as the reference point as the traditional procedure does. Recall that the yaw rate of a rigid is unique and does not depend on the point of calculation (1). Therefore, platform yaw rate is computed at the center of gravity for simplicity.

Applying the conservation of angular momentum law at point CG:

$$\boxed{\begin{array}{l} I_{GC} * \ddot{\theta} = F'_{1X} * (Lr - L_{GC}) - F'_{4X} * (Lr + L_{GC}) + F'_{2X} * (Lf - L_{GC}) - F'_{3X} * (Lf + L_{GC}) + \\ -(F'_{1Y} + F'_{4Y}) * (Fr + F_{GC}) + (F'_{2Y} + F'_{3Y}) * (Ff - F_{GC}) \end{array}}$$

where $\ddot{\theta} = \dot{\omega}$ Eq. 2.17

From here and in advance, if acceleration, speed and position do not show a sub index, then they refer to point P. To calculate platform acceleration, the forces and speed have to be transformed to the absolute coordinate frame.

---

[1] See appendix A for derivation

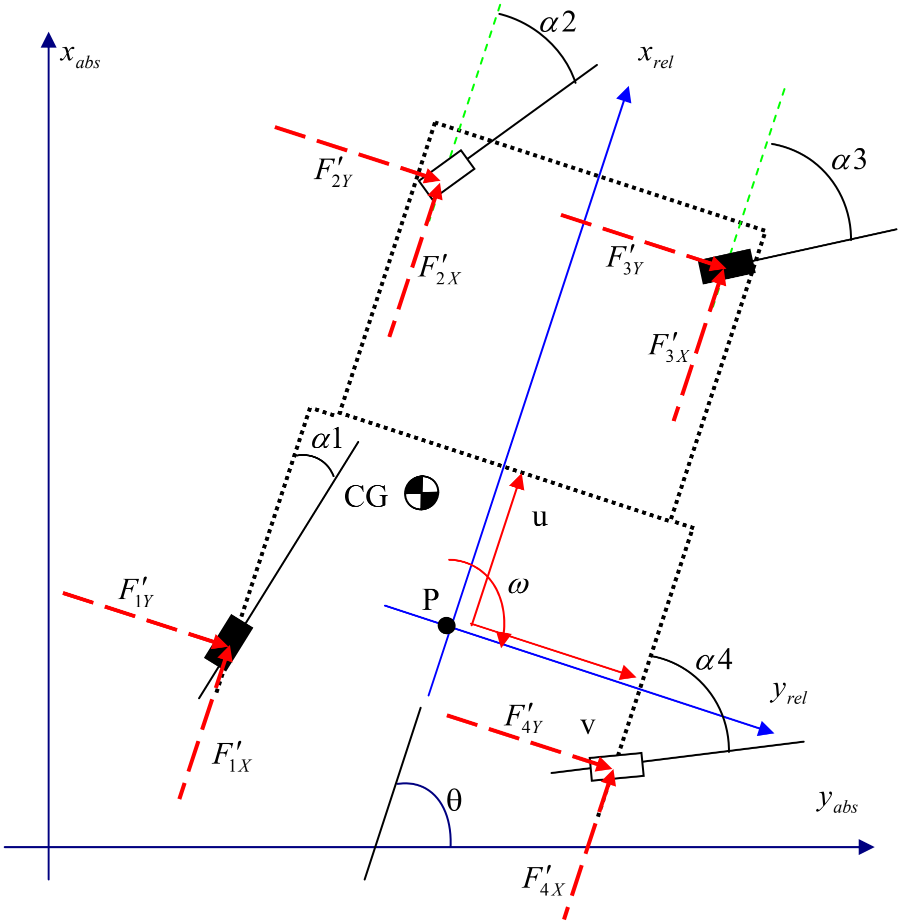

Figure 2.19 Forces diagram written in the platform frame

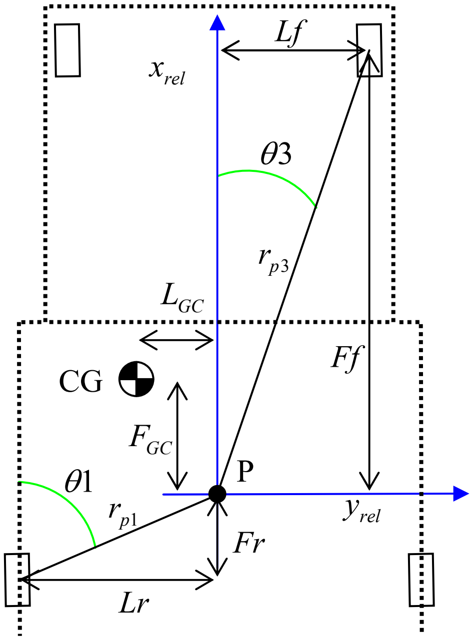

Figure 2.20 Platform geometric

The relative frame with origin at P moves with a velocity u in the x_{rel} direction, a velocity v in the y_{rel} direction and with a rotational speed ω, then the relative frame moves with the next speed respect to the absolute frame:

$$\begin{pmatrix} \dot{X} \\ \dot{Y} \end{pmatrix} = \begin{bmatrix} \sin(\theta) & -\cos(\theta) \\ \cos(\theta) & \sin(\theta) \end{bmatrix} \begin{pmatrix} u \\ v \end{pmatrix} \qquad \text{Eq. 2.18}$$

Differentiating respect to the time, acceleration respect to the absolute frame can be computed.

$$\begin{pmatrix} \ddot{X} \\ \ddot{Y} \end{pmatrix} = \omega * \begin{bmatrix} \cos(\theta) & \sin(\theta) \\ -\sin(\theta) & \cos(\theta) \end{bmatrix} \begin{pmatrix} u \\ v \end{pmatrix} + \begin{bmatrix} \sin(\theta) & -\cos(\theta) \\ \cos(\theta) & \sin(\theta) \end{bmatrix} \begin{pmatrix} \dot{u} \\ \dot{v} \end{pmatrix} \qquad \text{Eq. 2.19}$$

The forces translated to the absolute frame are:

$$\begin{pmatrix} F_X \\ F_Y \end{pmatrix} = \begin{bmatrix} \sin(\theta) & -\cos(\theta) \\ \cos(\theta) & \sin(\theta) \end{bmatrix} \begin{pmatrix} \sum_{i=1}^{4} F'_{iX} \\ \sum_{i=1}^{4} F'_{iY} \end{pmatrix} \qquad \text{Eq. 2.20}$$

Applying the second Newtown law of conservation of movement to the platform:

$$\begin{bmatrix} m & 0 \\ 0 & m \end{bmatrix}\begin{pmatrix} \ddot{X}_{GC} \\ \ddot{Y}_{GC} \end{pmatrix} = \begin{pmatrix} F_X \\ F_Y \end{pmatrix} \qquad \text{Eq. 2.21}$$

Observe that the second Newton law was applied to the platform center of gravity. To transform these results to the reference point P, the acceleration relationship between the Center of Gravity and point P must be introduced

$$\vec{a}_{GC} = \vec{a}_P - \dot{\vec{\omega}} \times (P - CG) - \vec{\omega} \times (\vec{\omega} \times (P - CG)) \qquad \text{Eq. 2.22}$$

Considering from Figure 2.20 that $(P - CG) = -L_{GC}\vec{x}_{rel} - F_{GC}\vec{y}_{rel}$, then using at equation 2.22:

$$\begin{pmatrix} \ddot{X}_{GC} \\ \ddot{Y}_{GC} \end{pmatrix} = \begin{pmatrix} \ddot{X} \\ \ddot{Y} \end{pmatrix} + \dot{\omega}\vec{z}_{rel} \times (-L_{GC}\vec{x}_{rel} - F_{GC}\vec{y}_{rel}) - \omega\vec{z}_{rel} \times (\omega\vec{z}_{rel} \times (-L_{GC}\vec{x}_{rel} - F_{GC}\vec{y}_{rel}))$$

Where, $\vec{a}_{GC} = \begin{pmatrix} \ddot{X}_{GC} \\ \ddot{Y}_{GC} \end{pmatrix}$ $\vec{a}_P = \begin{pmatrix} \ddot{X} \\ \ddot{Y} \end{pmatrix}$, and Z$_{\text{rel}}$ is the vertical axis, then doing the cross product:

$$\begin{pmatrix} \ddot{X}_{GC} \\ \ddot{Y}_{GC} \end{pmatrix} = \begin{pmatrix} \ddot{X} \\ \ddot{Y} \end{pmatrix} + \begin{bmatrix} \sin(\theta) & -\cos(\theta) \\ \cos(\theta) & \sin(\theta) \end{bmatrix}\begin{pmatrix} -\ddot{\theta} * L_{GC} - \omega^2 * F_{GC} \\ +\ddot{\theta} * F_{GC} - \omega^2 * L_{GC} \end{pmatrix}$$

Combining at equations 2.21 and last equation it results

$$\begin{bmatrix} m & 0 \\ 0 & m \end{bmatrix}\left(\begin{pmatrix} \ddot{X} \\ \ddot{Y} \end{pmatrix} + \begin{bmatrix} \sin(\theta) & -\cos(\theta) \\ \cos(\theta) & \sin(\theta) \end{bmatrix}\begin{pmatrix} -\ddot{\theta} * L_{GC} - \omega^2 * F_{GC} \\ +\ddot{\theta} * F_{GC} - \omega^2 * L_{GC} \end{pmatrix}\right) = \begin{pmatrix} F_X \\ F_Y \end{pmatrix}$$

Introducing the acceleration formula of equation 2.19 in last equation, replacing the forces at the absolute frame by using equation 2.20, and calling sin(θ)=S, and cos(θ)=C:

$$m*\left(\omega*\begin{bmatrix}C & S\\ -S & C\end{bmatrix}\begin{pmatrix}u\\ v\end{pmatrix}+\begin{bmatrix}S & -C\\ C & S\end{bmatrix}\begin{pmatrix}\dot{u}\\ \dot{v}\end{pmatrix}\right)=\begin{bmatrix}S & -C\\ C & S\end{bmatrix}\left\{\begin{pmatrix}\sum_{i=1}^{4}F'_{iX}\\ \sum_{i=1}^{4}F'_{iY}\end{pmatrix}-m\begin{pmatrix}-\ddot{\theta}*L_{GC}-\omega^{2}*F_{GC}\\ +\ddot{\theta}*F_{GC}-\omega^{2}*L_{GC}\end{pmatrix}\right\}$$

Pre-multiplying both sides of last equation by $\begin{bmatrix}\sin(\theta) & \cos(\theta)\\ -\cos(\theta) & \sin(\theta)\end{bmatrix}$, next equation is found

$$m*\left(\omega*\begin{bmatrix}S & C\\ -C & S\end{bmatrix}\begin{bmatrix}C & S\\ -S & C\end{bmatrix}\begin{pmatrix}u\\ v\end{pmatrix}+\begin{bmatrix}S & C\\ -C & S\end{bmatrix}\begin{bmatrix}S & -C\\ C & S\end{bmatrix}\begin{pmatrix}\dot{u}\\ \dot{v}\end{pmatrix}\right)=$$

$$\begin{bmatrix}S & C\\ -C & S\end{bmatrix}\begin{bmatrix}S & -C\\ C & S\end{bmatrix}\begin{pmatrix}\sum_{i=1}^{4}F'_{iX}+\ddot{\theta}*L_{GC}*m+\omega^{2}*F_{GC}*m\\ \sum_{i=1}^{4}F'_{iY}-\ddot{\theta}*F_{GC}*m+\omega^{2}*L_{GC}*m\end{pmatrix}$$

Expanding:

$$m*\left(\omega*\begin{bmatrix}SC-SC & C^{2}+S^{2}\\ -C^{2}-S^{2} & SC-SC\end{bmatrix}\begin{pmatrix}u\\ v\end{pmatrix}+\begin{bmatrix}C^{2}+S^{2} & SC-SC\\ SC-SC & C^{2}+S^{2}\end{bmatrix}\begin{pmatrix}\dot{u}\\ \dot{v}\end{pmatrix}\right)=$$

$$\begin{bmatrix}C^{2}+S^{2} & SC-SC\\ SC-SC & C^{2}+S^{2}\end{bmatrix}\begin{pmatrix}\sum_{i=1}^{4}F'_{iX}+\ddot{\theta}*L_{GC}*m+\omega^{2}*F_{GC}*m\\ \sum_{i=1}^{4}F'_{iY}-\ddot{\theta}*F_{GC}*m+\omega^{2}*L_{GC}*m\end{pmatrix}$$

Using trigonometric identities

$$m*\left(\omega*\begin{bmatrix}0 & 1\\ -1 & 0\end{bmatrix}\begin{pmatrix}u\\ v\end{pmatrix}+\begin{bmatrix}1 & 0\\ 0 & 1\end{bmatrix}\begin{pmatrix}\dot{u}\\ \dot{v}\end{pmatrix}\right)=\begin{bmatrix}1 & 0\\ 0 & 1\end{bmatrix}\begin{pmatrix}\sum_{i=1}^{4}F'_{iX}+\ddot{\theta}*L_{GC}*m+\omega^{2}*F_{GC}*m\\ \sum_{i=1}^{4}F'_{iY}-\ddot{\theta}*F_{GC}*m+\omega^{2}*L_{GC}*m\end{pmatrix}$$

Reducing:

$$m * \begin{pmatrix} \dot{u} \\ \dot{v} \end{pmatrix} = \begin{pmatrix} \sum_{i=1}^{4} F'_{iX} + \ddot{\theta} * L_{GC} * m + \omega^2 * F_{GC} * m \\ \sum_{i=1}^{4} F'_{iY} - \ddot{\theta} * F_{GC} * m + \omega^2 * L_{GC} * m \end{pmatrix} - m * \omega * \begin{pmatrix} v \\ -u \end{pmatrix}$$

the general movement equation of motion is:

$$\boxed{\begin{pmatrix} \dot{u} \\ \dot{v} \end{pmatrix} = \begin{pmatrix} \dfrac{\sum_{i=1}^{4} F'_{iX}}{m} + \ddot{\theta} * L_{GC} + \omega^2 * F_{GC} - \omega * v \\ \dfrac{\sum_{i=1}^{4} F'_{iY}}{m} - \ddot{\theta} * F_{GC} + \omega^2 * L_{GC} + \omega * u \end{pmatrix}} \qquad \text{Eq. 2.23}$$

Equations 2.17 and 2.23 govern the platform rotational and translational dynamics. One disadvantage of the dynamic method is that the forces at each wheel must be known. That not only implies the knowledge of the tire and caster models, but also accurate knowledge of the caster and tire properties needed by those models. Since no information was available from the manufacturers, some experiments were carried out to quantify these parameters. Next section simplifies the previous model to apply it in the lateral and forward translational modes. Hence, one of the objectives of this thesis is to study the applicability of the simplified dynamic model in control design.

2.3.2 Forward and Lateral Motion Mode

The main control objective for these cases is to keep the subject-platform distance within certain values. That is keeping the tracking error distance lower than a certain value L while the platform and subject run over a straight line. The value of L can be set as an example at 0.1 meters. Although, there is not a defined value for L; minimizing it, would reduce the work done by the joint tracking control. Varying the speed of the wheels the forces applied will be modified to cancel the total moment respect to the center of gravity, and then make the yaw rate null. Thus, no steering would be necessary and no lateral force would appear in the wheels. In the case the angular moment is not null, lateral forces velocities appear, longitudinal velocity will be altered and an orientation error would occur. Since the system has no device to measure that orientation error, then there is no clue of how to steer the wheels. Hence, steering would not be applied. Finally, experiments will show the orientation errors generated when this method is applied, and then check how well were balanced the wheel forces to get a null moment. Another assumption to be checked by experiments, is considering the caster wheels as ideal ball bearings, and then frictionless. Even the caster wheel model is not extremely complicated, considering it for the system modeling would imply knowing the casters' speed and yaw rate, and ultimately installing potentiometers and encoders on them. Figure 2.21 shows the simplified dynamic model, considering perfect moment balance.

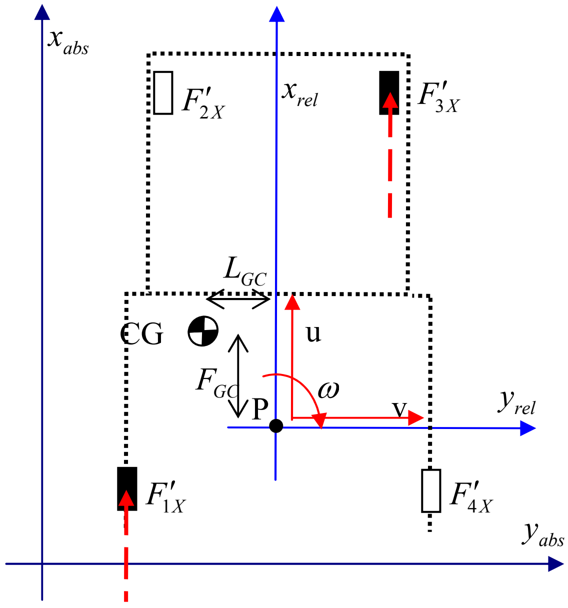

Figure 2.21 Translational dynamic model

Equation 2.19 is still applicable:

$$\begin{pmatrix}\dot{X}\\ \dot{Y}\end{pmatrix} = \omega * \begin{bmatrix}\cos(\theta) & \sin(\theta)\\ -\sin(\theta) & \cos(\theta)\end{bmatrix}\begin{pmatrix}u\\ v\end{pmatrix} + \begin{bmatrix}\sin(\theta) & -\cos(\theta)\\ \cos(\theta) & \sin(\theta)\end{bmatrix}\begin{pmatrix}\dot{u}\\ \dot{v}\end{pmatrix} \qquad \text{Eq. 2.19}$$

Applying the conservation of angular momentum law at point CG:

$$\boxed{\ddot{\theta} = \frac{F'_{1X} * (Lr - L_{GC}) - F'_{3X} * (Lf + L_{GC})}{I_{GC}}} \qquad \text{Eq. 2.24}$$

Applying conservation of movement law to point P of the platform: from Eq. 2.23.

$$\boxed{\begin{pmatrix}\dot{u}\\ \dot{v}\end{pmatrix} = \begin{pmatrix}\dfrac{F'_{1X} + F'_{3X}}{m} + \ddot{\theta} * L_{GC} + \omega^2 * F_{GC} - \omega * v\\ -\ddot{\theta} * F_{GC} + \omega^2 * L_{GC} + \omega * u\end{pmatrix}} \qquad \text{Eq. 2.25}$$

Equation 2.24 and 2.25 are under the assumption of frictionless caster wheels and no lateral force over driving motor wheels. The necessary condition to follow the subject in a straight line is to make the yaw rate ω=0. To achieve that, the yaw acceleration must be 0 at every moment. The traction (friction) forces at the wheels, F'_{1X} and F'_{3X}, depend on the platform and wheel speeds, as next chapter explains. Therefore, the main idea of the control system is to set dissimilar speeds to each wheel accomplishing a null yaw acceleration, and a platform speed such to keep platform-subject distance error at minimum.

From equation 2.24 to get null acceleration the condition is:

$$F'_{1X} * (Lr - L_{GC}) = F'_{3X} * (Lf + L_{GC}) \qquad \text{Eq. 2.26}$$

If yaw acceleration is always 0, then the yaw rate, ω, is 0 too, and θ=90. This fact and equation 2.19 leads to:

$$\begin{pmatrix}\dot{X}\\ \dot{Y}\end{pmatrix} = 0 * \begin{bmatrix}0 & 1\\ -1 & 0\end{bmatrix}\begin{pmatrix}u\\ v\end{pmatrix} + \begin{bmatrix}1 & 0\\ 0 & 1\end{bmatrix}\begin{pmatrix}\dot{u}\\ \dot{v}\end{pmatrix} = \begin{pmatrix}\dot{u}\\ \dot{v}\end{pmatrix} \qquad \text{Eq. 2.27}$$

Also operating at equation 2.25, it leads to:

$$m\begin{pmatrix} \dot{u} \\ \dot{v} \end{pmatrix} = m\begin{pmatrix} \ddot{X} \\ \ddot{Y} \end{pmatrix} = \begin{pmatrix} F'_{1X} + F'_{3X} \\ 0 \end{pmatrix} \qquad \text{Eq. 2.28}$$

These equations finish this section. Chapter three extends this approach adding the tire model.

2.4 PLATFORM SET-UP

The tracking fluoroscope system is being designed for laboratory floor surfaces. Recall that two translational modes will be provided. Translational forward mode, case 1, is a back/forward platform movement, while in translational lateral mode, case 2, the platform moves to its left and right directions. The system is going to be operated in restricted areas with specific motion corridors. A setup routine has been developed to rotate the platform in place for different modes of operations, Figure 2.22.

To make the platform rotate in place the instantaneous center of rotation must be a point on a line that connects the powered wheels, and it must be placed somewhere between those wheels. Without loosing generality the instantaneous center of rotation is placed at the midpoint between wheel 1 and wheel 3. In any platform rotation, every platform point will rotate around the ICR. To execute the setup movement, wheels must be steered 90-β degrees respect to the home position, relative X-axis, as Figure 2.23 shows. Angle β is defined by the wheel1-wheel3 line and the relative X-axis.

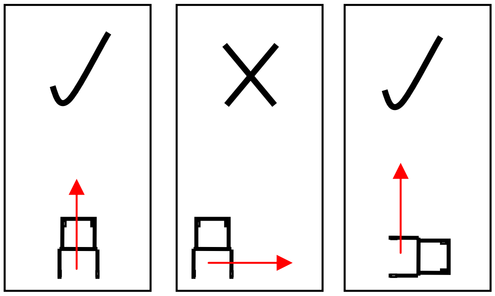

Case 1 Case 2 Case 2

Figure 2.22 Platform set up

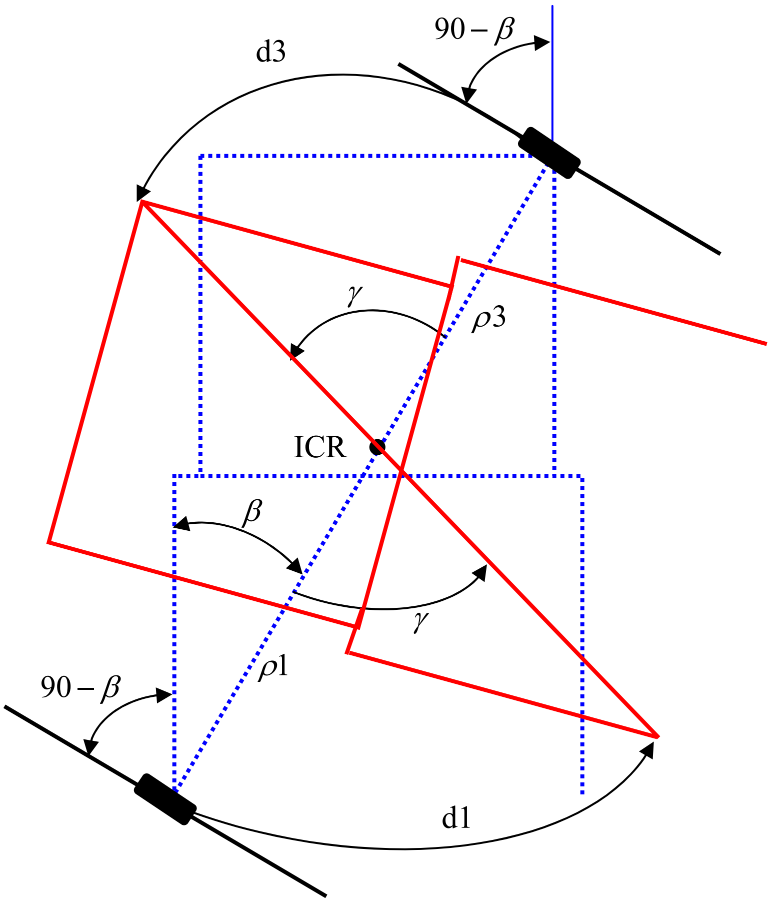

Figure 2.23 In place platform rotation.

Assuming no slipping and referring to Figure 2.23, for any rotation angle, γ, each point P will travel a distance d_p:

$d_p = \rho_p * \gamma$ ρ_p is the distance from the ICR to P Eq. 2.29

Hence, wheel 1 and wheel 3 travel:

$d_1 = \rho_1 * \gamma$, $d_3 = \rho_3 * \gamma$ Eq. 2.30

Defining the wheels radius as RW, the distance traveled for a driving wheel rotation, φ_1 and φ_3, is:

$d_1 = RW * \varphi_1$ $d_3 = RW * \varphi_3$ Eq. 2.31

Then, for an anticlockwise platform rotation of angle γ, from equations 2.30 and 2.31, the driving wheel rotation can be found:

$d_1 = \rho_1 * \gamma = -RW * \varphi_1$ $d_3 = \rho_3 * \gamma = RW * \varphi_3$

$\varphi_1 = -\dfrac{\rho_1 * \gamma}{RW}$ $\varphi_3 = \dfrac{\rho_3 * \gamma}{RW}$ Eq. 2.32

Finally, φ1 and φ3 are used as servo set point changes for the wheel 1 and wheel 3 drive servos to execute the setup maneuver. Table 2.2 shows the values of some platform parameters and the value of φ1 and φ3 for γ=90 degrees.

Table 2.2 Platform setup

	RAD	DEG
90-β	0.83	47.5
γ	1.57	90
	INCHES	METERS
ρ_1=ρ_3	45.52	1.16
d_1=d_3	71.5	1.816
	RAD	DEG
φ_1= φ_3	48.4	2775

Chapter 3. Servomotor and Tire models

The objective of this chapter is to present the servomotors and tire models needed for the kinematic and dynamic control models. The first section presents the load and servomotor models, the second section presents the servomotor closed loop control, and the last section presents a tire model.

3.1 LOAD AND SERVOMOTOR MODELING

The TFS has two powered omni-directional wheel drive units with two DC servomotors on each wheel, one for driving and the other for steering, for a total of four servomotors. Figure 3.1 contains 3 different perspective pictures of the unit.

The motor shaft is connected to a load with inertia J, which includes the motor rotor inertia and the reflected load inertia. A traction/friction force is applied to the load causing an external friction torque applied to the motor shaft. Drag force is also considered in the model. Table 3.1 reviews the nomenclature for the servomotor load model.

Table 3.1 Load model

T is the motor shaft torque	D is the drag coefficient
T_{ext} is the external friction torque	r is the gear box ratio
J is the total inertia (motor+load)	RW is the wheel radius
ω is the angular shaft speed	

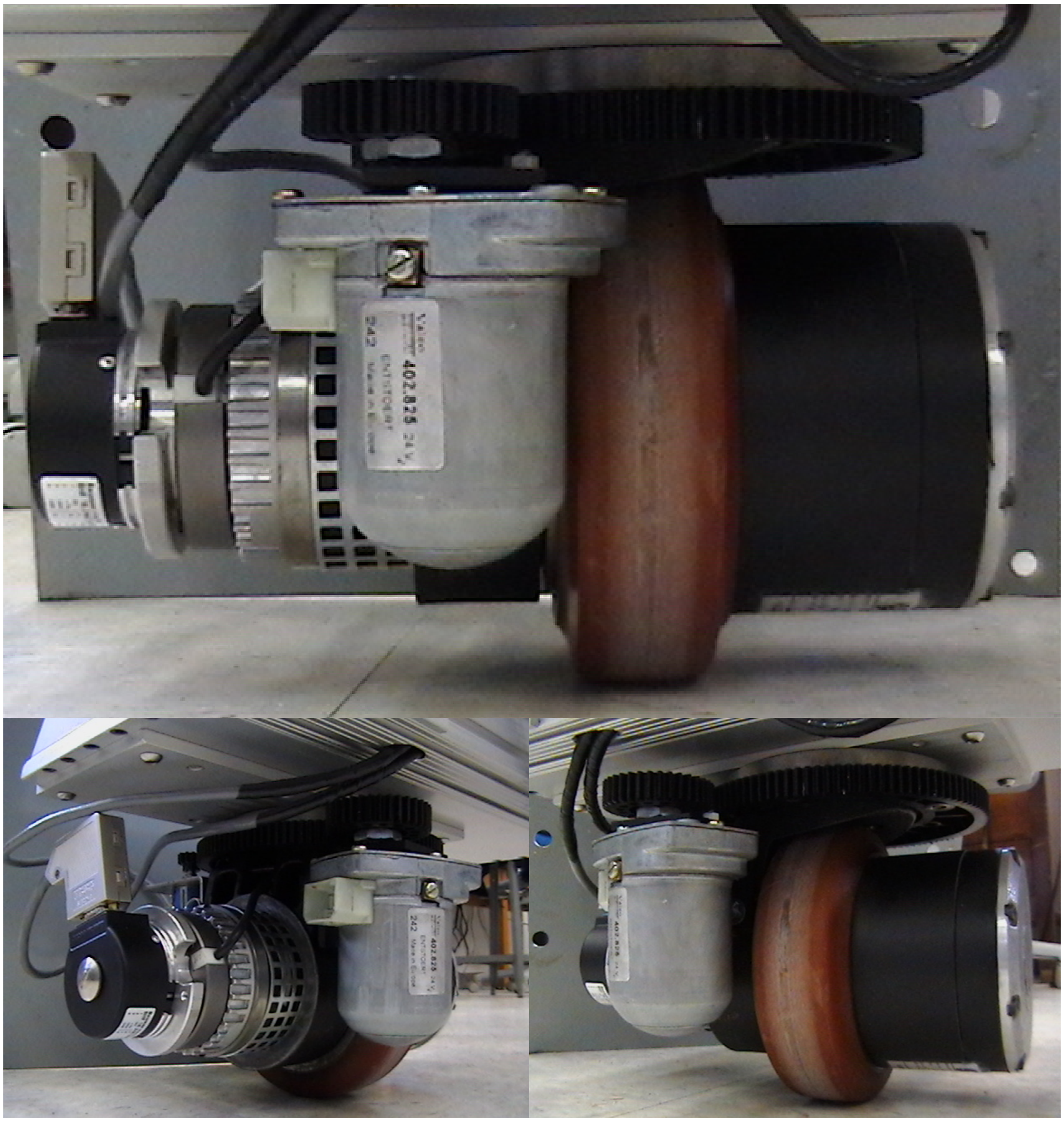

Figure 3.1 Driving and steering unit

3.1.1 Motor load dynamic model

Figure 3.2 shows the Load model and Figure 3.3 illustrates the Simulink model of the load.

Applying the conservation of angular momentum law to the load and motor shaft:

$$J * \frac{d\omega}{dt} = T - T_{ext} - D * \omega \qquad \text{Eq. 3.1}$$

where $T_{ext} = F_{ext} * \frac{RW}{r}$, being F_{ext} the traction force.

A DC servomotor is a motor with a DC input voltage. Its stator and a rotor can be represented as a resistance and inductance in series. The DC servomotor can be either field-controlled or armature-controlled, depending on which variables are controlled. Since armature-controlled model is normally used to approximate PM-DC brushless motors, only this kind is considered, and it is based in [6]. Field-controlled servomotor model is presented in Appendix B.

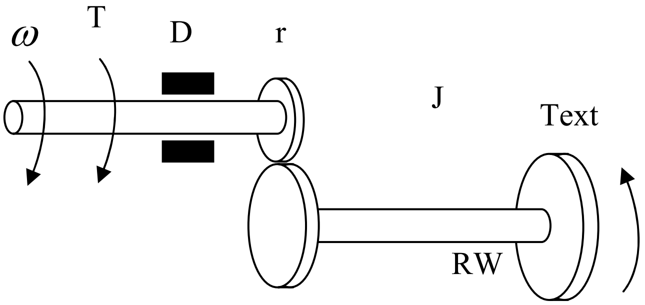

Figure 3.2 Load model

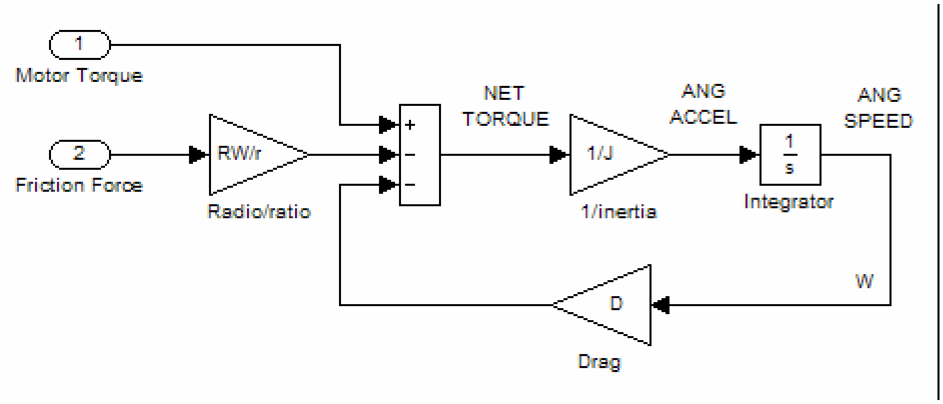

Figure 3.3 Simulink load model

3.1.2 Electric circuit model for armature-controlled dc servomotor

Table 3.2 reviews the nomenclature for the servomotor electric model.

Applying the first Kirchoff law to the electric circuit:

$$V_a = L_a * \frac{di_a}{dt} + R_a * i_a + V_{emf} \qquad \text{Eq. 3.2}$$

In this case the servomotor torque is proportional to the armature current.

$\boxed{T = K_t * i_a}$ K_t is the servomotor torque constant Eq. 3.3

The back electromotive force voltage is proportional to the servomotor shaft speed, then:

$\boxed{V_{emf} = K_e * \omega}$ K_e is the servomotor electromotive constant Eq. 3.4

Substituting i_a in Eq. 3.2 by Eq. 3.3 and V_{emf} by Eq. 3.4;

$$V_a = \frac{L_a}{K_t} * \frac{dT}{dt} + R_a * \frac{T}{K_t} + K_e * \omega$$

Figure 3.4 displays the electrical model for an armature-controlled motor model. Figure 3.5 shows the Simulink model correspondent to that model. Finally Figure 3.6 includes the load model and the servomotor model in a single Simulink diagram.

Table 3.2 Armature-controlled motor model

R_a is the motor armature resistance	i_a is the motor armature current
L_a is the motor armature inductance	V_a is the input motor armature voltage
V_{emf} is the back electromotive force	

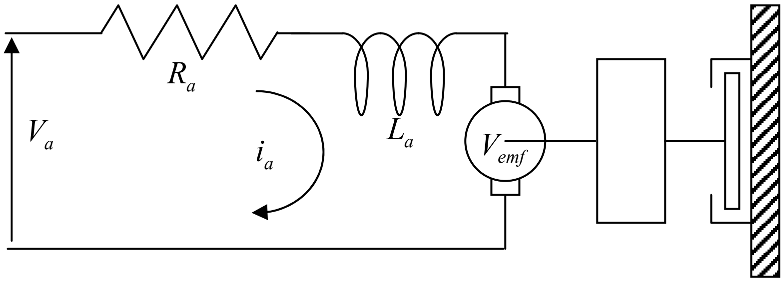

Figure 3.4 Armature-controlled motor model

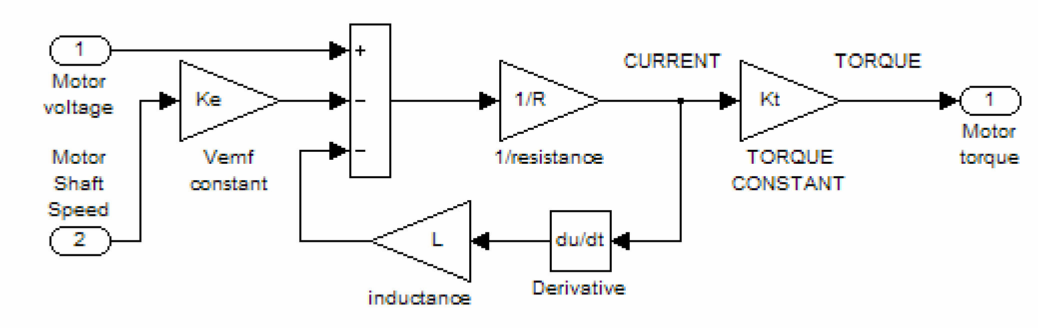

Figure 3.5 Simulink armature-controlled motor model

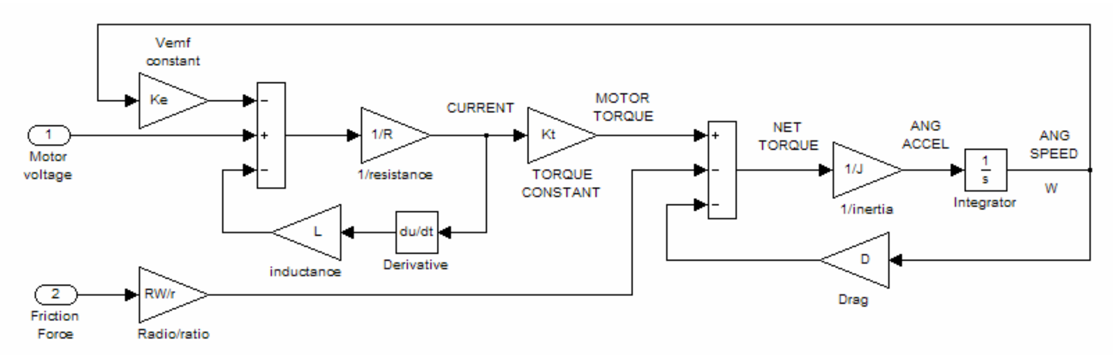

Figure 3.6 Simulink armature-controlled motor + load model

3.2 SERVOMOTOR CLOSED LOOP CONTROL

In the previous section, the DC servomotor model was presented, and it was shown that the servomotor’s input voltage relates to its shaft speed and position. Therefore, by varying the servomotor’s input voltage, speed and position can be controlled. However, this open loop control architecture cannot precisely control the variables. Thus, closed loop control architecture is imperative for accurate control of the process variables. To go from an open loop to a closed loop, some devices have to be incorporated to the loop, including feedback sensors to measure position and speed, and a controller. Controllers usually don’t have enough power to drive the servomotor so its output signal is sent to an amplifier after restraining to high and low limits. This process drives the servomotor. The servomotor closed loop control showing feedback, controller and amplifier is given in the next two Figures. Figure 3.7 shows a servomotor speed closed loop control, and Figure 3.8 shows a servomotor closed loop control with both speed and position controllers.

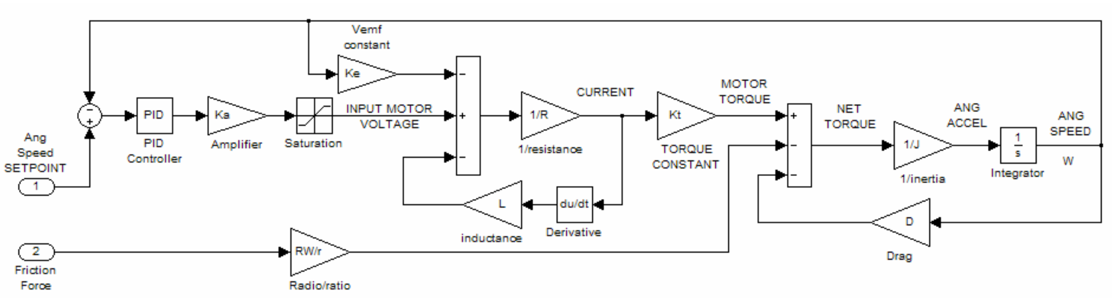

Figure 3.7 Servomotor speed closed loop model

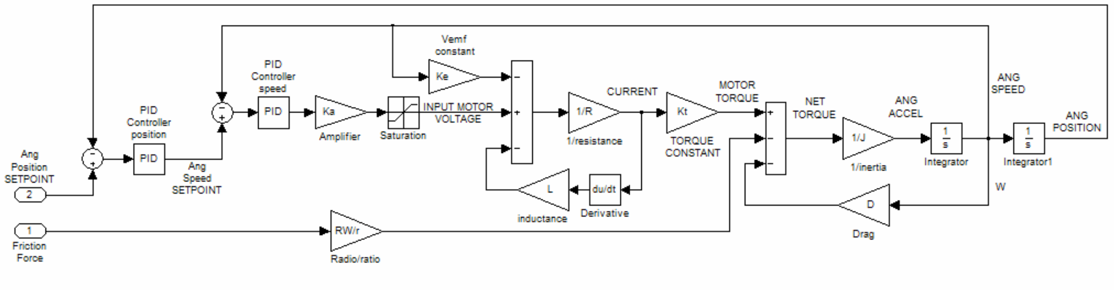

Figure 3.8 Servomotor position and speed closed loop model

In the previous figures the amplifier was represented as a device with a constant gain, in other words it was considered as a linear amplifier. However, the servo amplifiers, utilized in the TFS use a pulse width modulation (PWM) technique. The amplifiers are of the 4-quadrant type, allowing precise control of acceleration and deceleration in both directions. The main difference between a linear amplifier and a PWM amplifier is that the first one changes the input voltage of the motor. On the other hand a switched amplifier uses constant DC motor input voltage but switches it on and off to control power. The switching frequency, normally 20 KHz, is much higher than the servomotor mechanical frequency response. Thus, what the servomotor sees is a variable input power. Therefore, the inclusion of the dynamic response of the PWM does not make sense for the dynamic system simulation, and then a linear amplifier is considered for the driving motor. This example clarifies this functional aspect. For the current research the servomotors nominal voltage is 24v DC and the controller output is ±10v DC. A linear amplifier for this system would have a gain value of 2.4. Therefore, for a 5v controller output, the servomotor input voltage would be 12v. In the PWM amplifier case, the input servomotor voltage is always either 24v or 0v depending if the switch is on or off. For example a 5v controller output would mean 50% of the time on and 50% off, which represents 50% of the power.

3.3 TIRE MODEL

Tire modeling has received much attention in recent years. Friction is the factor that allows torque transfer, which generates movement. As a matter of fact, two realistic applications of friction models are anti-lock braking system (ABS) and traction control in the automotive industry [7], [8].

Empirical data can be easily acquired in labs, however, to obtain accurate analytical tire/ground friction models consistent with the empirical data, has been difficult.

Tire friction models commonly assume that the normalized tire friction coefficient μ

$$\mu = \frac{F_r}{F_N} \qquad \text{Eq. 3.5}$$

is a nonlinear function of the slip between the ground and the tire, the longitudinal wheel velocity, and ground and tire properties.

Curves shown in Figure 3.9 are empirically based on steady state (constant linear and angular velocity) experimental data in highly controlled lab environment with specially designed test vehicles. Therefore, under those particular conditions, experimental data for tires match curves shown in Figure 3.9. However, the friction phenomenon is dynamic and steady state is not commonly reachable in real vehicles and environments.

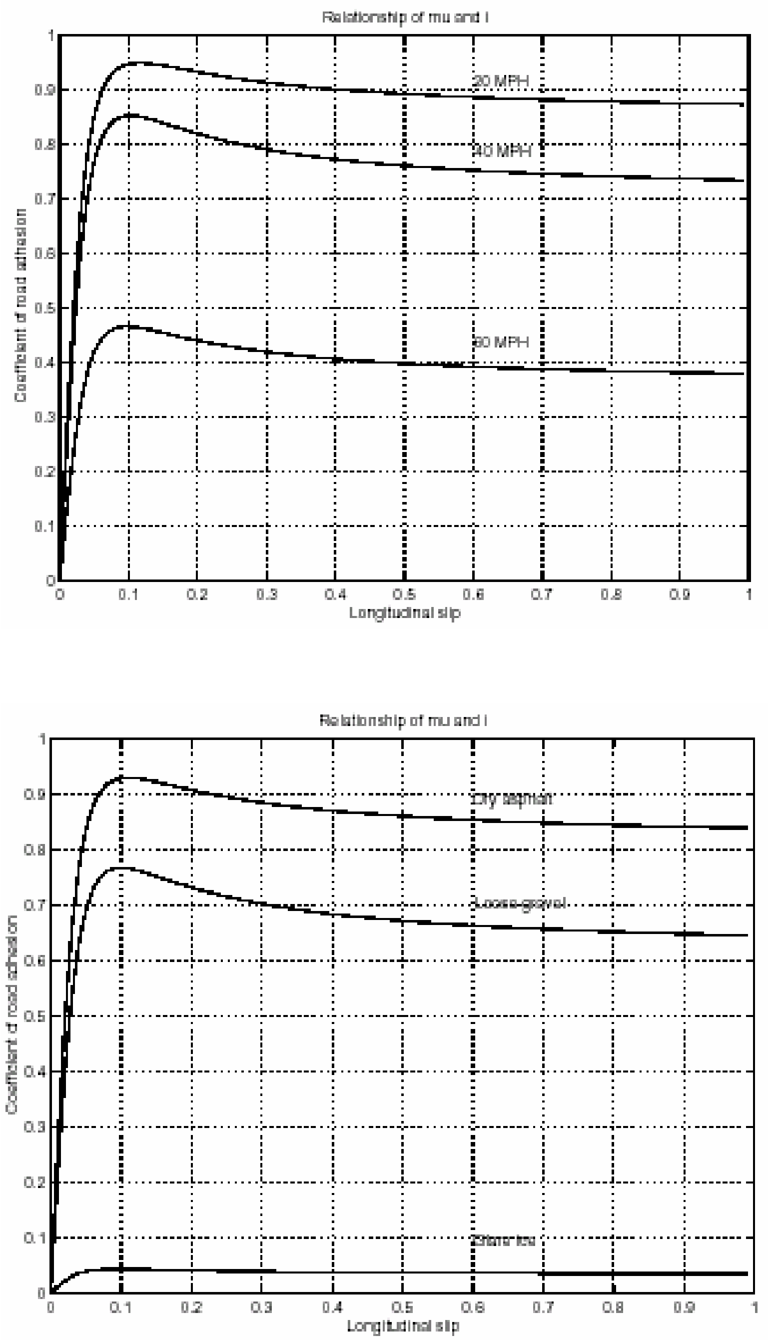

Figure 3.9 Tire friction coefficient as a function of slip, speed, and tire/ground properties, [9]

Before going into further details, some definitions and a review the dynamic model of the wheel should be addressed. Figure 3.2 and equation 3.1 have to be completed with the addition of the tire friction model, represented by Figure 3.10.

Except for F_r, all the variables described in Table 3.3 are known. The aim of this section and the tire model is to find the friction force. For a given ground and tire, the friction force depends only on the speed and the slip. Since the platform will move at low speeds, friction curves similar to 3.9 will not change. Hence, the friction force will only depend in the wheel-platform slip. Slip, noted as s, is defined as follows:

$$s = \frac{(V - \omega * RW)}{\max(|V|, |\omega * RW|)} \qquad \text{Eq. 3.6}$$

It is worth mentioning that the longitudinal velocity *V* is equal to the platform velocity if and only if the platform yaw rate is null.

The relative velocity v_r is defined as:

$$v_r = V - \omega * RW \qquad \text{Eq. 3.7}$$

Table 3.3 Wheel dynamic model parameters

T is the Motor torque after gear box	*V* is the wheel velocity in its longitudinal direction
F_N is the normal force measured by weight scales	ω is the angular velocity of the wheel
F_r is the friction force	RW is the wheel radius

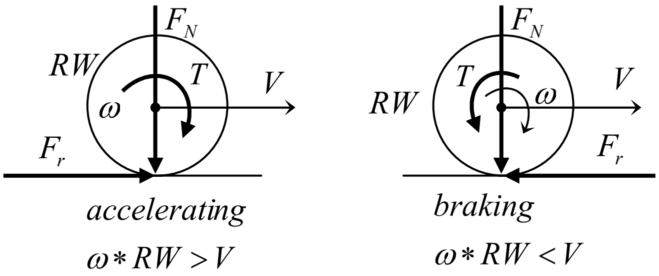

Figure 3.10 Wheel dynamic model

For positive relative velocities, the wheel is braking, the slip is positive, and the friction force is negative making the platform decelerate. For negative relative velocities, the wheel is accelerating, the slip is negative, and the friction force is positive making the platform accelerate.

Four more cases need to be described.

$$\begin{array}{l} sign(V) \neq sign(\omega) \quad then \quad s = \pm 1 \quad sliding \\ V = 0 \quad \omega \neq 0 \quad then \quad s = \pm 1 \quad spinning \\ \omega = 0 \quad V \neq 0 \quad then \quad s = \pm 1 \quad sliding \\ V = \omega = 0 \quad then \quad s = 0 \quad stopped \end{array} \qquad \text{Eq. 3.8}$$

Several tire models have been developed to predict how the friction force depends on the tire-ground parameters and particularly on the slip, s, Burckhardt, Kiencke and Daiss, Dugoff, LuGre. For a comprehensive discussion about static and dynamic friction models refer to [9]. Among them, the most used is the "Magic Formula" developed by Pacejka [10]. The friction force equation for this model is:

$$F(s) = D * \sin[C * \arctan(B * s - E * [B * s - \arctan(B * s)])] \qquad \text{Eq. 3.9}$$

Parameters B, C, D and E are defined in Table 3.4.

These static friction models are good for steady state conditions at the linear and angular velocities. This steady-state circumstance is seldom real, especially when the vehicle goes through continuous acceleration and braking phases, like in the platform case. Recently, dynamic friction models, which predict the friction force for unsteady speed conditions, have been developed as an alternative to the static friction models [9]. Either static or dynamic models are highly complicated and require precise tire and ground parameters identification, which is beyond the scope of this thesis.

Table 3.4 Magic formula parameters

B stiffness factor	D peak factor
C shape factor	E curvature factor

Therefore, a linear tire model is going to be considered, similar to simplification done in [5]. The linear tire model will give us a first approach to use at the system dynamic model. This first approximation will let us compare the dynamic versus the kinematic control approaches with minor tire properties knowledge. Subsequently, the advantages of the dynamic control model can be compared to the kinematic.

Then, the force characteristic equation for low slip ratios is:

$$F_r = \frac{-F_N * C * s}{S_{MAX}} \qquad for \quad |s| < |S_{MAX}|$$
$$F_r = -F_N * C * \operatorname{sgn}(V - \omega * RW) \qquad for \quad |s| > |S_{MAX}| \qquad \text{Eq. 3.10}$$

The constant C is determined by the actual tire-ground environment and is named "platform friction coefficient" for the purposes of this thesis. Hence, the friction plot as a function of the slip looks like Figure 3.11.

Figure 3.12 and 3.13 show the Simulink models for the slip and friction force calculation in accordance with equations 3.6, 3.8, and 3.10.

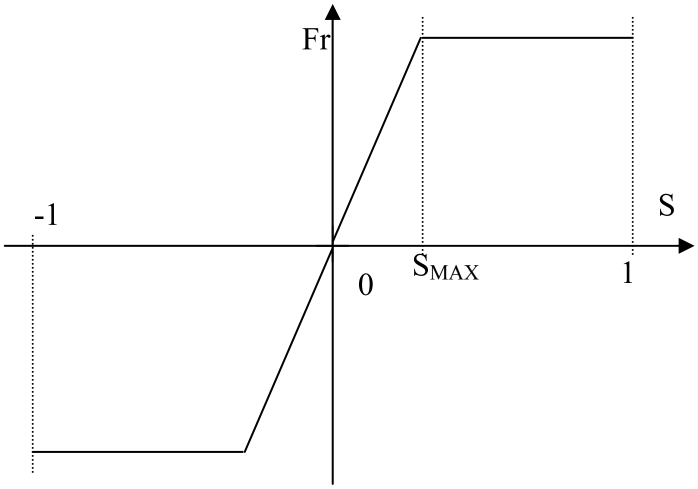

Figure 3.11 Friction vs. Slip

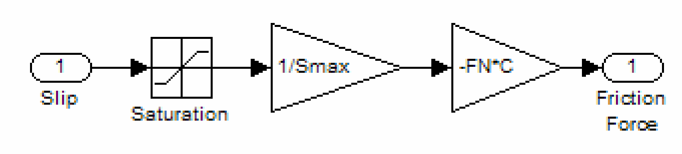

Figure 3.12 Friction Simulink diagram

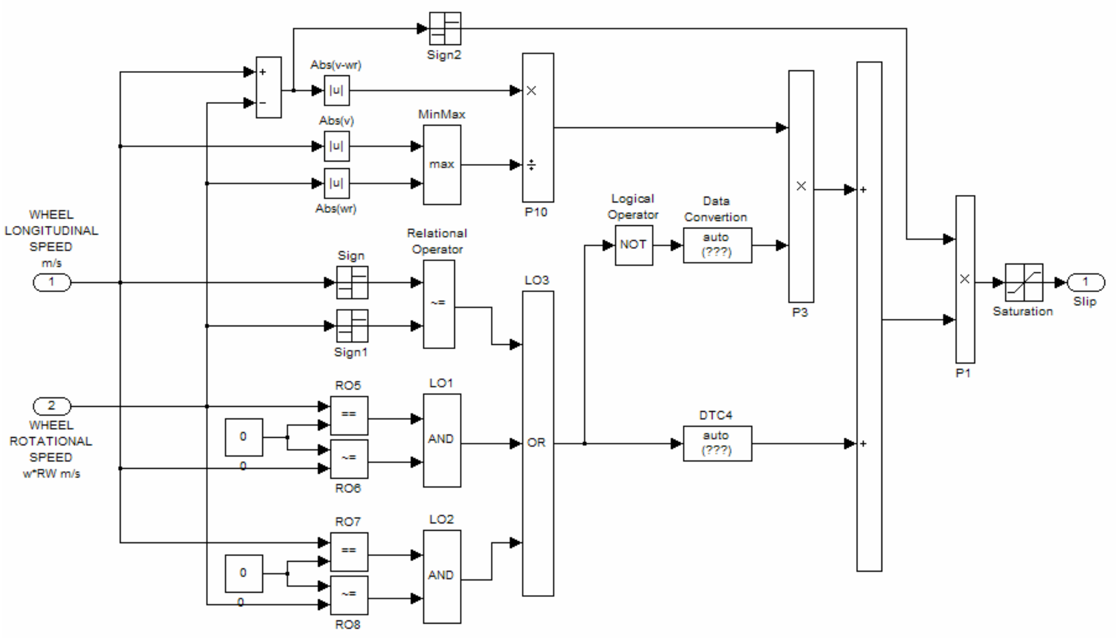

Figure 3.13 Slip Simulink diagram

Chapter 4. System control

The objective of this chapter is to describe the control architecture proposed for the system. Kinematic and dynamic models presented in chapter 2 are put together with the servomotor and tire models in two single kinematic and dynamic control architectures.

4.1 LINEAR TRANSLATIONAL MODE CONTROL

In the previous sections, DC servomotor model, load, speed and position closed loops were presented. Subsequently, a tire model was introduced. This section presents the control loop for the forward translational mode and lateral translational mode tracking schemes showed in Figure 4.1, implementing the dynamic and kinematic control models studied in Chapter 2.

To finally complete the tracking system control loop, two new devices must be introduced to the system; a device to sense the distance from the platform to the subject, and a controller to keep that distance close to its set point value.

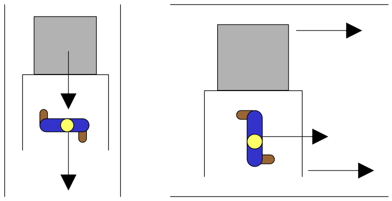

Figure 4.1 Translational modes

4.1.1 Kinematic control

In the kinematic control, the distance controller output is the servomotors' speed set point. The distance controller adjusts the servomotors' speed to control the subject-platform distance to the distance set point. This model assumes no slip, which implies that the wheel speed is equivalent to the platform speed, $v=\omega * RW$. This statement has two main consequences. The first one is that since this assumption is not accurate, the controller will have to overcome this error. It is worth mentioning that commonly, slip value is between 0% and 10%. Thus, we can consider a mean error of 5% in the speed, which represents the model deficiency that the controller has to overcome. The second consequence only affects the simulation. Since the slip is null, the friction at the wheel is 0, which means that the motor has no load and only has to overcome the inertia. To fix this situation, only for simulation purposes, a constant friction value will be set. Friction is linear with slip and slip varies as time passes. Assuming slip has a mean of 5% and considering the tire model represented by Equation 3.10, the friction model for the motor load will be modeled as:

$$F_r = -F_N * C * 0.5 * \operatorname{sgn}(V) \qquad \text{Eq. 4.1}$$

Figure 4.2 shows the kinematic system control loop for the translational mode. It is worth mentioning that the only difference that may exist between wheel 1 (top section of Figure 4.2), and wheel 3 (bottom section of Figure 4.2) models is the normal force at the wheel. In the case of unbalanced normal forces or different wheel linear velocities, the generated friction forces will be different.

Finally, Figure 4.3 shows the functional architecture for the kinematic closed loop control. Three controllers compose the system. One central stand-off distance controller is used to control the subject-platform distance, and two extra controllers are used for speed control of each servo wheel.

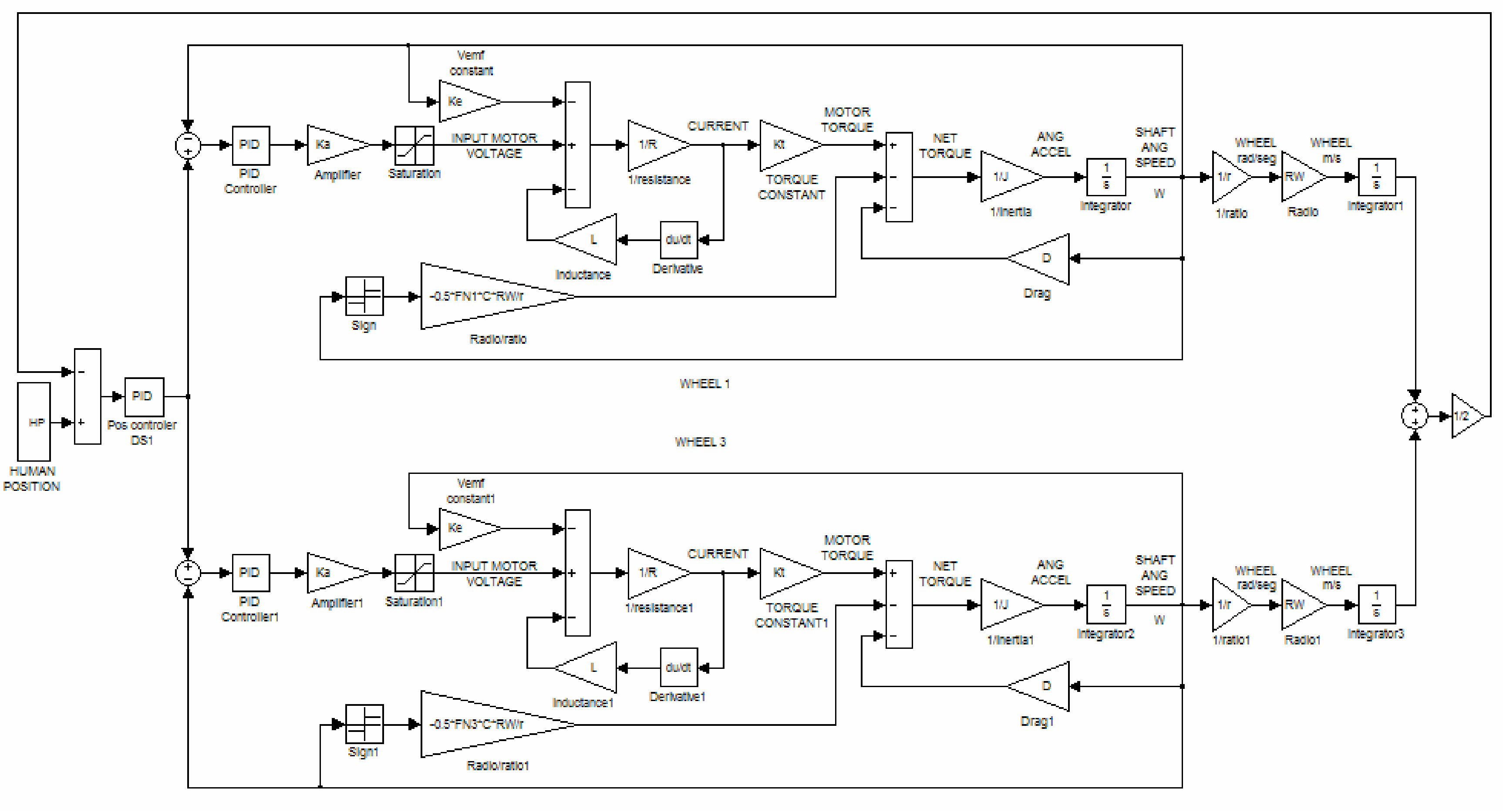

Figure 4.2 Kinematic system control loop for Translational mode

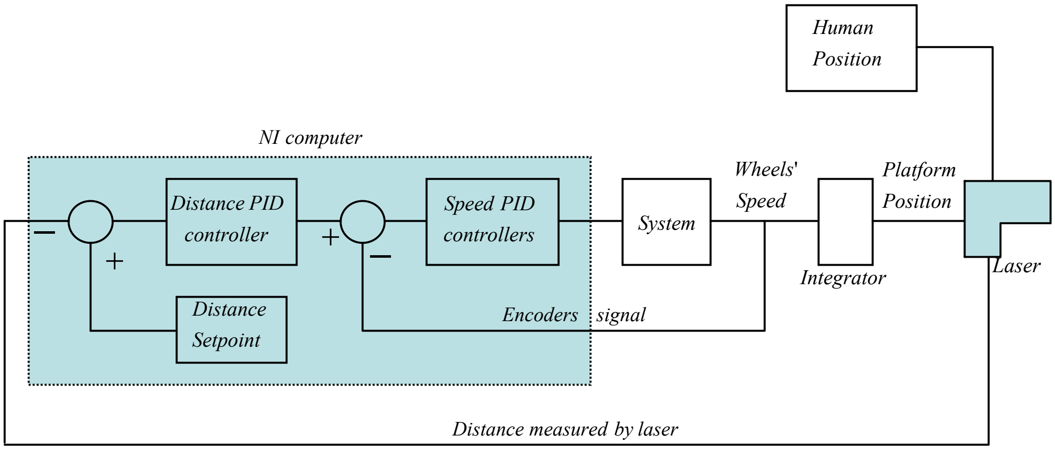

Figure 4.3 Functional architecture for kinematic closed loop control

4.1.2 Dynamic control

For the dynamic model, the system model also includes the direct and inverse dynamics diagrams described subsequently.

First the longitudinal velocity at each wheel must be computed in order to calculate the slip at each wheel. From this point forward, if acceleration, speed and position do not show a sub index, then they refer to point P. The speed of any point R at the platform can be calculated as a function of its distance to the reference point P, the platform yaw rate and the reference point velocity.

$$\vec{V}_R = \vec{V}_P + \omega\vec{z} \wedge (R - P)$$

Designating wheel 1 as W1, wheel 3 as W3 and considering distance given in Figure 2.20:

$$\begin{pmatrix} u_{W1} \\ v_{W1} \end{pmatrix} = \begin{pmatrix} u \\ v \end{pmatrix} + \begin{pmatrix} \omega * Lr \\ -\omega * Fr \end{pmatrix}$$

$$\begin{pmatrix} u_{W3} \\ v_{W3} \end{pmatrix} = \begin{pmatrix} u \\ v \end{pmatrix} + \begin{pmatrix} -\omega * Lf \\ \omega * Ff \end{pmatrix}$$

If steering is not considered, then the longitudinal velocity of each wheel is in the direction of x_{rel}, and then the longitudinal velocities at each wheel are u_{W1} and u_{W3} respectively.

$$\begin{aligned} V1 &= u_{W1} = u + \omega * Lr \\ V3 &= u_{W3} = u - \omega * Lf \end{aligned} \qquad \text{Eq. 4.2}$$

- Inverse Dynamics

The main idea of the control system is to vary each driving wheel rotational speed to accomplish null platform yaw rate and acceleration, and to keep platform-subject distance error at minimum.

Operating at equation 2.26, to achieve null yaw acceleration:

$$F'_{1X} * \left(Lr - L_{GC}\right) = F'_{3X} * \left(Lf + L_{GC}\right) \qquad \text{Eq. 2.26}$$

Writing the friction force at wheel 1 as a function of the friction force at wheel 3:

$$F'_{1X} = F'_{3X} * \frac{\left(Lf + L_{GC}\right)}{\left(Lr - L_{GC}\right)} \qquad \text{Eq. 4.3}$$

Similarly, writing the friction force at wheel 3 as a function of the friction force at wheel 1:

$$F'_{3X} = F'_{1X} * \frac{\left(Lr - L_{GC}\right)}{\left(Lf + L_{GC}\right)} \qquad \text{Eq. 4.4}$$

Operating at equation 2.25 with null yaw acceleration, the accelerations in the forward and lateral direction are:

$$\begin{pmatrix} \dot{u} \\ \dot{v} \end{pmatrix} = \begin{pmatrix} \dfrac{F'_{1X} + F'_{3X}}{m} + \omega^2 * F_{GC} - \omega * v \\ \omega^2 * L_{GC} + \omega * u \end{pmatrix} \qquad \text{Eq. 4.5}$$

In the forward direction, the friction forces are replaced with equations 4.3 and 4.4, and the next equations are obtained respectively:

$$\dot{u} = \frac{F'_{3X} * \dfrac{(Lf + L_{GC})}{(Lr - L_{GC})} + F'_{3X}}{m} + \omega^2 * F_{GC} - \omega * v \qquad \text{Eq. 4.6}$$

$$\dot{u} = \frac{F'_{1X} + F'_{1X} * \dfrac{(Lr - L_{GC})}{(Lf + L_{GC})}}{m} + \omega^2 * F_{GC} - \omega * v \qquad \text{Eq. 4.7}$$

Writing the friction forces as a function of other parameters:

$$F'_{3X} = \frac{m * \left(\dot{u} - \omega^2 * F_{GC} + \omega * v\right)}{1 + \dfrac{(Lf + L_{GC})}{(Lr - L_{GC})}} \qquad \text{Eq. 4.8}$$

$$F'_{1X} = \frac{m * \left(\dot{u} - \omega^2 * F_{GC} + \omega * v\right)}{1 + \dfrac{(Lr - L_{GC})}{(Lf + L_{GC})}} \qquad \text{Eq. 4.9}$$

Operating again and using equation 3.12 $\underline{(F_r = -F_N * C * s / S_{MAX})}$:

$$\frac{-F_{3N} * C * s_3}{S_{MAX}} = \frac{m * \left(\dot{u} - \omega^2 * F_{GC} + \omega * v\right) * (Lr - L_{GC})}{Lr + Lf} \qquad \text{Eq. 4.10}$$

$$\frac{-F_{1N} * C * s_1}{S_{MAX}} = \frac{m * \left(\dot{u} - \omega^2 * F_{GC} + \omega * v\right)(Lf + L_{GC})}{Lf + Lr} \qquad \text{Eq. 4.11}$$

Replacing the slip at each tire by its analytical representation, equation 3.6, the following equations are obtained:

$$\frac{-F_{3N} * C}{S_{MAX}} * \frac{(V_3 - \omega_3 * RW)}{\max\left(|V_3|, |\omega_3 * RW|\right)} = \frac{m * \left(\dot{u} - \omega^2 * F_{GC} + \omega * v\right) * (Lr - L_{GC})}{Lr + Lf} \qquad \text{Eq. 4.12}$$

$$\frac{-F_{1N} * C}{S_{MAX}} * \frac{(V_1 - \omega_1 * RW)}{\max\left(|V_1|, |\omega_1 * RW|\right)} = \frac{m * \left(\dot{u} - \omega^2 * F_{GC} + \omega * v\right)(Lf + L_{GC})}{Lf + Lr} \qquad \text{Eq. 4.13}$$

Writing the wheel rotational speed as a function of the other parameters:

$$\omega_3 = \frac{V_3}{RW} + \frac{m*\left(\dot{u} - \omega^2 * F_{GC} + \omega * v\right)* S_{MAX} * \left(Lr - L_{GC}\right)* \max\left(\left|V_3\right|, \left|\omega_3 * RW\right|\right)}{F_{3N} * C * \left(Lr + Lf\right)* RW}$$

$$\omega_1 = \frac{V_1}{RW} + \frac{m*\left(\dot{u} - \omega^2 * F_{GC} + \omega * v\right)* S_{MAX} * \left(Lf + L_{GC}\right)* \max\left(\left|V_1\right|, \left|\omega_1 * RW\right|\right)}{F_{1N} * C * \left(Lr + Lf\right)* RW}$$

Writing all the constants as a single constant K$_1$ and K$_3$ respectively

$$\omega_3 = \frac{V_3}{RW} + K_3 * \left(\dot{u} - \omega^2 * F_{GC} + \omega * v\right)* \max\left(\left|V_3\right|, \left|\omega_3 * RW\right|\right) \qquad \text{Eq. 4.14}$$

$$\omega_1 = \frac{V_1}{RW} + K_1 * \left(\dot{u} - \omega^2 * F_{GC} + \omega * v\right)* \max\left(\left|V_1\right|, \left|\omega_1 * RW\right|\right) \qquad \text{Eq. 4.15}$$

The rotational speed at wheel 1, ω$_1$, and wheel 3, ω$_3$, defined by equation 4.14 and equation 4.15, accomplish null yaw acceleration and desired platform acceleration. To compute the rotational speed, the previous rotational speed value is utilized. Writing equation 4.14 and 4.15 in Simulink, Figure 4.4 is built.

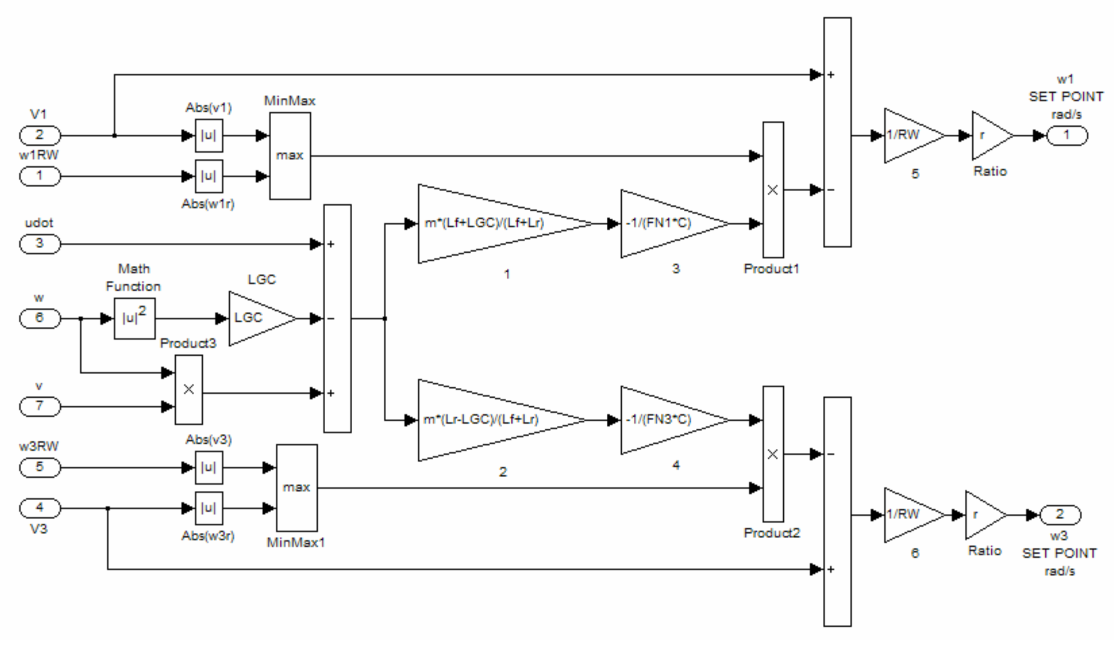

Figure 4.4 Inverse platform Dynamics

- Direct Dynamics

Direct dynamics is shown by directly applying equations 2.24, 2.25 and 3.10:

$$\ddot{\theta} = \frac{F'_{1X} * \left(Lr - L_{GC}\right) - F'_{3X} * \left(Lf + L_{GC}\right)}{I_{GC}} \tag*{Eq. 2.24}$$

$$\begin{pmatrix} \dot{u} \\ \dot{v} \end{pmatrix} = \begin{pmatrix} \dfrac{F'_{1X} + F'_{3X}}{m} + \ddot{\theta} * L_{GC} + \omega^2 * F_{GC} - \omega * v \\ -\ddot{\theta} * F_{GC} + \omega^2 * L_{GC} + \omega * u \end{pmatrix} \tag*{Eq. 2.25}$$

$$F_r = \frac{-F_N * C * s}{S_{MAX}} \tag*{Eq. 3.10}$$

Operating the last equations:

$$\ddot{\theta} = \frac{-F_{N1} * C * s_1 * \left(Lr - L_{GC}\right) + F_{N3} * C * s_3 * \left(Lf + L_{GC}\right)}{I_{GC} * S_{MAX}} \tag*{Eq. 4.16}$$

$$\begin{pmatrix} \dot{u} \\ \dot{v} \end{pmatrix} = \begin{pmatrix} \dfrac{-F_{N1} * C * s_1 - F_{N3} * C * s_3}{m * S_{MAX}} + \ddot{\theta} * L_{GC} + \omega^2 * F_{GC} - \omega * v \\ -\ddot{\theta} * F_{GC} + \omega^2 * L_{GC} + \omega * v \end{pmatrix} \tag*{Eq. 4.17}$$

Writing these two last equations in Simulink, Figure 4.5 is built. Figure 4.6 shows the dynamic system control loop for the translational mode.

In Figure 4.6 the PID block multiplies the error distance, computing the necessary forward acceleration to minimize the distance error. A saturation block to limit the desired platform acceleration is placed after the PID stand-off distance controller. The reason to limit the desired platform acceleration is that the traction force developed by the tire-ground surface is non-linear as showed by Figure 4.2. Thus, the traction force has a maximum value inherent to the ground conditions for a given tire type. Therefore, the platform force in the forward direction also has a maximum, and then a maximum platform forward acceleration. If the desired forward acceleration computed by the PID controller is greater than the maximum platform acceleration achievable

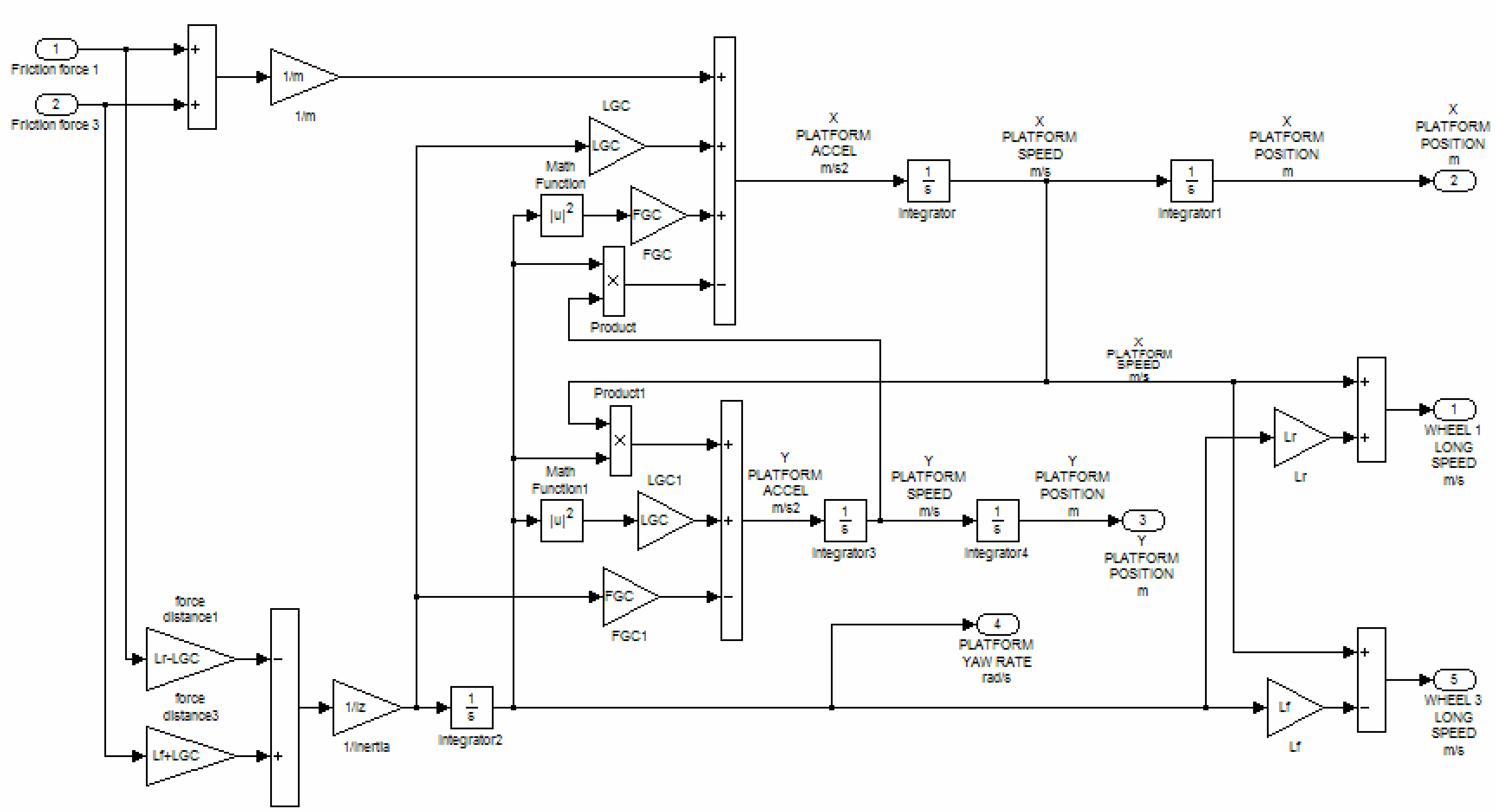

Figure 4.5 Direct platform Dynamics

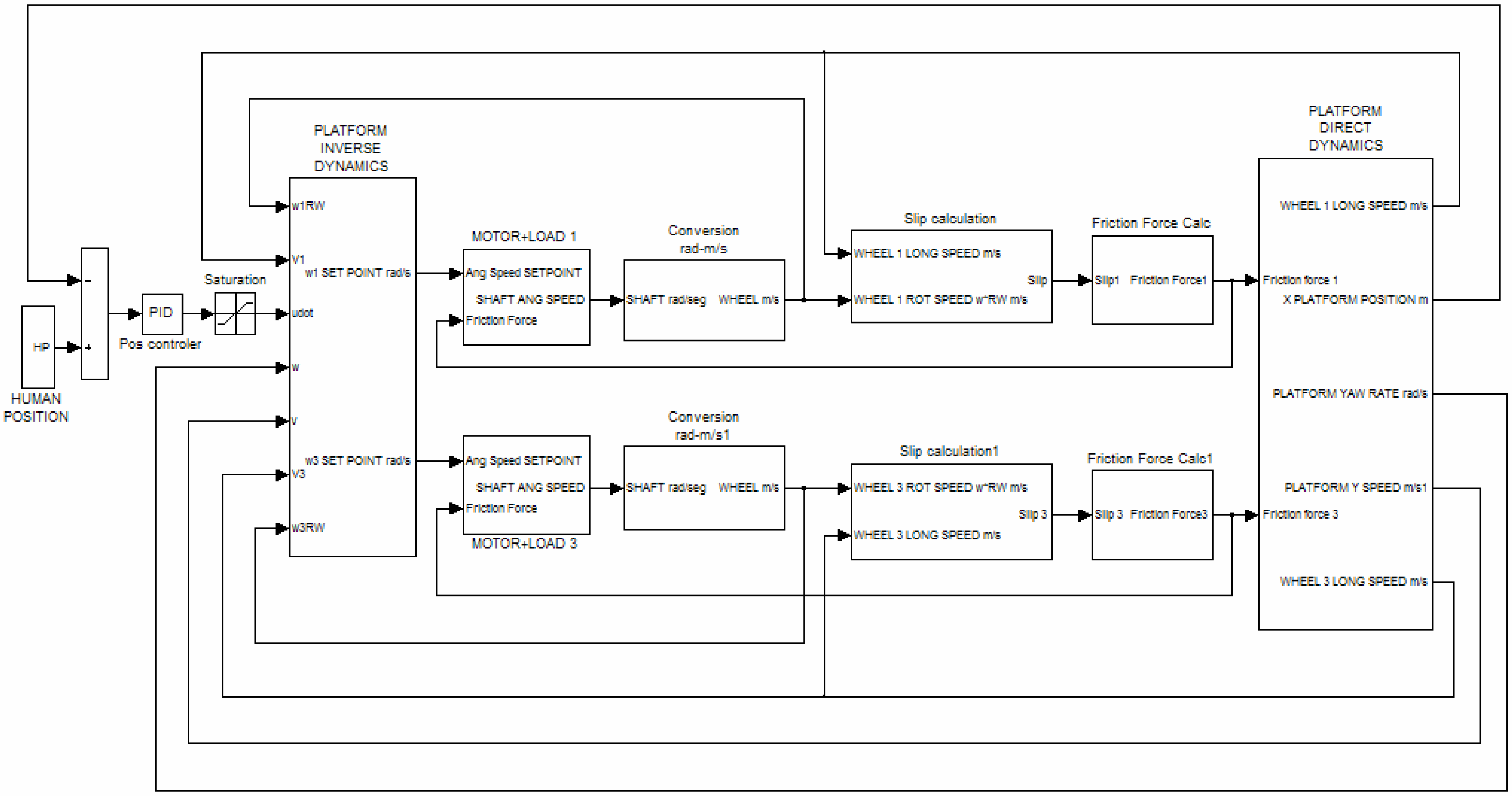

Figure 4.6 Dynamic system control loop for Translational mode

then the rotational speed computed by the inverse dynamic algorithm will not be able to develop the desired force. Consequently, neither the desired acceleration nor the null yaw acceleration would be attained. The next equations describe this fact. From equation 3.10 and equation 2.25 the maximum forward acceleration achievable by the platform is when the slip is 1:

$$\dot{u}_{MAX} = \frac{F_{1N} * C + F_{3N} * C}{m * S_{MAX}} + \ddot{\theta} * L_{GC} + \omega^2 * F_{GC} - \omega * v \qquad \text{Eq. 4.18}$$

Since the terms in function of the yaw rate and acceleration are null or much smaller than the traction forces, the maximum achievable acceleration is:

$$\dot{u}_{MAX} = \frac{\left(F_{1N} + F_{3N}\right) * C}{m * S_{MAX}} \qquad \text{Eq. 4.19}$$

Figure 4.5 includes a subject position block to generate diverse subject walking patterns, and also includes a conversion block diagram which converts the motor shaft rotational speed into the wheel rotational speed in meters per second. Both block diagrams are detailed in Figures 4.7 and 4.8 respectively. The other block diagrams shown in Figure 4.5 were previously illustrated.

Finally, Figure 4.9 shows the functional architecture for the kinematic closed loop control. Three controllers compose the system; one central controller is used for the subject-platform distance, and two extra controllers for speed control of each servo wheel.

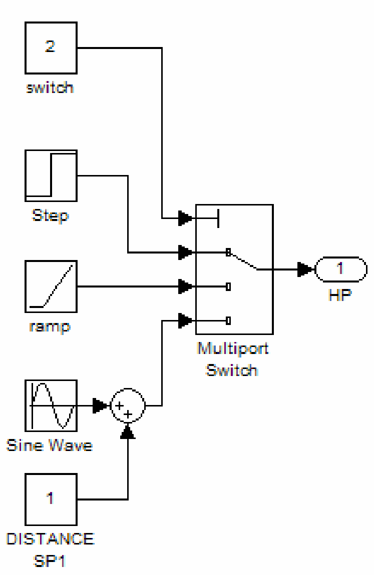

Figure 4.7 Subject walking pattern

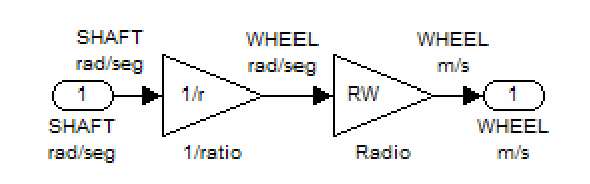

Figure 4.8 Conversion block diagram

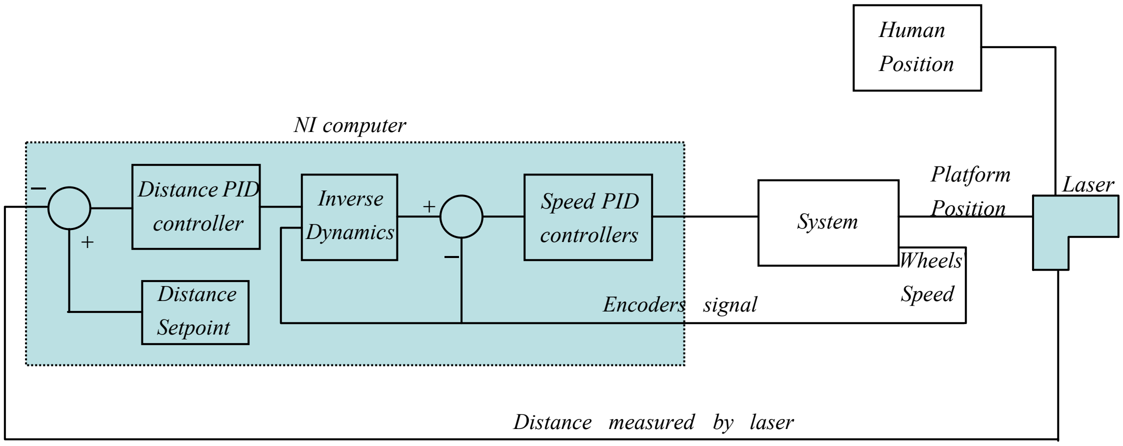

Figure 4.9 Functional architecture for dynamic control loop

Chapter 5. Simulation results and analysis

Previous chapters introduced the dynamic and kinematic models of the system. The objective of this chapter is to present the simulation results carried on in Simulink to see the response of the system control design. This chapter first presents results for the kinematic control scheme for the linear translational mode. Finally, the results for the dynamic control scheme for the linear translational mode will be presented.

5.1 SIMULATION APPROACH

Models were developed and run in Simulink. Due to the existence of nonlinear elements, the model was run with a fixed step size and continuous solver. The step size was decreased until no variation of the output variables was observed, since a greater decrease in the step size only results in computing-time increment. A Simulink model specifies the time derivatives of its continuous states but not the values of the states themselves. Thus, when simulating a system, Simulink computes continuous states by numerically integrating their state derivatives by an ordinary differential equation (ODE) solver. The step size was established at 0.001 for the kinematic scheme and 0.0001 for the dynamic scheme since the latter needed a smaller step size. The solver chosen was Simulink's most accurate, ode5 Dormand-Prince.

5.2 SIMULATION RESULTS FOR KINEMATIC CONTROL OF THE LINEAR TRANSLATIONAL MODE

The Simulink model used for the simulation is the one represented in the last chapter by Figure 4.2, reviewed in Figure 5.1.

Model parameters like motor inductance, wheel radius, etc. are illustrated in Chapter 6. Subject movement will now be considered. At time 0 the subject begins walking at a constant speed of 0.5 m/s until time is 10 seconds, when she/he stops. Figure 5.2 is the subject movement showed as a distance-time plot.

The kinematic model simulation predicts the system response shown in Figure 5.3 when the subject movement pattern is the one shown in Figure 5.2.

Figure 5.4 shows the motor speed set point and the motor and wheel speed, which are related by the gear ratio and the wheel radius. It can be seen that after the subject stops walking after 10 seconds, the speed set point position goes to 0. However, plots show that the servomotor speed oscillates between –100 RPM and 100 RPM. In Figure 5.1 it can be observed that the motor external load and tire friction force, was assumed to have constant value with direction opposite to wheel speed. Behavior shown in the last figure is the cause of this friction modeling. In fact, when the stand-off distance error goes to 0, the speed set point also goes to 0. The modeling deficiency happens when the servomotor speed, almost 0, inverts direction. At that time, the external load also reverses, applying full load to the motor and producing a new speed and distance tracking error. The error is again reduced to 0, but if the wheel speed switches direction, even at infinitesimal speed values, the full load is again applied to the servomotor shaft in the reverse direction, generating a new speed error and the cycle repeats indefinitely.

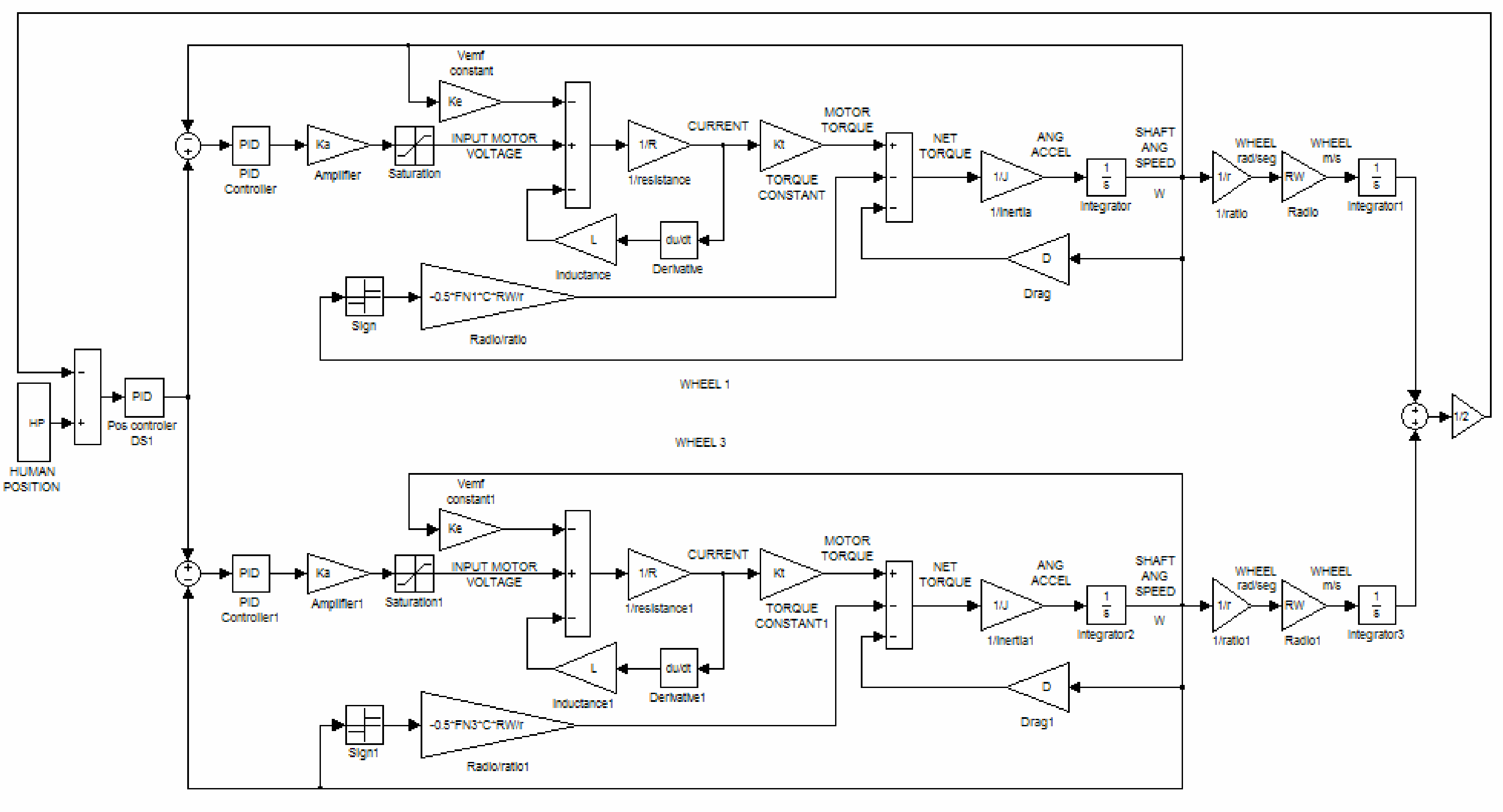

Figure 5.1 (Figure 4.2) Kinematic system control loop for Translational mode

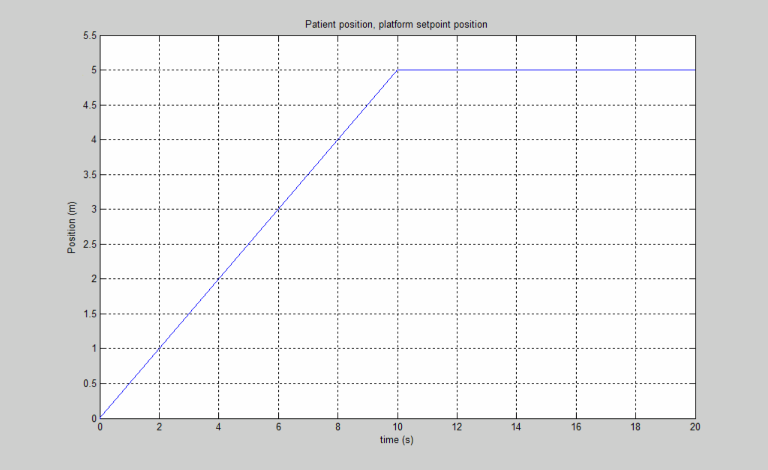

Figure 5.2 Subject movement

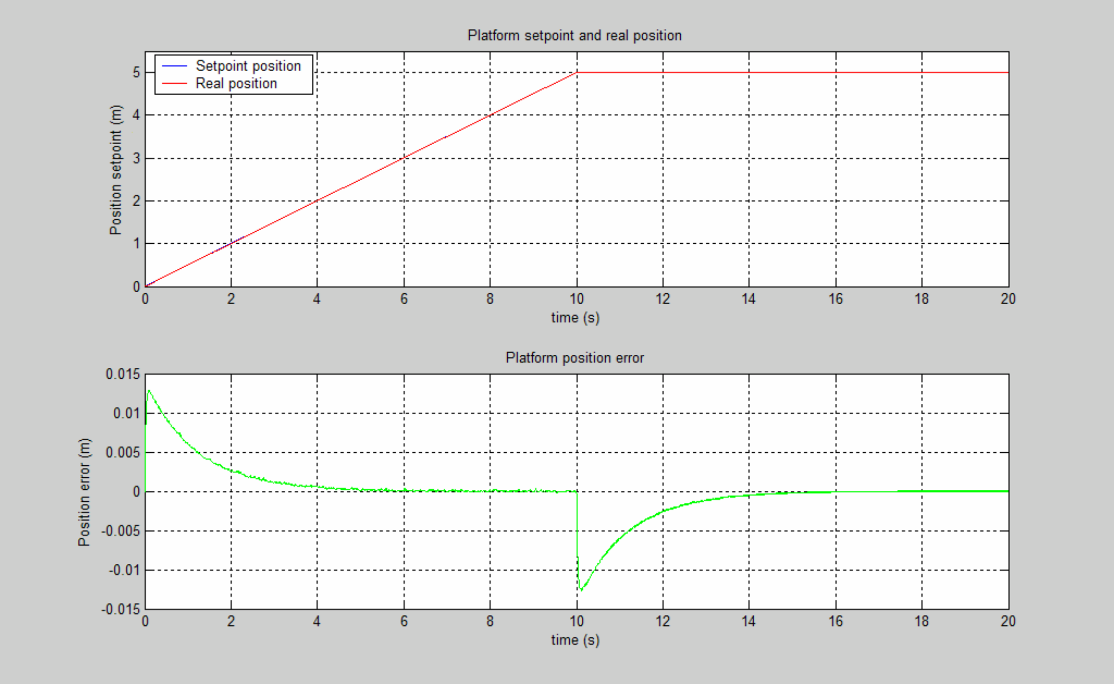

Figure 5.3 Kinematic platform control system response

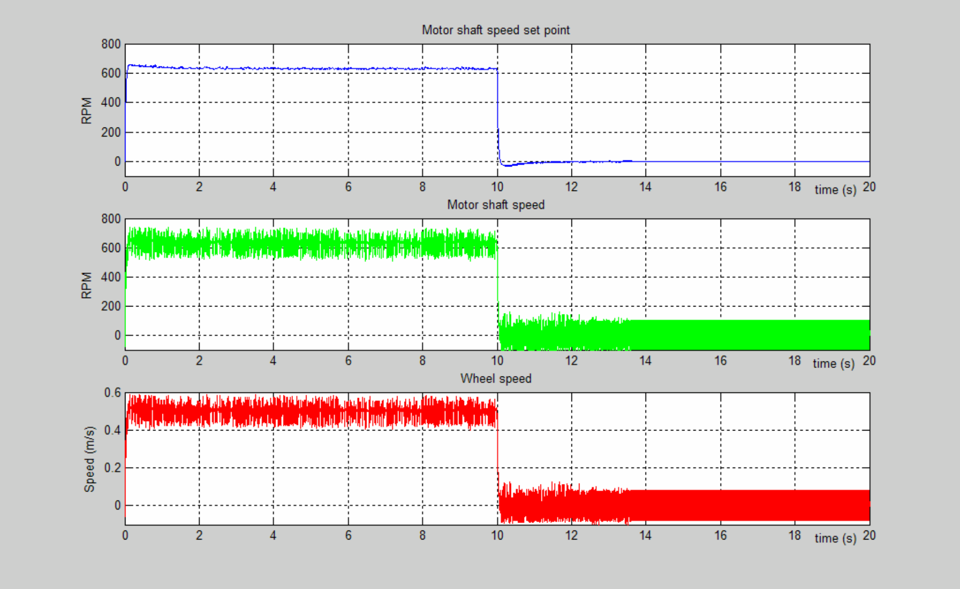

Figure 5.4 Motor speed set point, and motor and wheel speeds

Figure 5.2, 5.3 and 5.4 show the system response for given controller parameter values, Ki, Kd, and Kp. Those parameters were chosen after various simulation runs considering fast responses, stability and no-bumping conditions. It is worth mentioning that during simulations both servomotors ran at the same speed, even having different friction forces applied to them. Finally, the system simulation shows that the system could track the subject to within 3/4 inches, much better than required.

5.3 SIMULATION RESULTS FOR DYNAMIC CONTROL OF THE LINEAR TRANSLATIONAL MODE

The Simulink model used for the simulation is the one represented in the last chapter and showed by Figure 5.5. The subject movement pattern for this simulation is the same as the pattern used in the last section. The dynamic model simulation results are presented in Figure 5.6, which shows subject and platform movements and in addition to the tracking error.

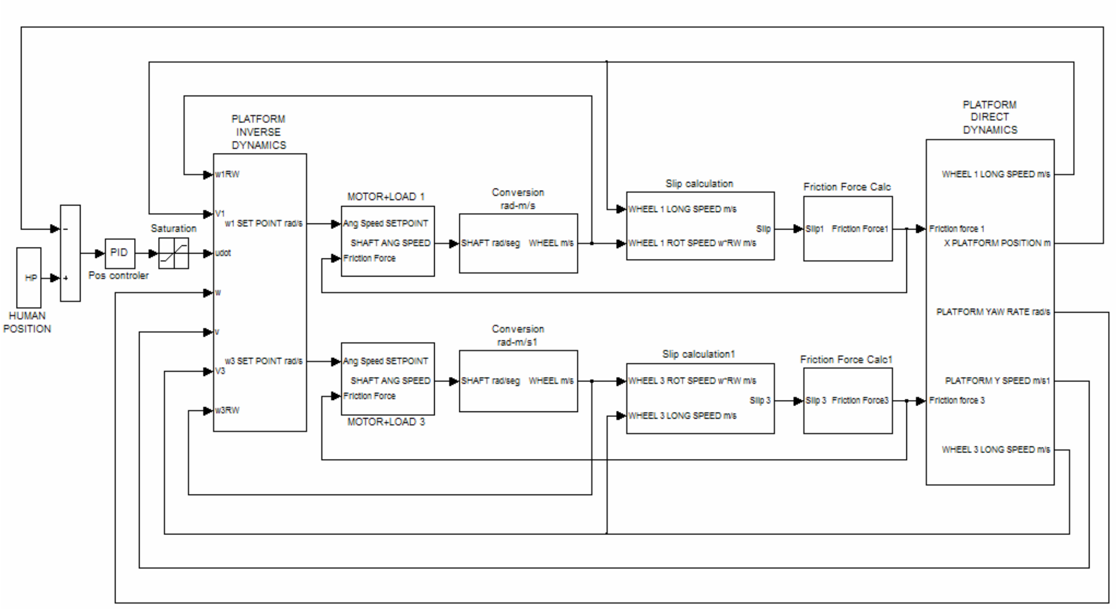

Figure 5.5 Dynamic system control loop for Translational mode (Figure 4.5)

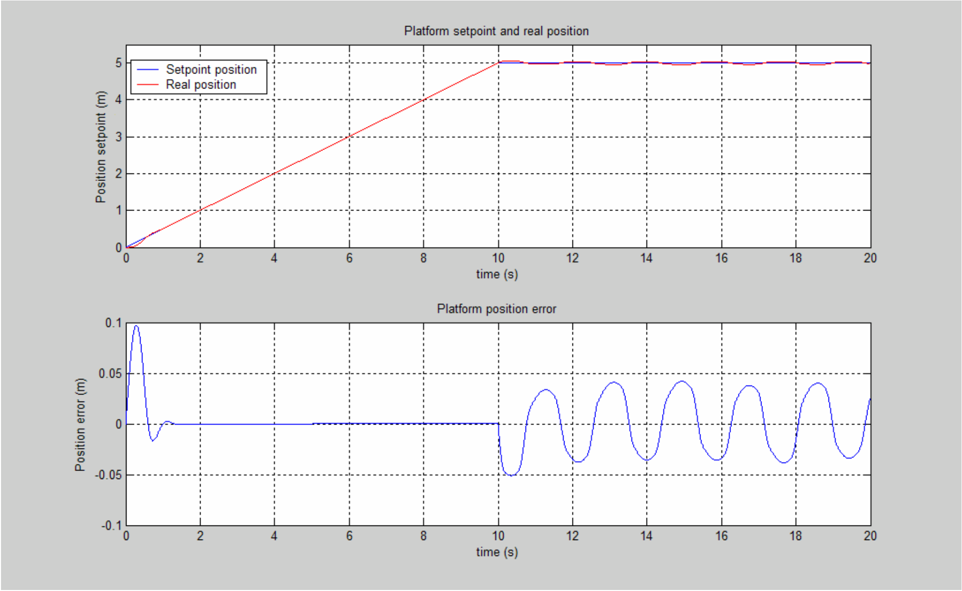

Figure 5.6 Dynamic platform control system response

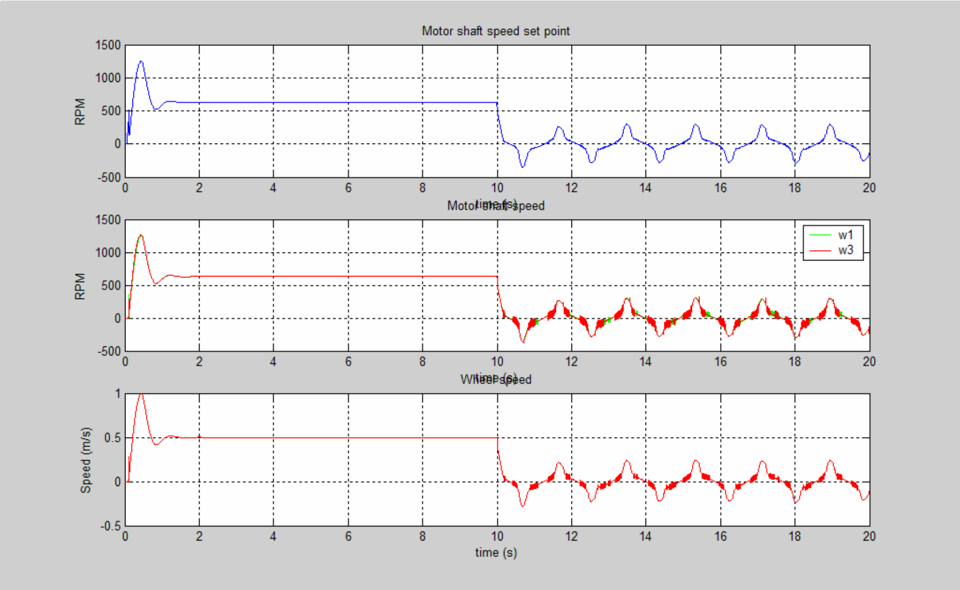

Figure 5.7 Servomotors and wheel speed

Figure 5.7 shows the motor and wheel speed, which are related by the gear ratio and the wheel radius. Figures 5.6 and 5.7 show that while the subject is walking, the tracking error is kept at values lower than 0.1 meter. After the subject stops, the platform maintains the tracking error at reduced values. However, plots show that the platform never stops moving. The cause of this behavior is the friction/tire model considered. In previous chapters the tire model was defined by equation 3.10 as:

$$\begin{aligned} F_r &= \frac{-F_N * C * s}{S_{MAX}} && \textit{for} \quad s < S_{MAX} \\ F_r &= -F_N * C * \operatorname{sgn}(V - \omega * RW) && \textit{for} \quad s > S_{MAX} \end{aligned} \qquad \text{Eq. 3.10}$$

The slip s is defined by equations 3.6 and 3.8

$$s = \frac{(V - \omega * RW)}{\max(|V|, |\omega * RW|)} \qquad \text{Eq. 3.6}$$

$$\begin{aligned} & \mathit{sign}(V) \neq \mathit{sign}(\omega) \quad \textit{then} \quad s = \pm 1 \quad \textit{sliding} \\ & V = 0 \quad \omega \neq 0 \quad \textit{then} \quad s = \pm 1 \quad \textit{spinning} \\ & \omega = 0 \quad V \neq 0 \quad \textit{then} \quad s = \pm 1 \quad \textit{sliding} \\ & V = \omega = 0 \quad \textit{then} \quad s = 0 \quad \textit{stopped} \end{aligned} \qquad \text{Eq. 3.8}$$

The reason for this behavior is that when the subject stops, platform speed V and wheel speed ω∗RW decrease. While both speeds are positive, the model simulation result is correct. However, at some moment the error has decreased and both speeds are close to 0. Some time after that, one of the speeds switches direction. Then, by the slip definition given by equation 3.8, the slip becomes 1 or –1. Thus, by equation 3.10, full load is applied to both platform and motor. This high and sudden load makes the platform and motor accelerate and then increases the tracking error. The cycle repeats indefinitely, finally producing the steady state error shown in Figure 5.6. To exemplify the fact previously addressed, Figure 5.8 shows the slip at one of the wheels. The kinematic model in the proximity of null speeds also showed similar behavior. However, in that case, the load was only applied to the motor, while in this case it is also applied to the platform. It is worth mentioning that such behavior is not expected as real since it is a product of a deficiency of the model at reduced speeds.

Finally, one of the problems encountered during the simulation of the dynamic model was in the first steps of the model. The dynamic control loop sets the wheel speed as a function of the actual wheel speed. Hence, if at any instant, V_3 and ω_3 are null, then the set point speed will be null as well.

$$\omega_3 = \frac{V_3}{RW} + K_3 * \left(\dot{u} - \omega^2 * F_{GC} + \omega * v\right) * \max\left(\left|V_3\right|, \left|\omega_3 * RW\right|\right) \qquad \text{Eq. 4.14}$$

$$\omega_1 = \frac{V_1}{RW} + K_3 * \left(\dot{u} - \omega^2 * F_{GC} + \omega * v\right) * \max\left(\left|V_1\right|, \left|\omega_1 * RW\right|\right) \qquad \text{Eq. 4.15}$$

The simulation begins at time 0, and at the initial step, V1, ω1 and V3, ω3 are 0. Thus, it does not matter how much the stand-off distance controller sets the desired platform acceleration, since the wheel speed set point will be 0. To overcome this problem a small modification was introduced at the inverse dynamic algorithm, which computes the driving wheel set point speeds. A kinematic term was incorporated, which only

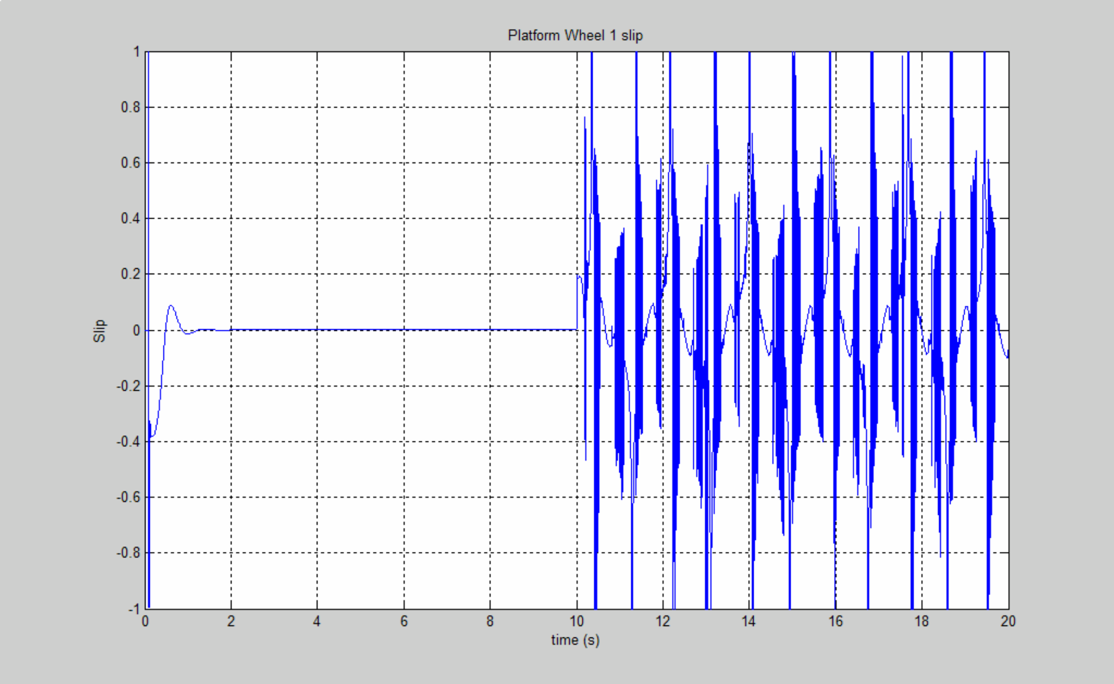

Figure 5.8 Wheel slip

acts when the dynamic speed set point is less than 0.1 m/s and the tracking error is greater than 0.05 m. Under these conditions, the kinematic term adds a term to the dynamic speed calculation that is directly proportional to the actual distance tracking error. The reason to add the kinematic term for speeds lower than 0.1 m/s and not only when the speed is null, is that the actual speed term is always multiplying the acceleration term as showed in equations 4.14 and 4.15. Hence, for small speeds the dynamic term is always negligible, likely generating an undesirable system response. This modification was also considered for the LabView control algorithm code implemented for the tests. Figure 5.9 shows the new implementation.

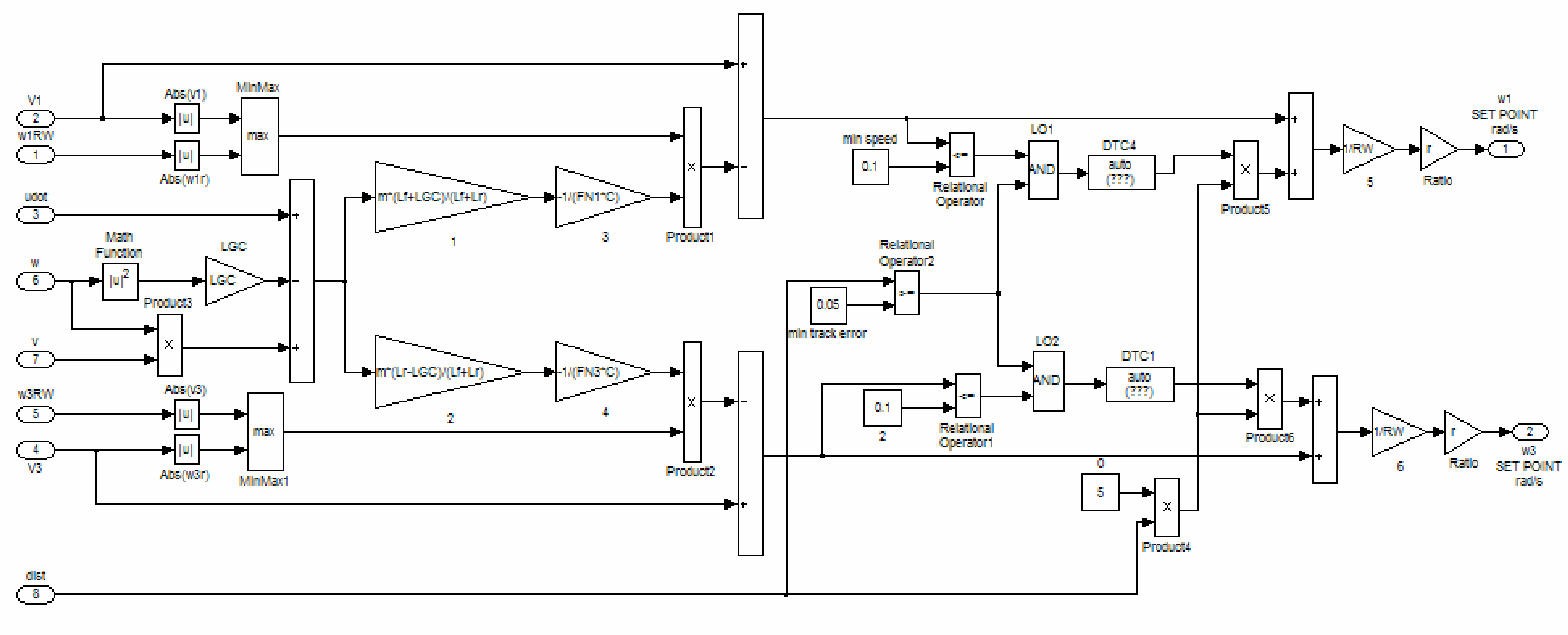

Figure 5.9 New inverse dynamic algorithm

Chapter 6. System implementation

This chapter describes tracking fluoroscope system components. First section presents the general overview of the hardware, software, and a hardware diagram of the control architecture. Subsequently, each component is described. Section 6.3 contains the system control and power wiring diagrams, and deals with the signal conditioning for the encoder and potentiometer. Finally, last section presents the system control software developed in LabView.

6.1 SYSTEM ARCHITECTURE

The tracking fluoroscope control system is a complex mechanism with 2 wheeled-servomotor for driving and 2 servomotors for steering. Every servomotor has a driver or amplifier that supplies it with the necessary power. Such power is obtained from eight twelve volts batteries connected in series of two such that they generate twenty-four volts. That is, four batteries banks connected in parallel; where each battery bank consist on two batteries connected in series, as Figure 6.1 and 6.2 show.

Drivers are controlled by an eight-axis motion card, which is installed in the main computer that is placed in the platform. To control the drivers the main computer has five main feedback signals, as listed subsequently in table 6.1. Figure 6.3 shows the control system architecture including power and control signals.

Control algorithms were developed in LabView. Code is actually running under a Windows XP platform, but it is expected to run under real time once all code is finished. Main system control tasks run in the National Instruments PXI computer, host PC.

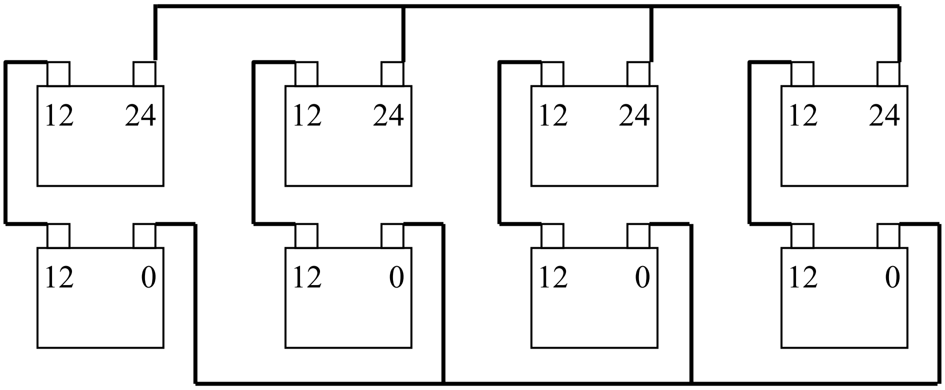

Figure 6.1 Battery Pack configuration

Figure 6.2 Actual batteries connection

Table 6.1 Feedback signals

Device	Measures	Type of signal
Encoder Left Rear Wheel (LRW) driving	Wheel position and speed	Two wires with high frequency pulses.
Potentiometer LRW steering	Wheel steering angle	Analog
Encoder Front Right Wheel (FRW) driving	Wheel position and speed	Two wires with high frequency pulses.
Potentiometer FRW steering	Wheel steering angle	Analog
Laser distance sensor	Subject-Platform distance	RS232

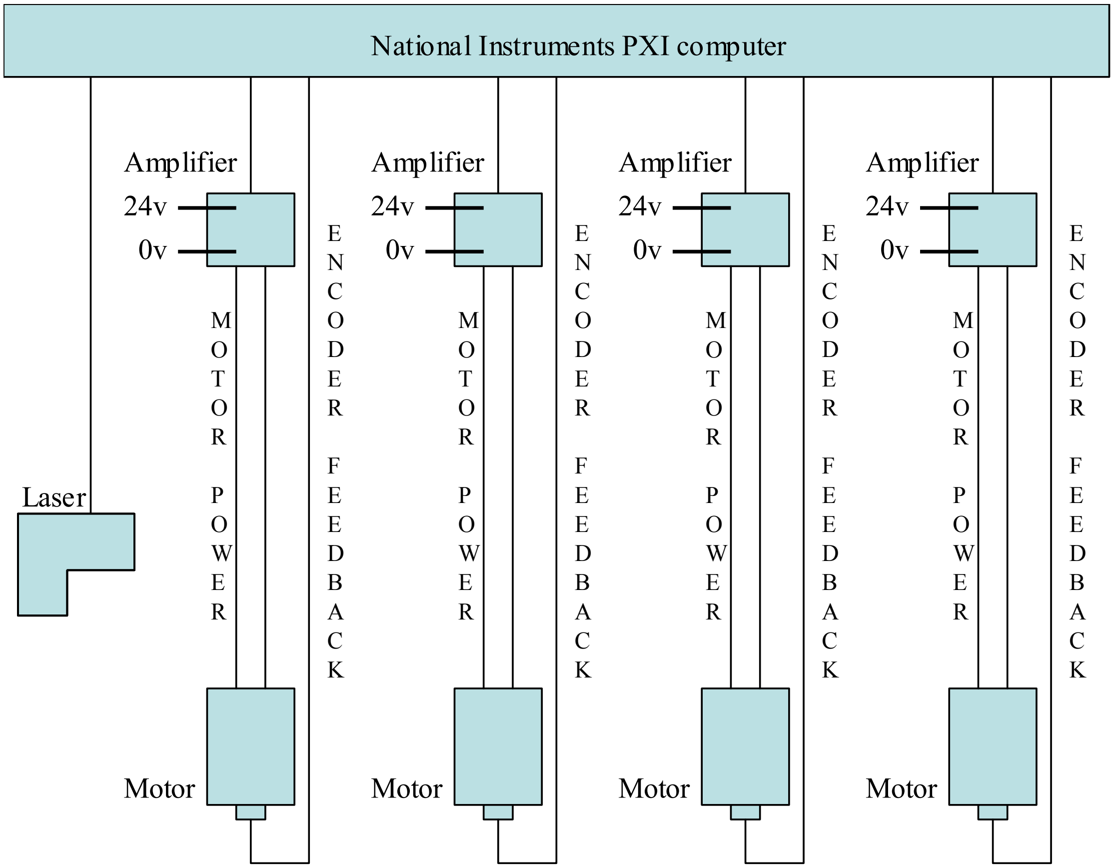

Figure 6.3 Hardware architecture

The subject machine interface HMI, which actually also run in the PXI computer, is controlled from the Dell computer, remote PC. Once the PXI computer goes to real time, the HMI will have to be readapted to run only in the remote computer. A wireless link is established to maintain the remote PC updated. From the remote PC the operator is able to start and stop the system. Operator can also change set points, choose among different operational modes, automatic translational mode, platform rotation, wheel steering and platform manual driving, that are explained later on in the chapter. Figures 6.4 to Figure 6.6 show the host computer, the remote computer and the wireless router respectively.

6.2 SYSTEM DESCRIPTION

6.2.1 Main processing unit

This computer is a National instrument PXI8186 model, with a processor Intel Pentium 4 that runs at 2.2 GHz and with a ram memory of 1 GB. The computer has 8 slots with different PXI cards. The tracking system uses an analog output card, PXI6071E, to operate the driving servomotor brake, and a PXI7538 motion card for the driving and steering functions. The motion card is an eight-axis servo motion controller with quadrature incremental, single ended encoder inputs, +-10v, 16-bit resolution, analog inputs, and +-10v, 16-bit resolution, analog outputs for servo command. The PID update rate range is 62.5 to 500 μs/sample.

The remote computer, showed in Figure 6.5 is a Dell workstation PWS650, Xeon™ with a CPU of 3.06 GHz and 1GB of ram. The wireless link is established by a wireless 4 ports broadband router type g, band of 2.4 GHz and transfer rate of 54 Mbps. The wireless router is showed in Figure 6.6, and it is a Linksys brand, Model wrt54G.

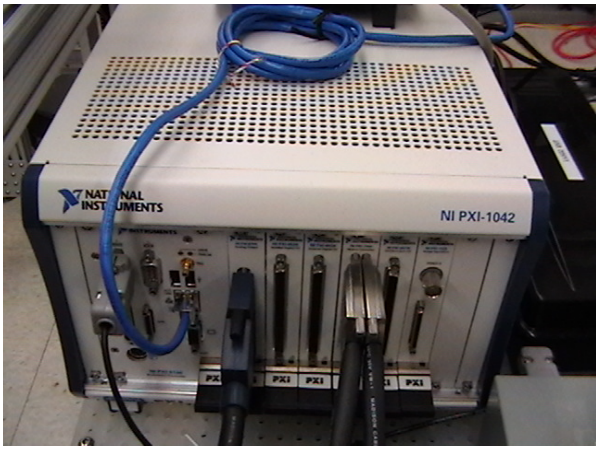

Figure 6.4 National Instrument processor, host computer

Figure 6.5 Dell, remote computer

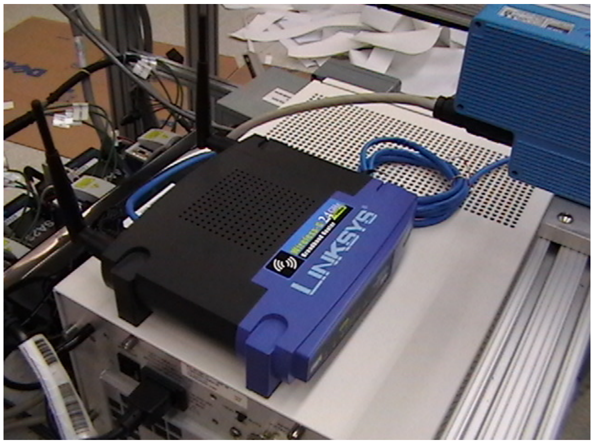

Figure 6.6 Wireless router

6.2.2 Driving-steering servomotors units

Driving-steering servomotor unit is the composition of a DC driving servomotor-in-wheel plus a DC steering servomotor. When the steering servomotor runs, the driving servomotor rotates along the axis perpendicular to the ground. To measure that rotation angle, steering angle, the system has a potentiometer. On the other hand, to measure the position and speed of the driving servomotor, system uses an encoder. Figure 6.7 shows system components, but not showed in the pictures is an internal gearbox that connects the servomotor axis to the wheel axis, with a gear ratio of 9.9. In the case of the external gearbox, the ratio is not needed for position calculation since the potentiometer moves respect to the outer gear instead of the servomotor gear. The potentiometer is 10 KΩ, and the encoder is a Baumer electric quadrature incremental encoder model BHF16.24K with 1000 pulses per revolution. It also has a fifth wire that gives one pulse per revolution. Finally, table 6.2 shows the servomotor parameters as given by the manufacturer.

Table 6.2 Servomotor data

Driving servomotor	
Resistance (Ω)	0.14
Inductance (Ω /s)	0.0005
Torque constant (N.m/A)	0.06
Electro-motive constant (V.s/rad)	0.074
Gear Ratio	9.9
Wheel radius (m)	0.075
Motor and wheel inertia (seen by motor) Kg.m^2	2.15E-4
Steering servomotor	
Steering speed (deg/s)	90

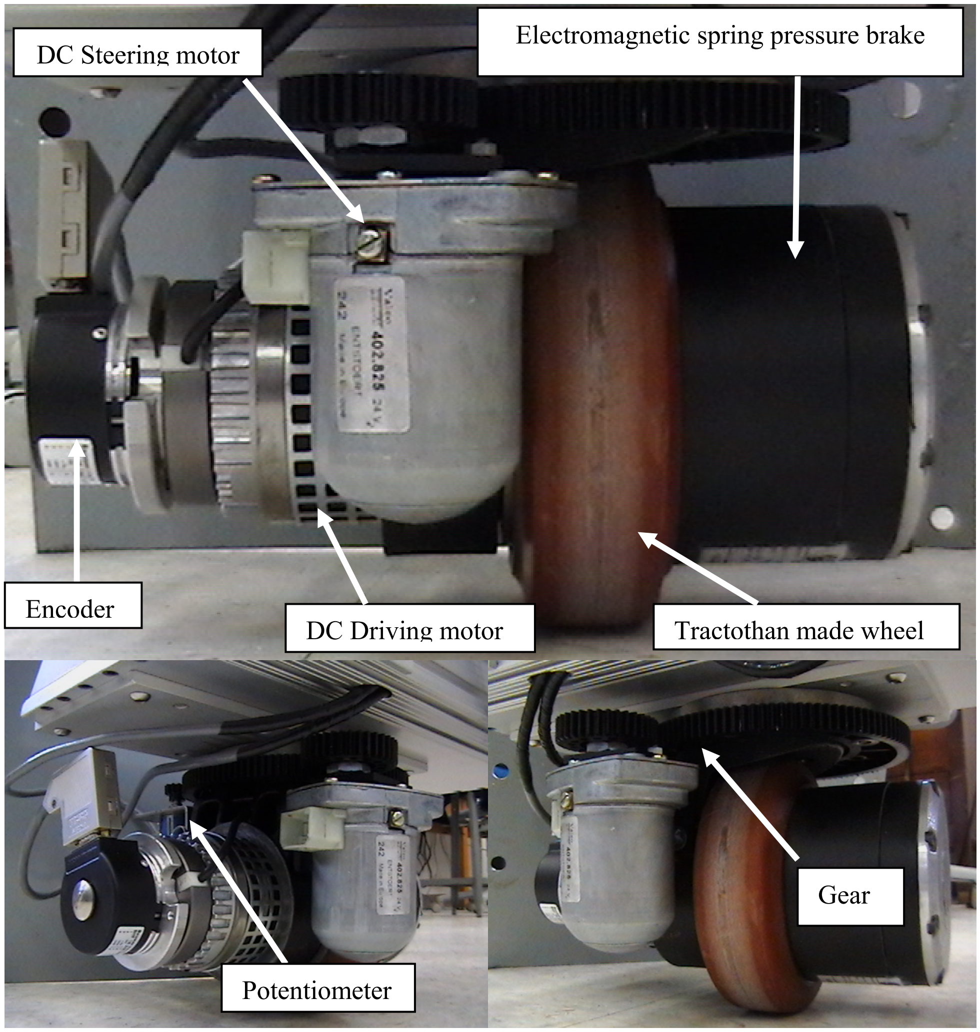

Figure 6.7 Driving-Steering servomotor units

6.2.3 Servomotor amplifiers

The FSA23 Danaher Motion servo amplifiers used in the system operate by the chopper principle for precision control of DC motors. They can be either used with tachometer feedback as well as armature feedback. However, they don't allow encoder feedback and that is the reason to close the speed loop at the motion controller card instead of at the servo amplifier. Table 6.3 resumes the operational data of the driver:

The servo drives are of the four-quadrant control kind, and can therefore precisely control both acceleration and deceleration in both directions. Its typical efficiency exceeds 90%. It has short circuit protection and power transistor overload protection. Figure 6.9 shows the drivers already mounted and wired in the platform.

Table 6.3 Servo amplifier operational data

Type	FSA23
Supply voltage (24v/48v systems)	15-70 v
Power consumption	1.2 W
Control voltage range	+- 10 v
Chopper frequency	21 KHz
Voltage drop in FSA	0.12
High current limit (adjustable)	23 A / 3s
Low current limit (adjustable)	10 A
Continuous current	10 A at 40^{o}c
Minimum motor inductance	100 μH
Trigger temperature for over heating protection	70^{o}c
Weight	0.7 Kg

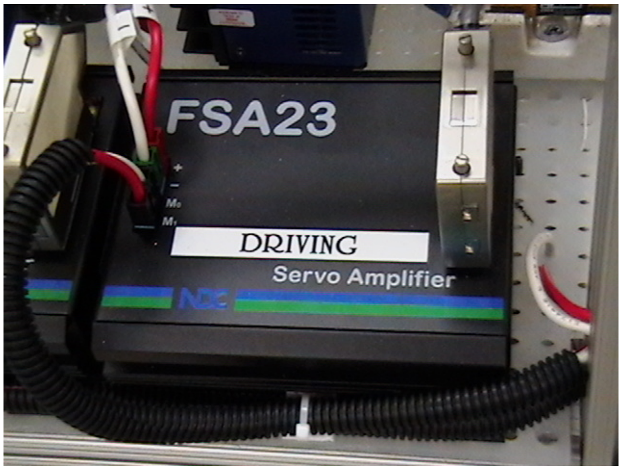

Figure 6.9 Servo amplifiers

6.2.4 Laser distance sensor

The laser distance sensor is a Sick model DME 3000-2. It has 1 mm resolution, selectable response time from 20 to 200 ms. It transmits data trough a RS422 channel at a transfer rate of 38.4 Kbps maximum. The system has a RS422/RS232 converter that sends data to the computer communications port. That signal is read by a LabView code that configures the computer port. Figure 6.10 shows the laser mounted and table 6.4 gives the laser accuracy.

6.3 POWERING AND CONTROL SIGNALS

6.3.1 Wiring diagrams

Next pages show the wiring diagrams for the tracking fluoroscope system. Power and control electric wiring diagrams are presented. Next section introduces the signal conditioning.

Figure 6.10 Laser distance sensor

Table 6.4 Laser accuracy (from manufacturers manual)

Accuracy (for measuring distance)	1 m	2 m	4 m	6 m	8 m
White 90 %	± 5 mm	± 5 mm	± 10 mm	± 20 mm	± 30 mm
Grey 18 %	± 5 mm	± 10 mm	± 30 mm		
Black 6 %	± 10 mm	± 20 mm			

Figure 6.11 shows the laser RS422/RS232 converter power connections and the encoder power and signal connections. The encoder signals had to be transformed, as it will be explained in next section, to do that a voltage divider was made. Last Figure also shows the encoder motion card digital grounding and encoders fuse. Figure 6.12 illustrates the potentiometer input signal and the analog output connections to command the servo drives.

Finally, next diagram includes all power wirings. Figure 6.13 includes two steering, and two driving servomotors with its electromagnetic brakes, remote switch for emergency stop, fuse circuit protection, screw terminals, relays, diodes and batteries.

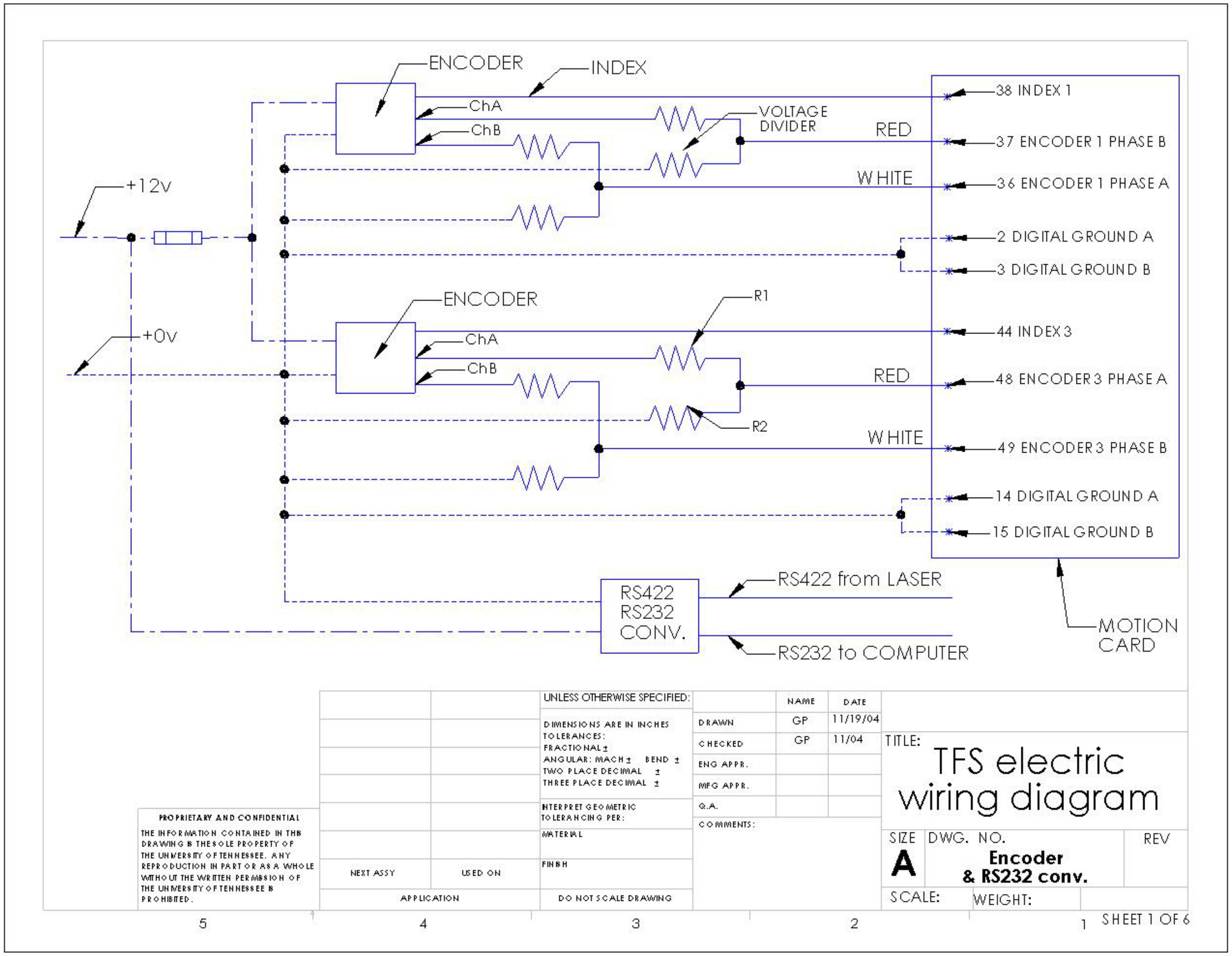

Figure 6.11 Encoder and laser converter connections

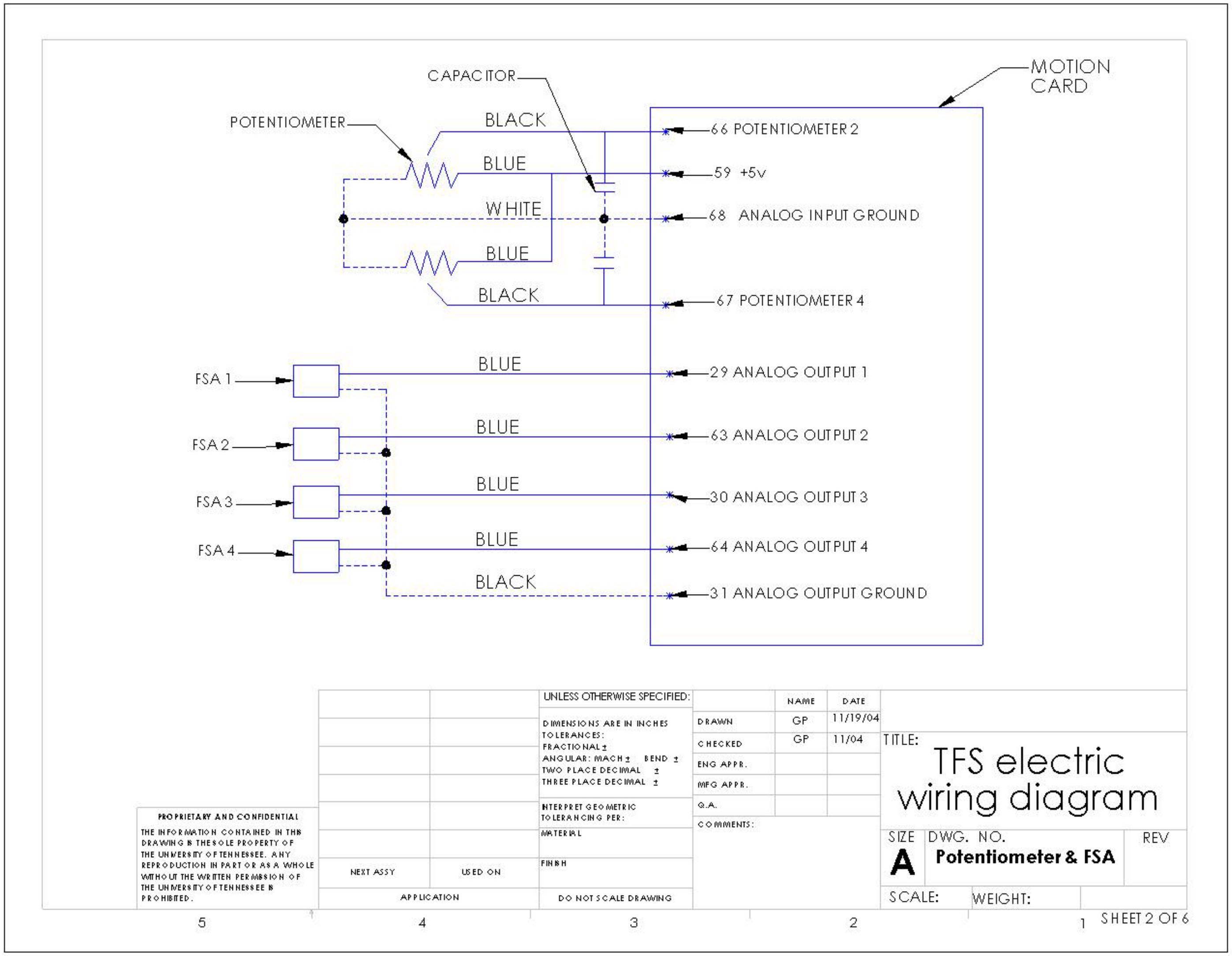

Figure 6.12 Wiring of potentiometer and signal to amplifiers

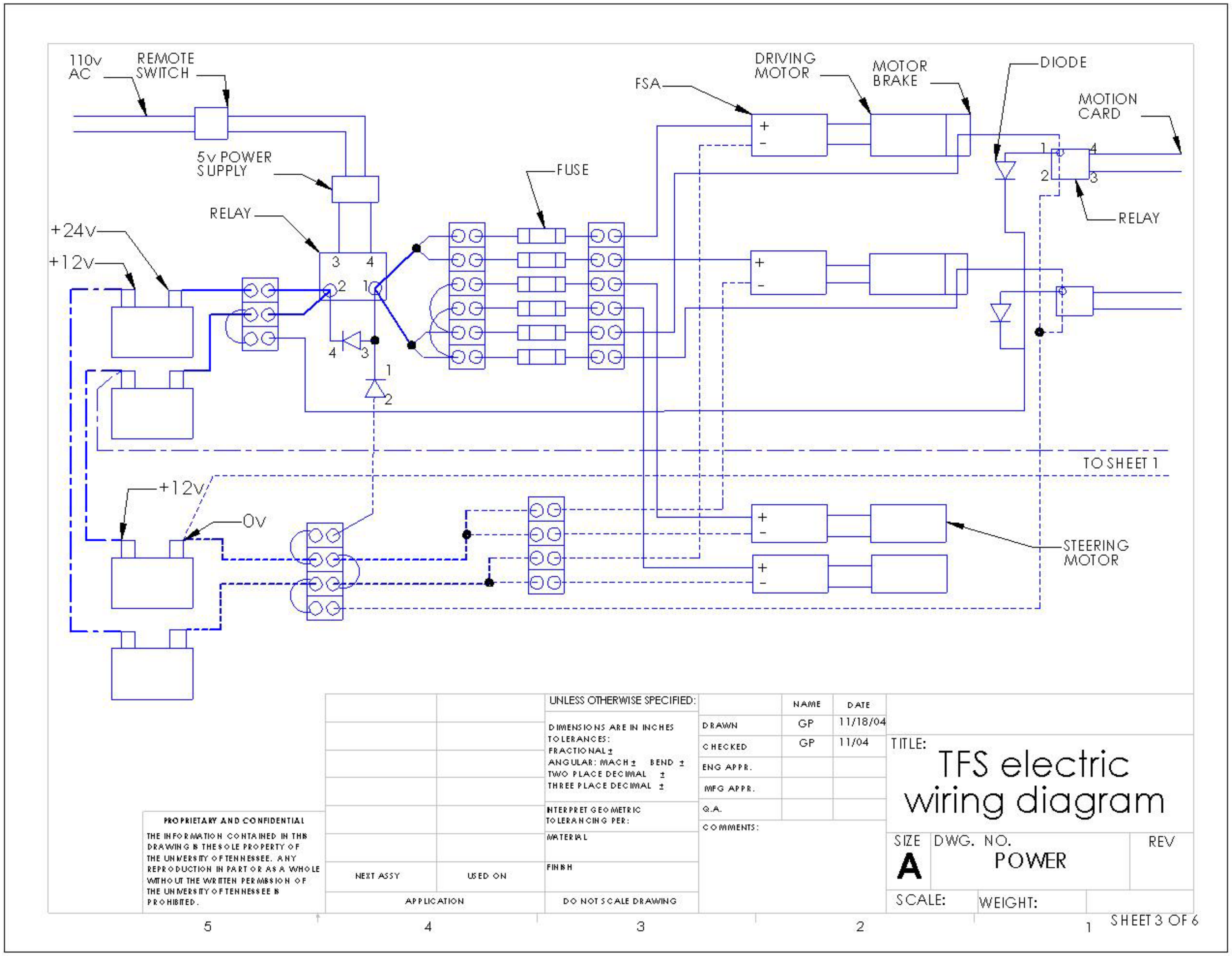

Figure 6.13 Power connections

6.3.2 Signal conditioning

The tracking fluoroscope system is a complex electric system with different voltages. The system has 5v, 12v, 24v DC and 115v AC. Furthermore, it has 8 servo amplifiers which work sending high frequencies to the motors. Besides the DC servomotors also create a magnetic field in its surroundings. All those factors contribute to noise interference at the control signal level. Thus, the system has to be properly wired and grounded. For the wiring, special caution was taken to have control and power lines as separated as possible. In addition, control and power lines were crossed at 90 degrees at lines intersections to avoid noise due to the magnetic field created by the power wires.

Even the precautions taken, noise was found at the potentiometer signal. Large peaks appeared generating the control algorithm of the steering motor to operate when the motor was correctly positioned. Hence, a capacitor of 105 mF was placed to reduce the noise. The potentiometer is power with 5v from the motion card. The capacitor was placed between the motion card analog ground and the potentiometer signal wire.

The baumer electric encoder needs a minimum power supply of 10v and a maximum of 30v. The output channels of the encoder, A and B, have a voltage that is 2v less than the encoder input voltage. The motion card encoder input is 0-5v. Then, it is easy to see that even powering the encoder with the minimum of 10v, its output A/B would be 8v, what is greater than the maximum voltage at the motion card encoder input, 5v. Consequently, a voltage divider is placed at the encoder output to reduce the voltage to less than 5 volts.

The motion card encoder input has a pull up resistor of 3.3 KΩ value. The motion card considers a low state of the encoder when A/B channel the voltage is less than 0.8v, and considers a high state when voltage is higher than 2v. Figure 6.14 shows the voltage divider configuration to accomplish the motion card requirements.

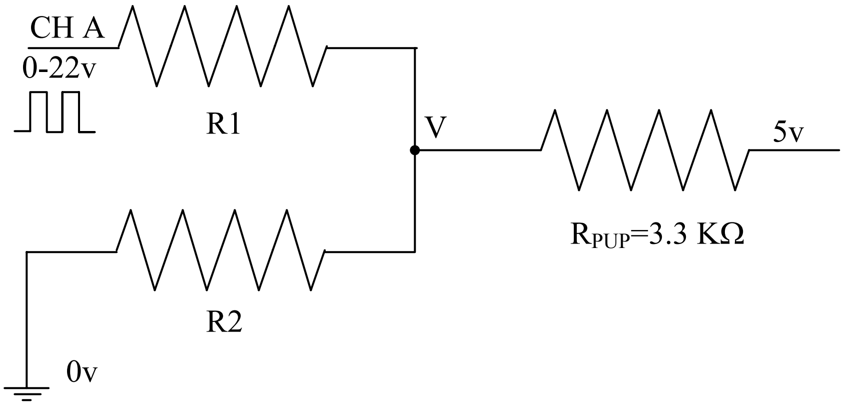

Figure 6.14 Encoder voltage divider

In the case of a peak the voltage at channel A is 22v, then for a high voltage with the showed resistors configuration the voltage, V, at the input point relates to the other variables by equation 6.1. By Kirchoff law the current flowing in and out of a node is null, then applying it to the motion card input:

$$\frac{22-V}{R1}+\frac{5-V}{R_{PUP}}=\frac{V}{R2} \qquad \text{Eq. 6.1}$$

Operating, the value of V can be found in function of the resistors R1 and R2.

$$V_{HIGH}=\frac{R2*(5*R1+22*R_{PUP})}{R1*R2+R1*R_{PUP}+R2*R_{PUP}} \qquad \text{Eq. 6.2}$$

In the case of a valley the voltage at channel A is 0v, then for low voltage with the showed resistors configuration the voltage, V, at the input point relates to the other variables as follows:

$$\frac{-V}{R1}+\frac{5-V}{R_{PUP}}=\frac{V}{R2} \qquad \text{Eq. 6.3}$$

Table 6.5 Resistors for voltage divider

R1	R2	Vlow	Vhigh
2.00	0.70	0.68	5.61
2.00	1.00	0.84	6.94
2.00	0.50	0.54	4.46
5.00	1.00	1.01	3.94
1.00	1.00	0.66	10.21
1.00	2.00	0.84	13.04
1.00	3.00	0.93	14.37
1.00	0.50	0.46	7.12
1.00	0.20	0.24	3.73
2.00	0.20	0.26	2.16
0.60	0.19	0.21	4.97

Operating, the value of V can be found in function of the resistors R1 and R2.

$$V_{LOW} = \frac{5}{\left(1 + R_{PUP} * \left(\frac{R1 + R2}{R1 * R2}\right)\right)} \qquad \text{Eq. 6.4}$$

Table 6.5 was built varying R1 and R2. In this case, the values of R1 and R2 chosen were:

R1= 600 Ω

R2= 200 Ω

6.4 LABVIEW CODE

Next pages present the software code developed in LabView. Four codes were developed, platform setup code, dynamic code, kinematic closed loop, and kinematic open loop. Those codes may be integrated in a common single program in the case the platform desires to be controlled by the different tracking control algorithms.

6.4.1 Platform setup software code

The platform setup algorithm is designed to rotate platform 90 degrees respect to its original position. The program does a platform rotation in two steps. The first step is to steer the wheels, the second one is to run the driving wheels. Figure 6.15 is the operator screen, or human machine interface, from where the operator controls the system. Please refer to that figure for the next description.

The first step is to steer the wheels, steering can be operated manually or automatically. The main steering button, placed next to the emergency stop button, turns on the steering algorithm. If PID button is off, manual voltage can be applied to the motion card output. If the PID button is on, then a PID controls the steering angle for correct positioning. Using the selector placed under the PID button, steering angle can be set manually to each wheel, or automatically to both wheels steering them to 0 or –47.5 degrees. To rotate the platform 90 degrees wheels must be steered –47.5 degrees as defined in previous chapters. Steering angle is always showed to the operator by the charts.

The second step is to run the driving motors. The main driving button, placed in the left bottom side of the picture, turns on the driving algorithm. The operator should select “automatic speed”, release the brake, and then write the platform rotation angle. If the operator wants to do it manually, he/she needs to select manual voltage. Operator should choose between translation and rotation modes. In the translation mode, the wheels go in the same direction and then the platform translates, while in the rotation mode they go in opposite direction. The operator should later release the brake and change the voltage as desired, using the colored gauge in the bottom of the screen.

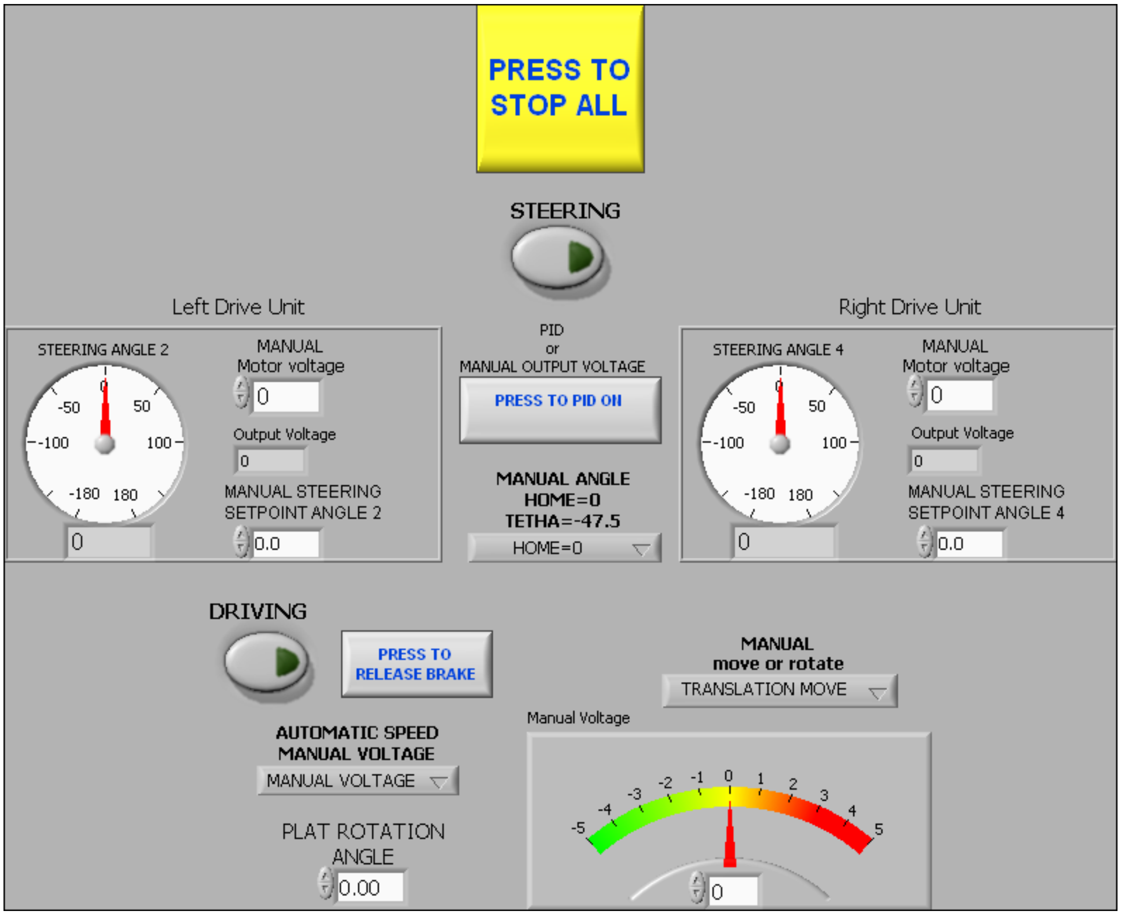

STEERING ANGLE 2: 0
MANUAL Motor voltage: 0
Output Voltage: 0
MANUAL STEERING SETPOINT ANGLE 2: 0.0
MANUAL ANGLE HOME=0 TETHA=-47.5: HOME=0
STEERING ANGLE 4: 0
MANUAL Motor voltage: 0
Output Voltage: 0
MANUAL STEERING SETPOINT ANGLE 4: 0.0
MANUAL move or rotate: TRANSLATION MOVE
AUTOMATIC SPEED MANUAL VOLTAGE: MANUAL VOLTAGE
PLAT ROTATION ANGLE: 0.00
Manual Voltage: 0

Figure 6.15 Platform rotation HMI screen

Figure 6.16 shows the LabView code for the platform rotation. Since most steering and driving code developed here is used later in the other codes, they are only explained here.

The code has a main while loop, which runs every 30 ms.. It contains all the code on it, except for the initialization of the motion controller and the resetting of the motion card output. The sequence structure, at the right side of the figure, is the one which resets the output when the while structure is stopped with the emergency stop bottom. Two main case structures selectable with the buttons showed in Figure 6.16 are used; one is used for steering and the other one for driving. Figure 6.16 shows the two case structures in the ON state. When they are in OFF state, the code loads 0 volt to the motion card outputs that go to the motor amplifiers. In a similar way, in the case structure to choose between manual voltage steering or automatic PID steering, only the second one is showed in Figure 6.16. Figure 6.17 shows that case structure in the "Manual voltage" steering case. Once again, in the case structure to select among manual angle, 0 deg, and –47.5 deg, only the last one is showed in Figure 6.16. Figure 6.18 shows the other two states of the case structure. The last case structure is the one to select between automatic rotation and manual output voltage, only the automatic speed rotation is showed in Figure 6.16. Figure 6.19 shows the case structure for the manual voltage state, including the translational mode and rotational mode selector. Finally, Figure 6.20 is an operation chart that shows all the functions that the operator can do and its operation order.

6.4.2 Dynamic control software code

In this program, the steering code is almost the same as with the one developed for the platform rotation. Since this algorithm is not intended for platform rotation, the code does not include different angle for each wheel and also replace the –47.5 deg steer angle by 90 and –90 deg needed by the lateral translational mode cases. This HMI screen includes both wheels' speed in conjunction with platform speed and is showed

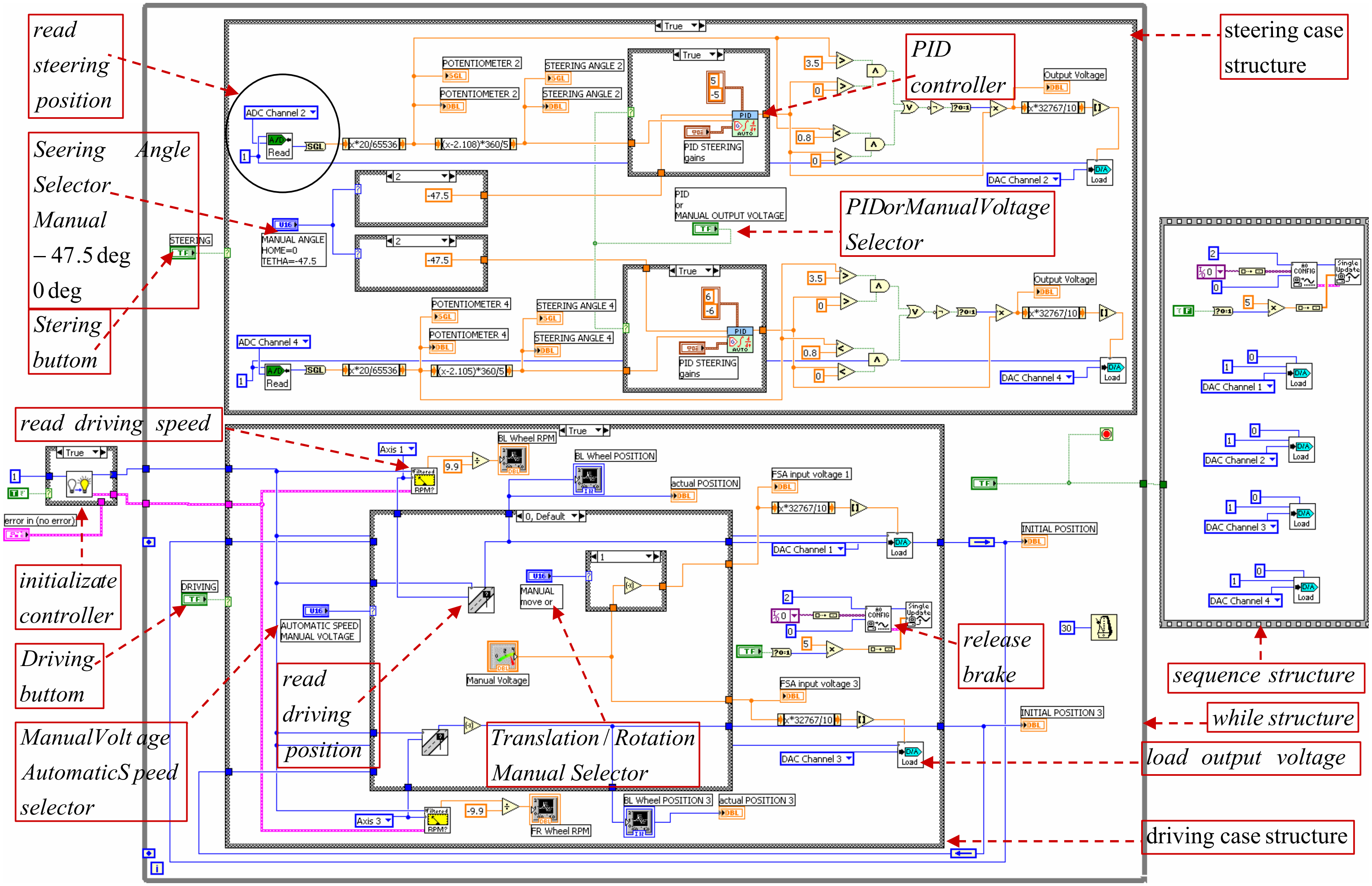

Figure 6.16 Platform rotation LabView code

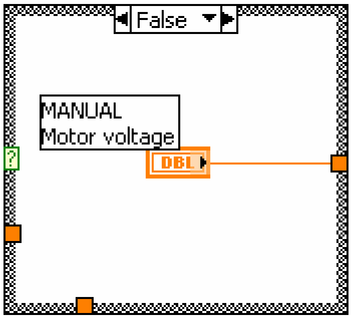

Figure 6.17 Manual voltage to steering servomotor

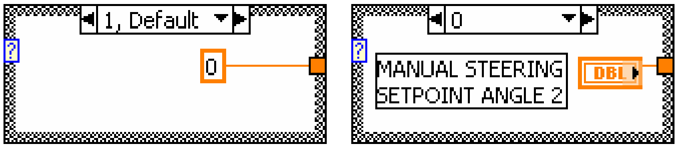

Figure 6.18 PID steering angle set point

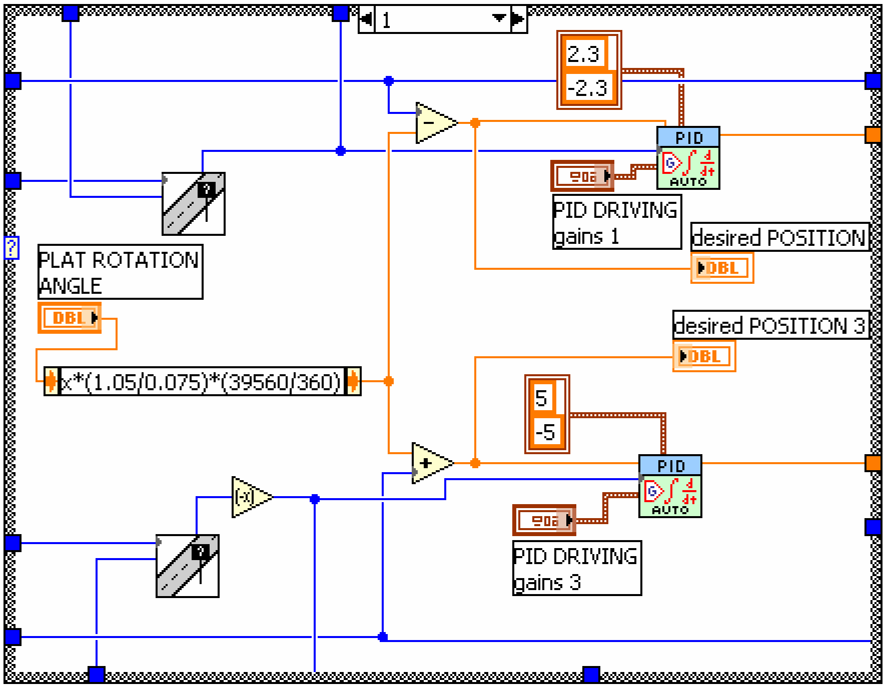

Figure 6.19 Automatic driving for platform rotation or translation

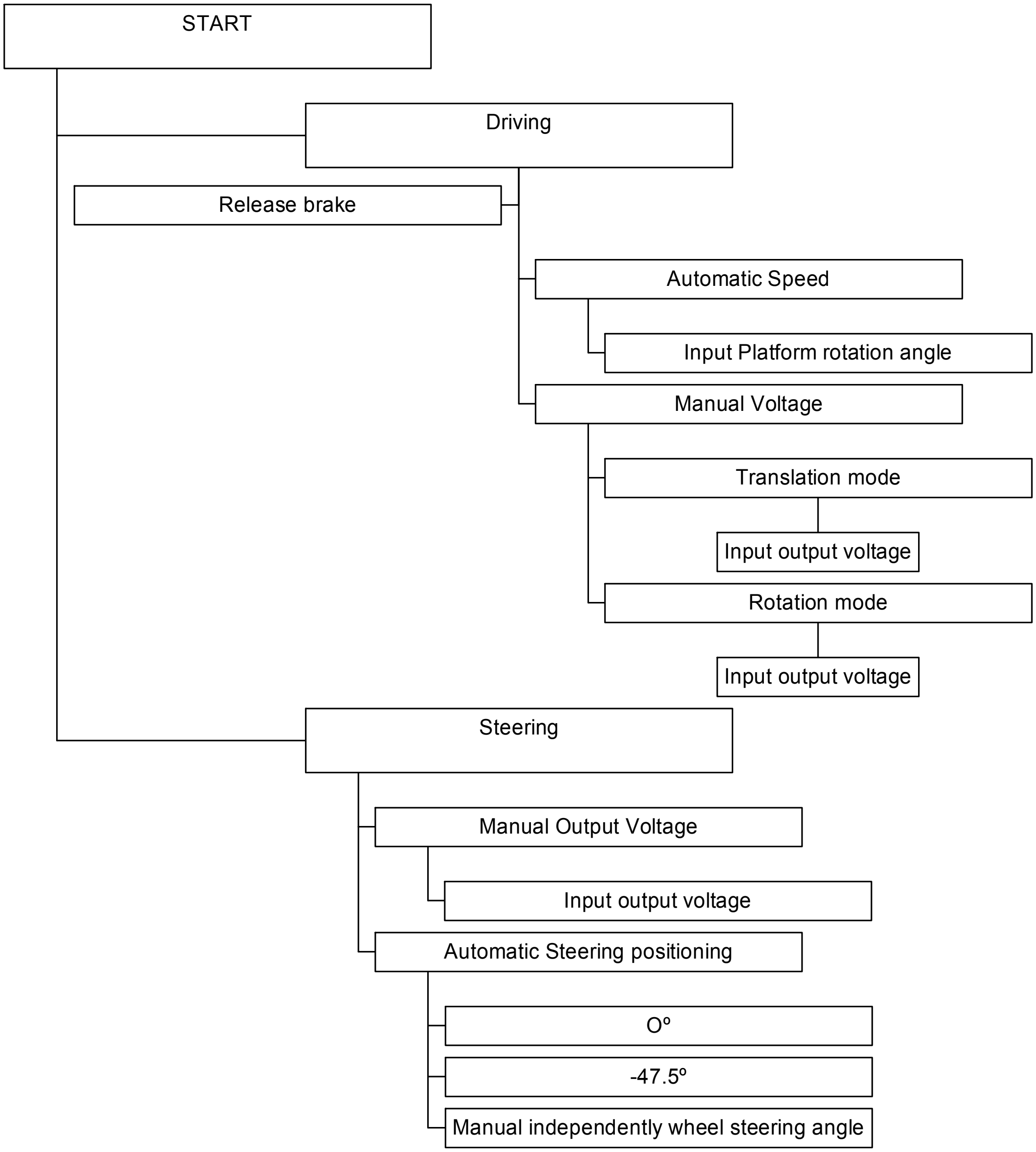

Figure 6.20 Platform rotation operations chart

in Figure 6.21. Besides, it adds the distance set point input, distance tracking error plot and subject position graphic. Figures 6.22, 6.23 and 6.24 show LabView code for the dynamic model. Figure 6.25 illustrate operations chart to easily understand operator tasks availability.

In the case structure to select among manual speed, automatic speed or manual voltage, only the automatic speed is showed in the Figure 6.21. Figure 6.22 and 6.23 show the other two cases. The automatic speed case structure contains the equations developed in previous chapters to calculate wheel 1 and wheel 3 speeds in function of their actual speed and desired acceleration. The algorithm also contains the adaptive control algorithm explained in the control chapter that adds a kinematic term when the platform and wheel speed terms are small.

6.4.3 Kinematic control software code

In this case the steering code is exactly the same as for the dynamic model. The only difference with the dynamic model is that for the automatic speed, the speed set point is set to the output of the distance PID controller. However, in the dynamic code, the inverse dynamics algorithm calculates the desired speed in function of the desired acceleration that is the distance PID controller.

Figure 6.26 shows the operator screen, or human machine interface. Figure 6.27 and Figure 6.28 are equal but they are written with different LabView functions. When using the motion card functions, there is no need to use a PID controller to control the motor speed. That controller is built-in at the motion card function. As it can be seen, the motion card code seems to be easier and neater than the other; besides acceleration and speed margins can be established. However, it has some disadvantages. The first one is that the PID gains have to be defined in the motion card configuration software, outside of LabView, and then with a difference interface that can only be programmed at the host computer. That software does not tolerate tuning the internal PID controller

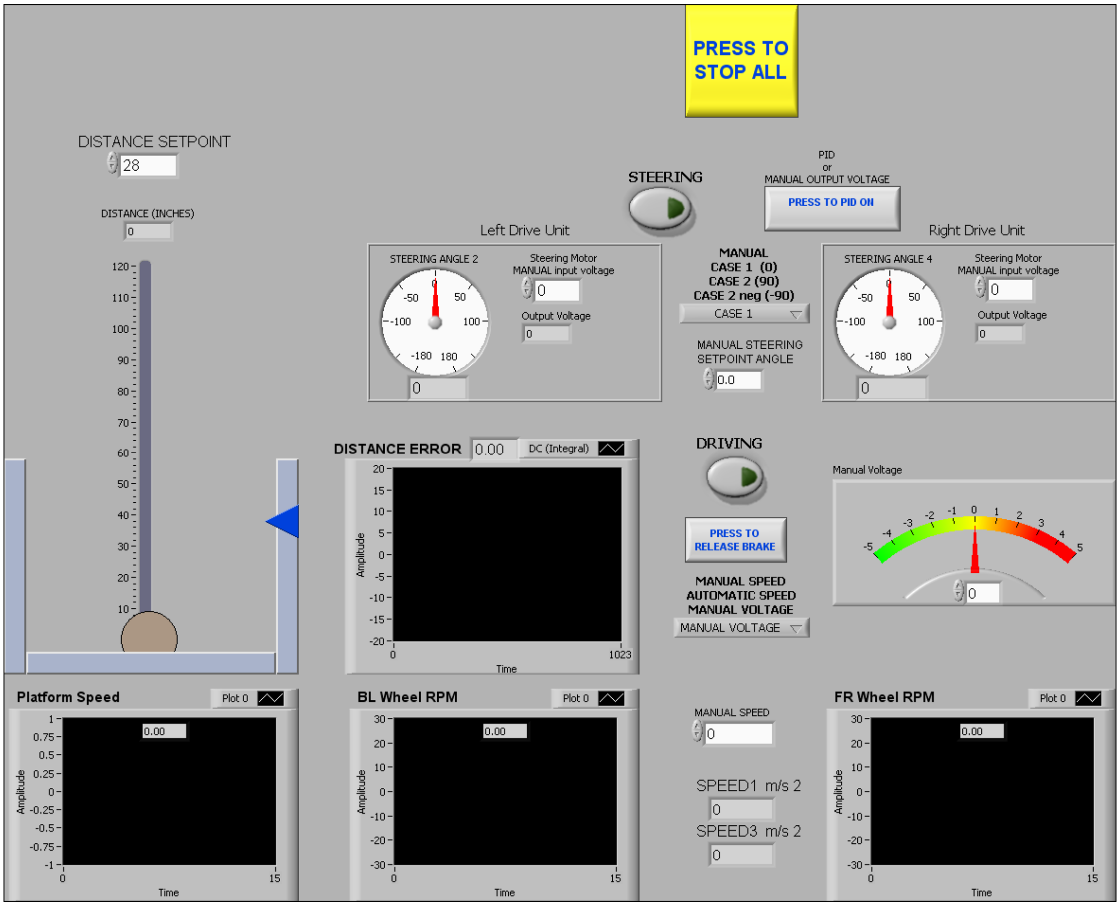

DISTANCE SETPOINT 28

DISTANCE (INCHES) 0

DISTANCE ERROR 0.00

Steering Motor MANUAL input voltage 0

Output Voltage 0

CASE 1

MANUAL STEERING SETPOINT ANGLE 0.0

MANUAL VOLTAGE

MANUAL SPEED 0

SPEED1 m/s 2 0

SPEED3 m/s 2 0

Figure 6.21 Platform dynamic control HMI screen

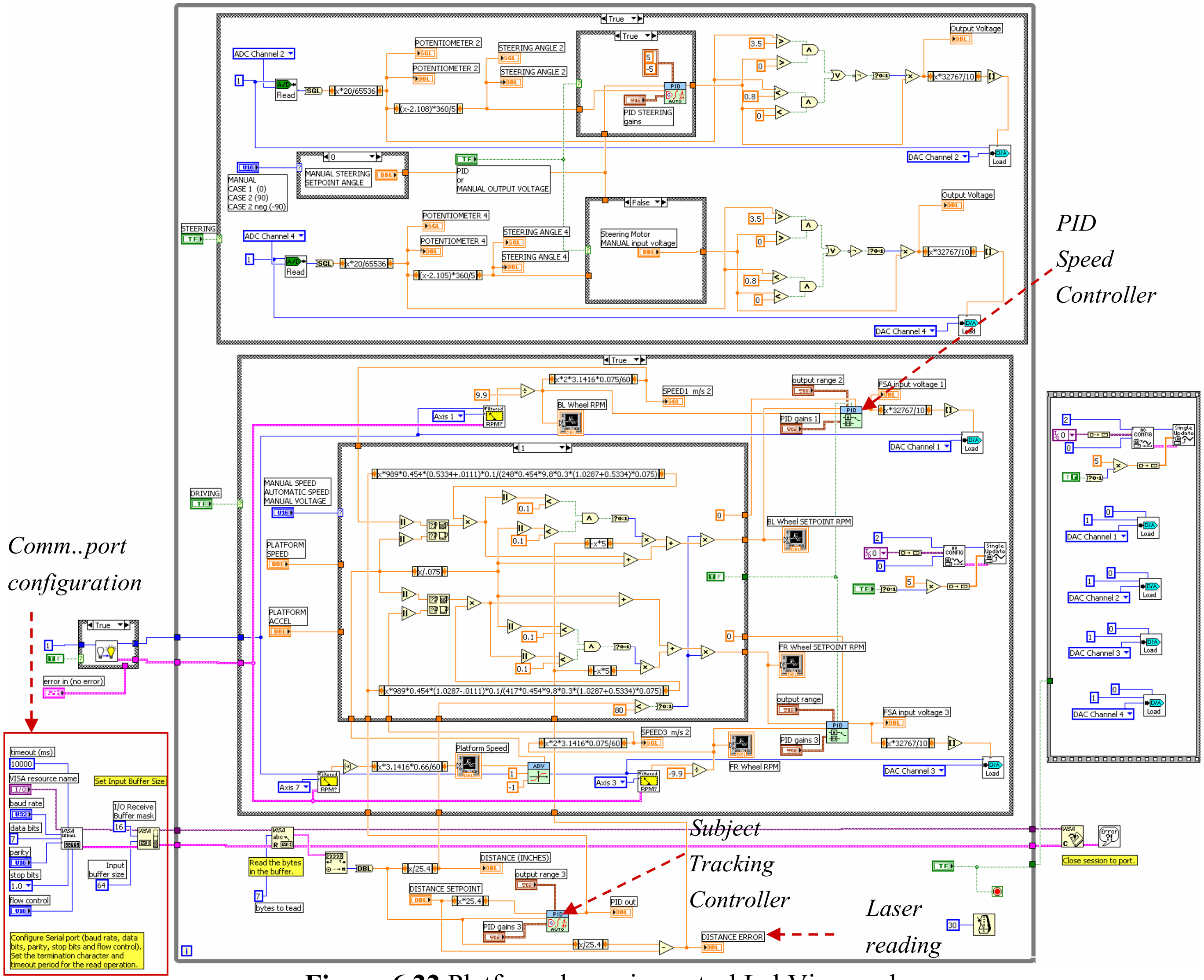

Configure Serial port (baud rate, data bits, parity, stop bits and flow control). Set the termination character and timeout period for the read operation.

Read the bytes in the buffer.

Close session to port.

Figure 6.22 Platform dynamic control LabView code

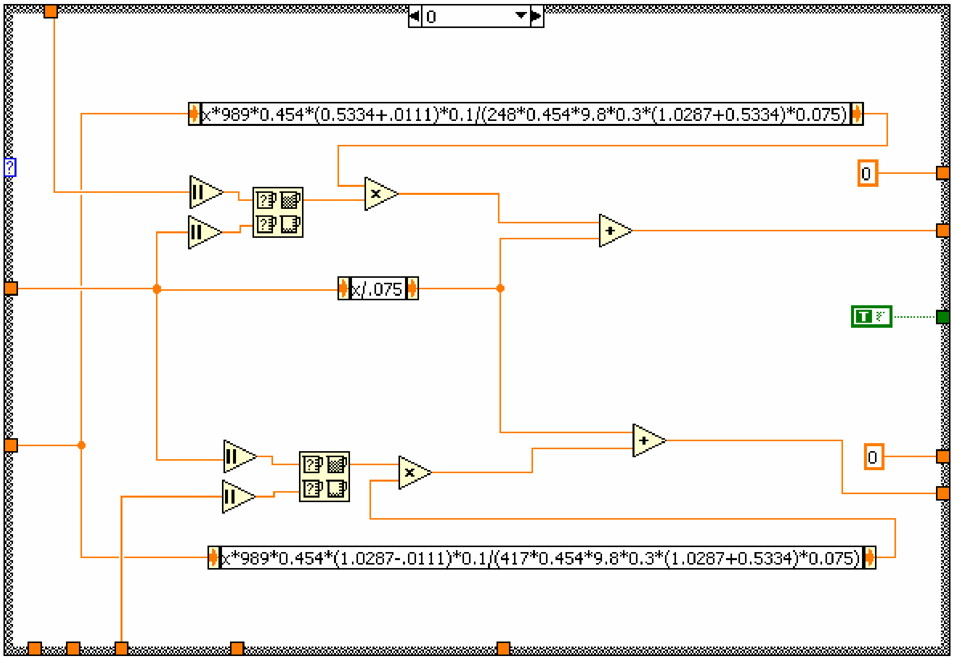

Figure 6.23 Platform dynamic control LabView code, manual speed case

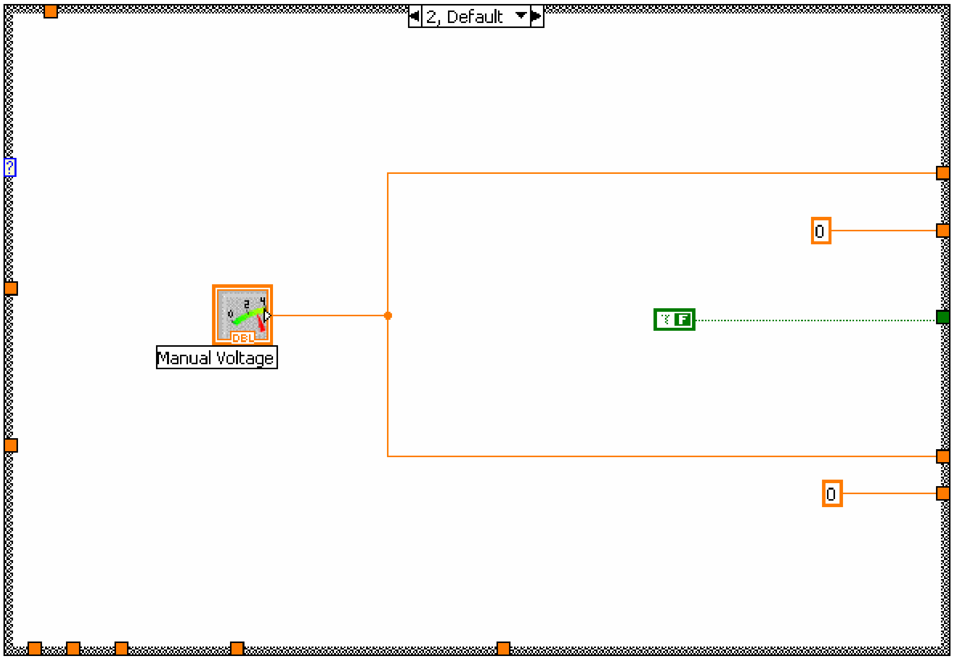

Figure 6.24 Platform dynamic control LabView code, manual voltage

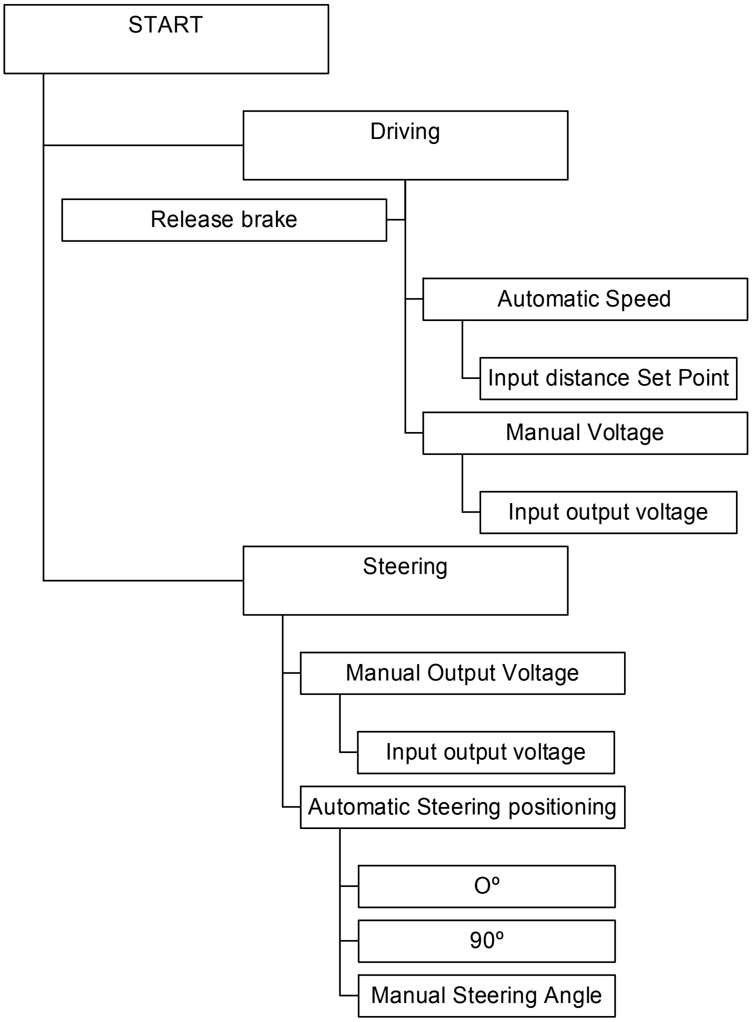

Figure 6.25 Dynamic control operations chart

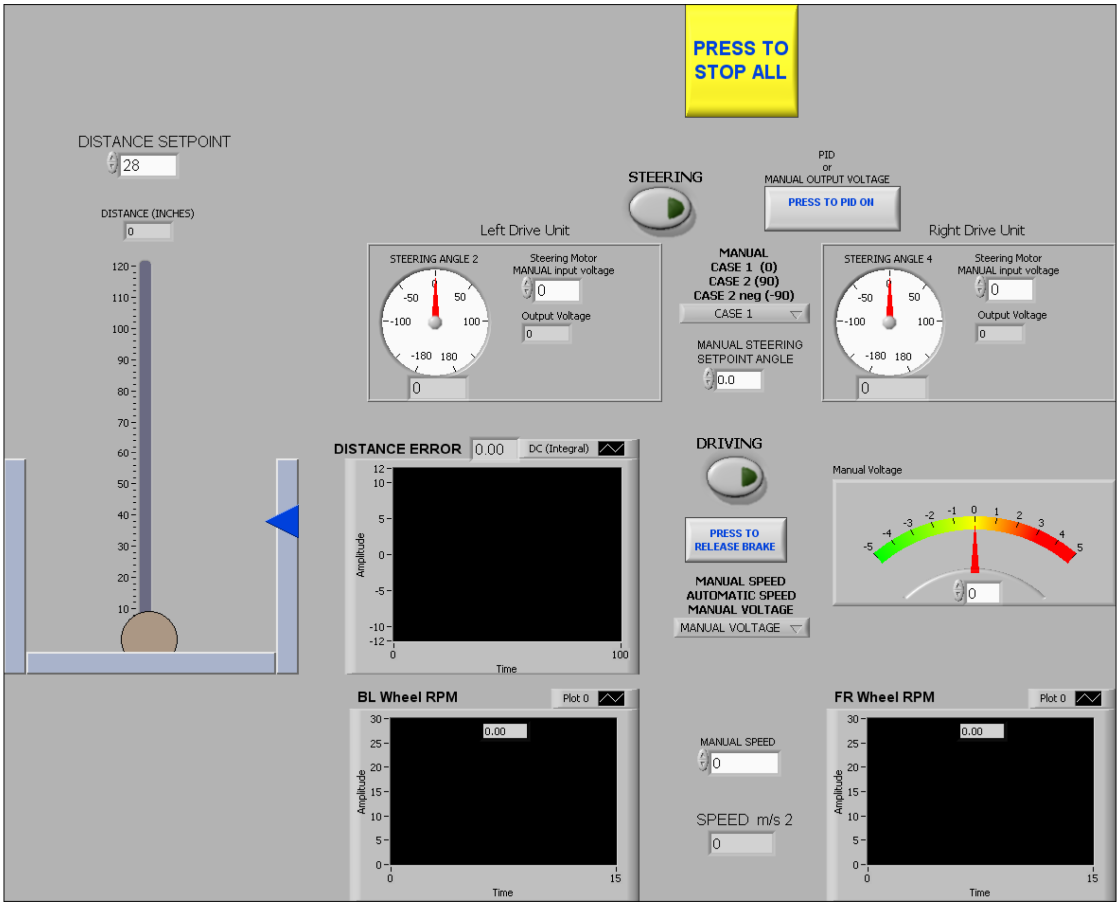

DISTANCE SETPOINT 28

DISTANCE (INCHES) 0

STEERING ANGLE 2: 0

Steering Motor MANUAL input voltage (Left Drive Unit): 0

Output Voltage (Left Drive Unit): 0

MANUAL
CASE 1 (0)
CASE 2 (90)
CASE 2 neg (-90)

CASE 1

MANUAL STEERING SETPOINT ANGLE 0.0

STEERING ANGLE 4: 0

Steering Motor MANUAL input voltage (Right Drive Unit): 0

Output Voltage (Right Drive Unit): 0

DISTANCE ERROR 0.00

MANUAL SPEED
AUTOMATIC SPEED
MANUAL VOLTAGE

MANUAL VOLTAGE

Manual Voltage: 0

MANUAL SPEED 0

SPEED m/s 2: 0

BL Wheel RPM: 0.00

FR Wheel RPM: 0.00

Figure 6.26 Platform kinematic (closed control loop) HMI screen

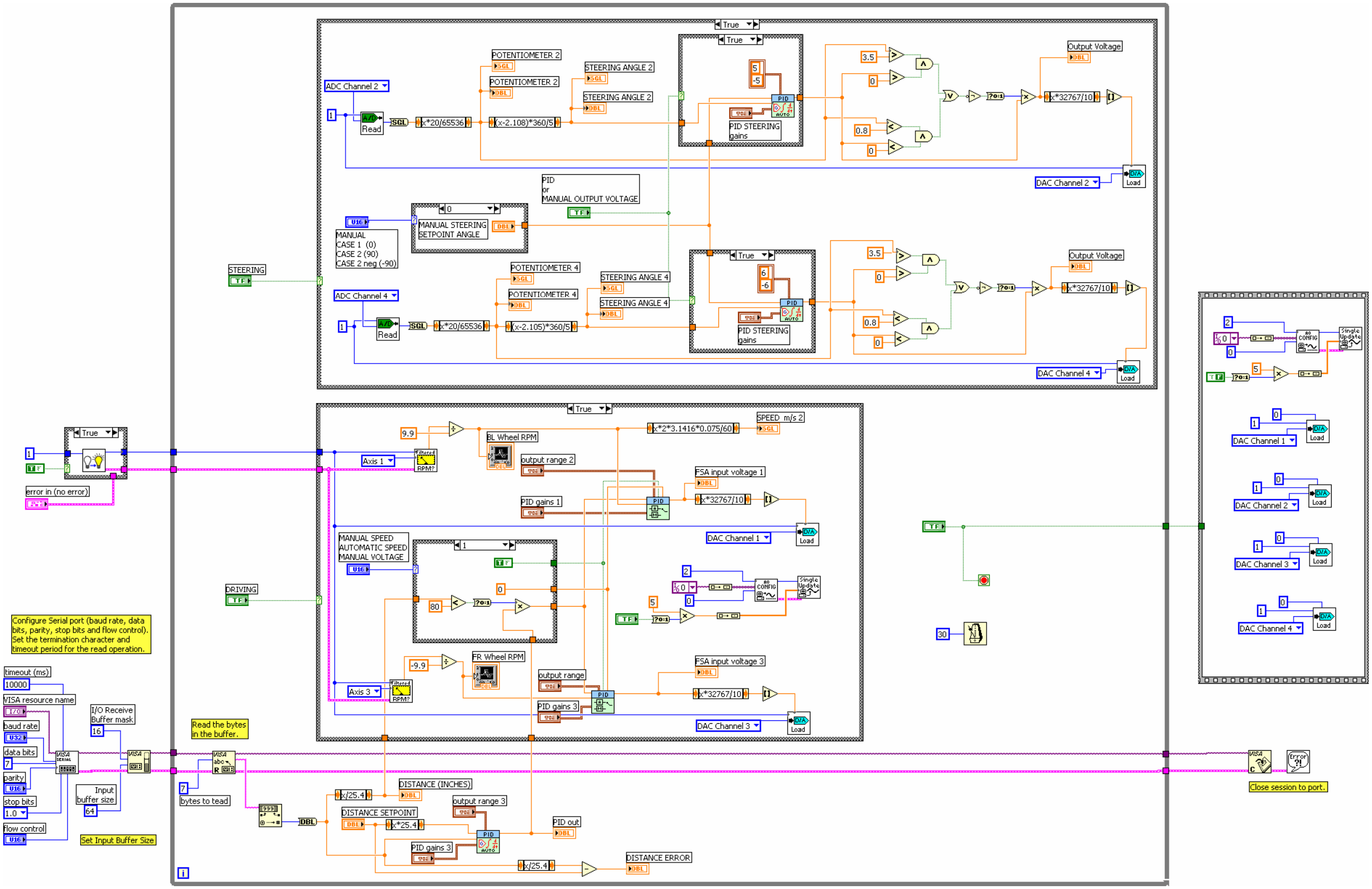

Figure 6.27 Platform kinematic (closed control loop) LabView code

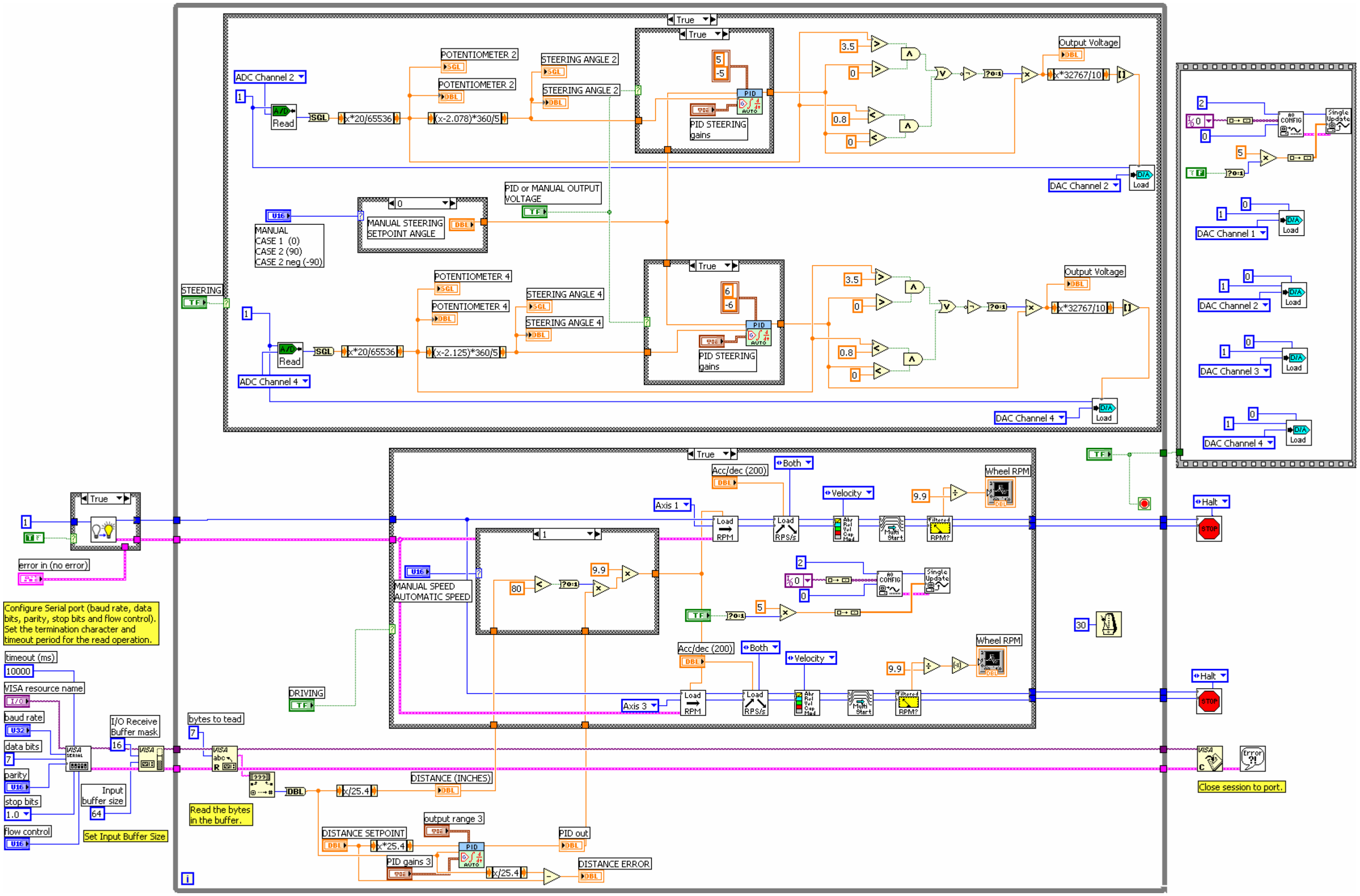

Configure Serial port (baud rate, data bits, parity, stop bits and flow control). Set the termination character and timeout period for the read operation.

Set Input Buffer Size

Read the bytes in the buffer.

Close session to port.

Figure 6.28 Platform kinematic (closed control loop) LabView code using internal motion card functions for the two driving servomotors at the same time. Hence, the tuning process has to be done one motor at a time, and then with the platform lifted. Subsequently, when doing the tuning process, the load at the servomotor is not the real load that the servomotor is going to have when moving the platform. The second disadvantage is that the motion card output voltage cannot be controlled. Thus, if the brake is pressed when the speed set point is not null, the motion card output goes to ±10 v, and then full power is applied to the servomotor with the brake on. Finally, the motion card functions are only designed for encoder inputs, then the steering servomotors can only be controlled using the motion card output as an analog signal, like done by code showed at Figures 6.22 and 6.27. Finally, Figure 6.29 shows the operation chart for the Kinematic closed control loop model.

6.4.4 Stand-off distance controller software code

In this case the steering code is exactly the same than for the dynamic and kinematic closed control loop models. This screen and code are much simpler than the previous models' screen since this model does not need a controller for the speed. The output of the distance controller is the speed set point. Finally, it is worth mentioning that since there is no controller for the speed, the platform cannot be manually moved at a certain speed. In this case, the platform can be moved at a certain motion card output voltage, which has a direct relationship with the speed. Figures 630, 6.31 and 6.32 show the human machine interface, the LabView code, and the operations chart for the stand-off distance controller model.

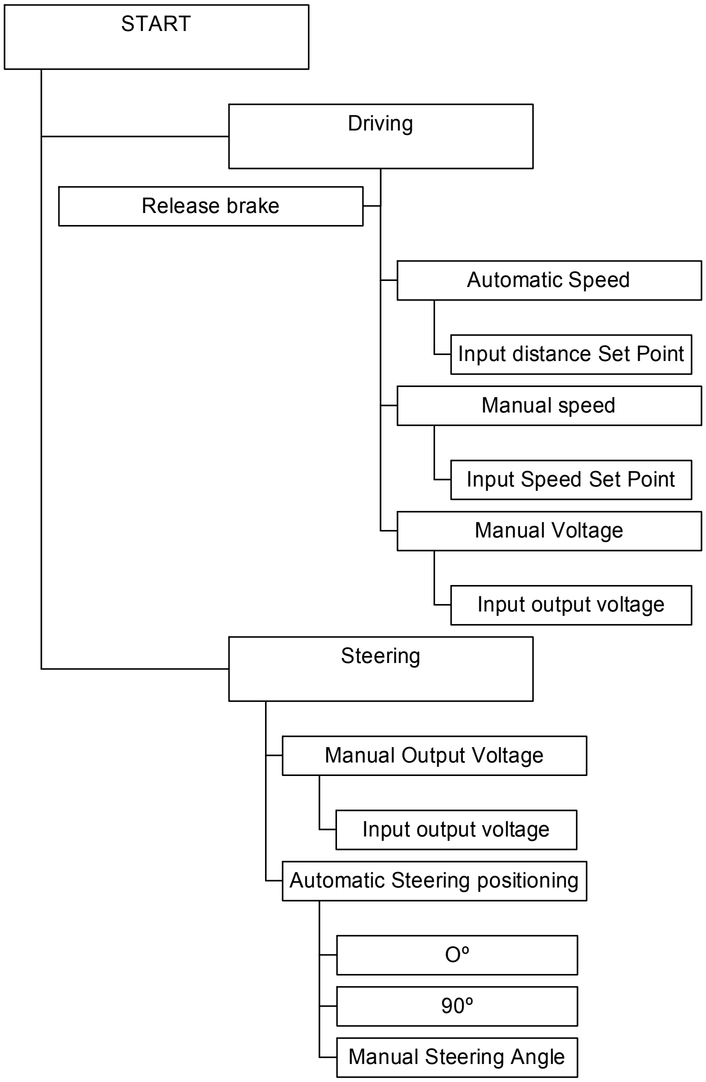

Figure 6.29 Kinematic (closed control loop) operations chart

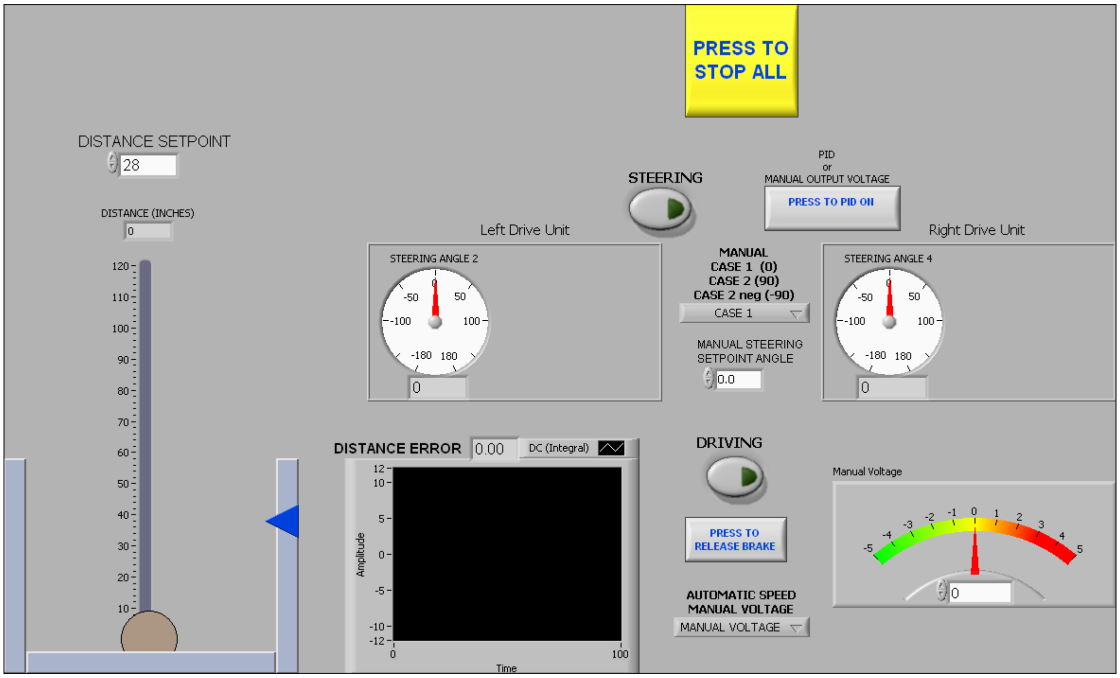

DISTANCE SETPOINT 28

DISTANCE (INCHES) 0

STEERING ANGLE 2 0

STEERING ANGLE 4 0

MANUAL
CASE 1 (0)
CASE 2 (90)
CASE 2 neg (-90)
CASE 1

MANUAL STEERING SETPOINT ANGLE 0.0

DISTANCE ERROR 0.00

AUTOMATIC SPEED
MANUAL VOLTAGE
MANUAL VOLTAGE

Manual Voltage 0

Figure 6.30 Stand-off distance controller HMI screen

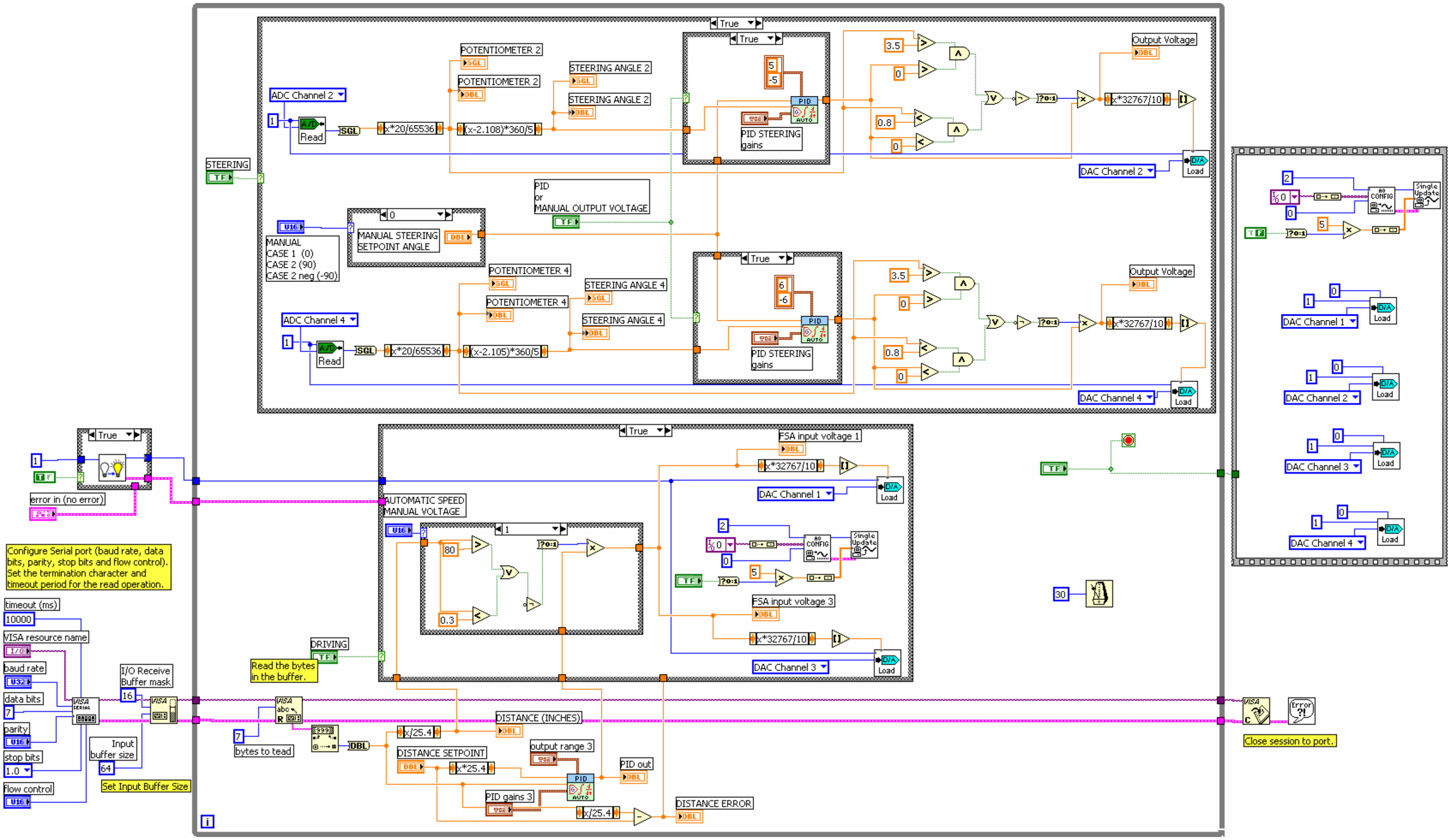

Figure 6.31 Stand-off distance controller LabView code

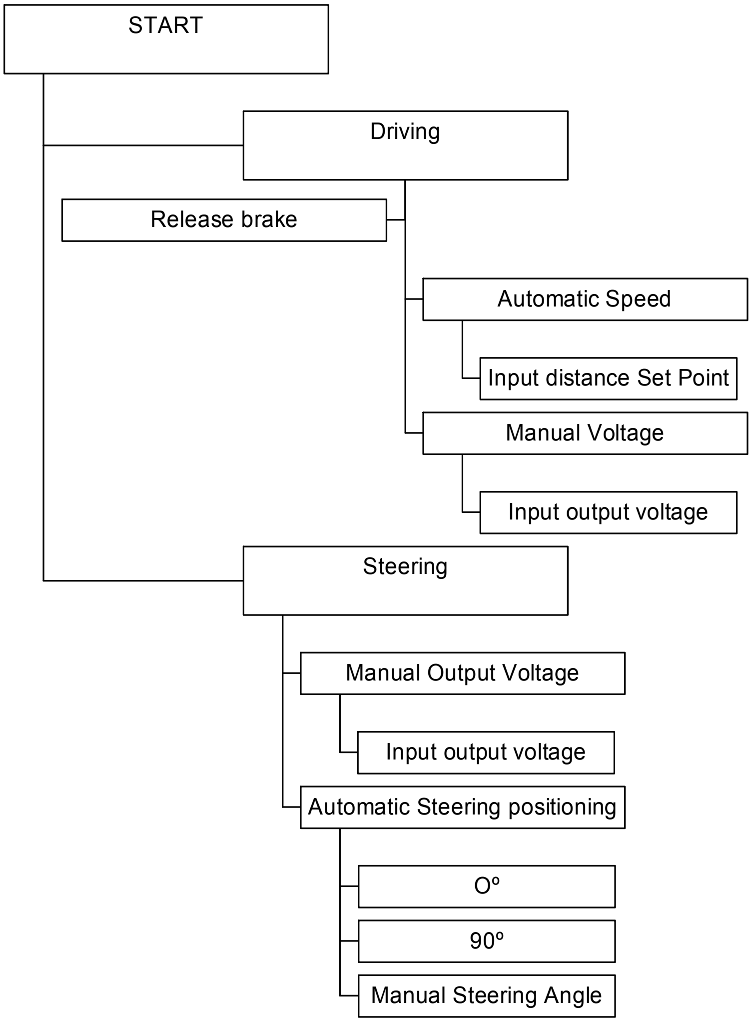

Figure 6.32 Stand-off distance controller operations chart

Chapter 7. Tests results

This chapter describes the tests developed with the tracking fluoroscope system to check the efficiency of the various tracking control algorithms. The first test is carried out to find the platform friction coefficient, C. The second section presents the translational mode tests results, which includes the second, third and fourth sets of tests. While the second and third tests are performed using the dynamic and kinematic algorithms developed in previous chapters, the fourth test uses stand-off distance control architecture. Finally, last test measures the performance of the platform setup algorithm that makes the platform rotate 90 degrees.

7.1 TEST PLANS

In the first test the platform is moved from point A to point B, 4.8 meters, as shown in picture 7.1. Various trials are done at diverse speeds and accelerations.

In the second, third and fourth tests a person walks from point A to point B and the platform follows the person keeping the tracking error as low as possible, as Figure 7.2 shows. The last test is the platform setup. The platform is automatically rotated 90 degrees and rotation precision is measured as showed in Figure 7.3.

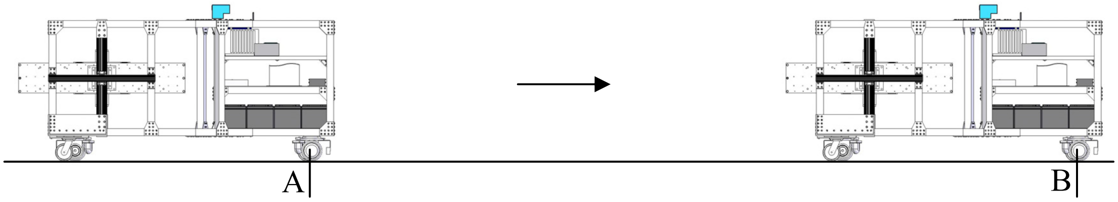

Figure 7.1 Friction test

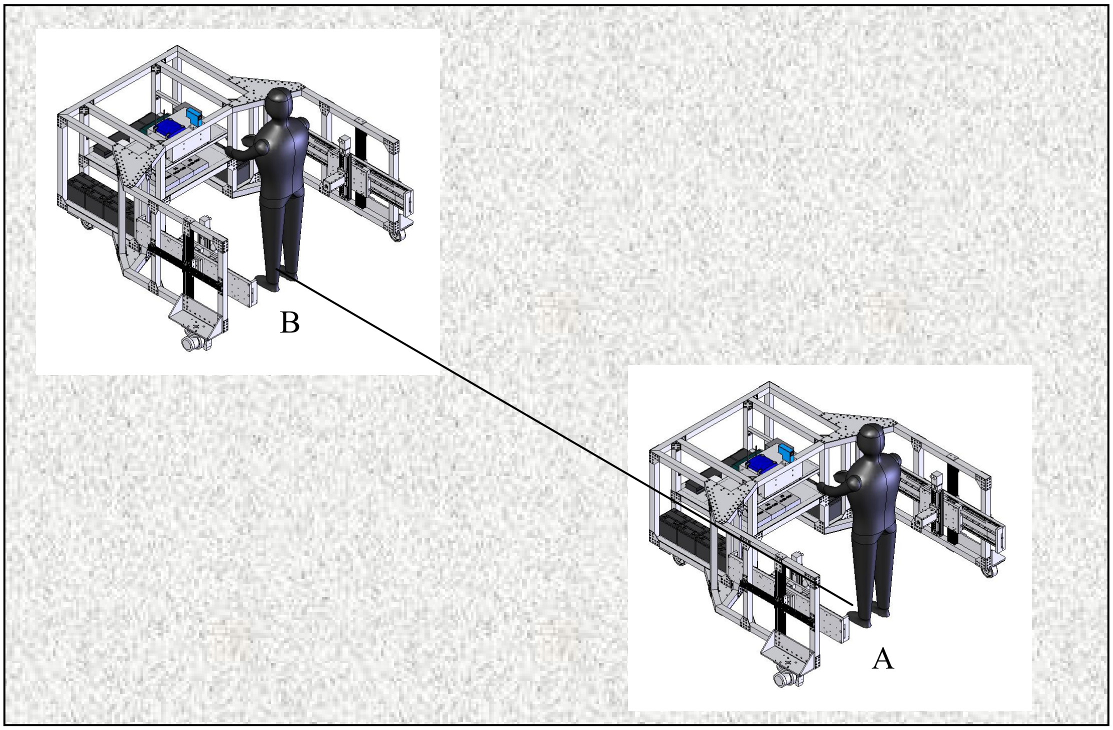

Figure 7.2 Tests of translational modes with kinematic and dynamic control

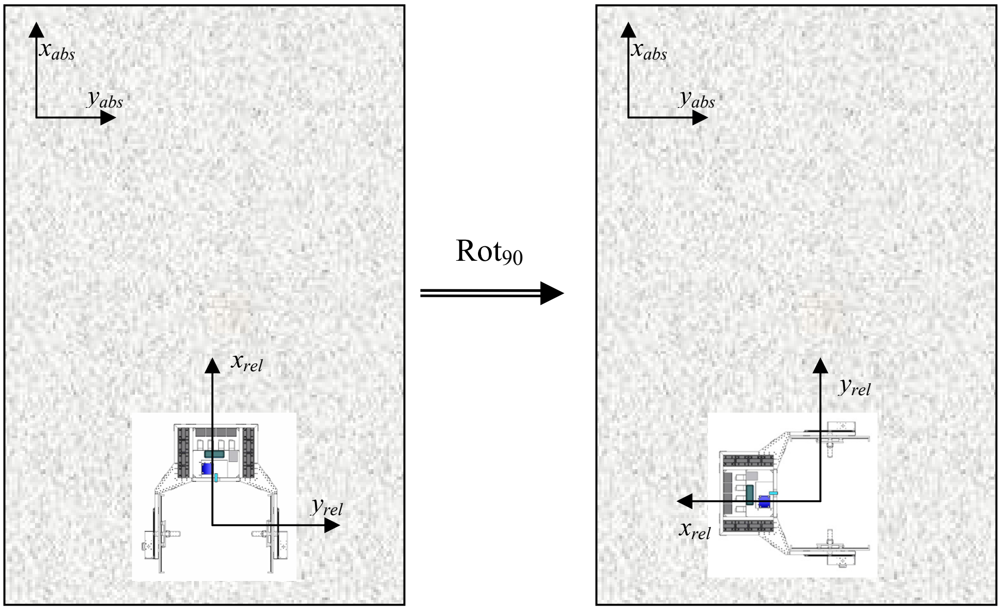

Figure 7.3 Platform Setup

7.2 FRICTION TEST

In this test the platform is moved with different speeds and accelerations in order to find out the friction coefficients. It was previously stated the relationship between the platform acceleration and platform slip is:

$$\begin{pmatrix} \dot{u} \\ \dot{v} \end{pmatrix} = \begin{pmatrix} \dfrac{F'_{1X} + F'_{3X}}{m} + \ddot{\theta} * L_{GC} + \omega^2 * F_{GC} - \omega * v \\ -\ddot{\theta} * F_{GC} + \omega^2 * L_{GC} + \omega * u \end{pmatrix} \qquad \text{Eq. 2.25}$$

In the case of null yaw rate and acceleration:

$$\begin{pmatrix} \dot{u} \\ \dot{v} \end{pmatrix} = \begin{pmatrix} \dfrac{F'_{1X} + F'_{3X}}{m} \\ 0 \end{pmatrix} \qquad \text{Eq. 7.1}$$

The friction model is represented by the next equation as previously addressed:

$$\begin{aligned} F_r &= \frac{-F_N * C * s}{S_{MAX}} && \mathit{for} \quad |s| < |S_{MAX}| \\ F_r &= -F_N * C * \operatorname{sgn}(V - \omega * RW) && \mathit{for} \quad |s| > |S_{MAX}| \end{aligned} \qquad \text{Eq. 3.10}$$

From this last equation and equation 7.1:

$$\dot{u} = \frac{-(F_{N1} * s_1 + F_{N3} * s_3) * C}{m * S_{MAX}} \qquad \text{Eq. 7.2}$$

Writing equation 7.2 in terms of C:

$$\boxed{C = \frac{-\dot{u} * m * S_{MAX}}{F_{N1} * s_1 + F_{N3} * s_3}} \qquad \text{Eq. 7.3}$$

Then if the platform slip is maintained in the linear zone, the friction coefficient C can be computed by equation 7.3. After measuring platform speed and acceleration, and both servomotor wheel speeds, the friction coefficient C is computed. The platform speed and acceleration are computed by differentiating distance measured by the scanner with respect to the time. Wheel-servomotor speeds are obtained from encoder readings. The objective of the test is to compute the value of the friction coefficient C and observe its variations as a function of the speed. Tests consist of moving the platform at various speeds and accelerations. Figure 7.4 shows C plots and mean values recorded and computed during the various tests.

It is worth mentioning that at every time during trials 2-6 the slip ratio was between 0.1 and -0.1. In the case of the first trial, the margins were larger, -0.30 to 0.30. Consequently, doing analogy with the plots presented at chapter 3, Figure 7.5 is built.

In simulations presented in chapter 5, a friction coefficient value of 0.4 was used based on the previous plot, since the subject walking speed was 0.5 m/s.

7.3 LINEAR TRANSLATIONAL MODE TEST RESULTS

The functional architectures previously addressed are tested for the linear translational mode. It is important that the control system be able to follow the person with a smooth movement. The performance of the control system is going to be evaluated by some quantitative and some qualitative indicators. Those indicators include the settling time, maximum error, steady state error, tracking error, platform rotation, spinning and sliding, and smooth movement. Settling time is defined here as the time needed by the control system to decrease the tracking error to below 0.1 meters. Steady state error is the tracking error before the subject starts walking, and the tracking error after the subject stops walking. Two facts are of fundamental significance, the first one is that the tracking dynamic error needs to be kept at small values, and the second one is that the platform movement must be smooth enough to the eyes of the walking subject.

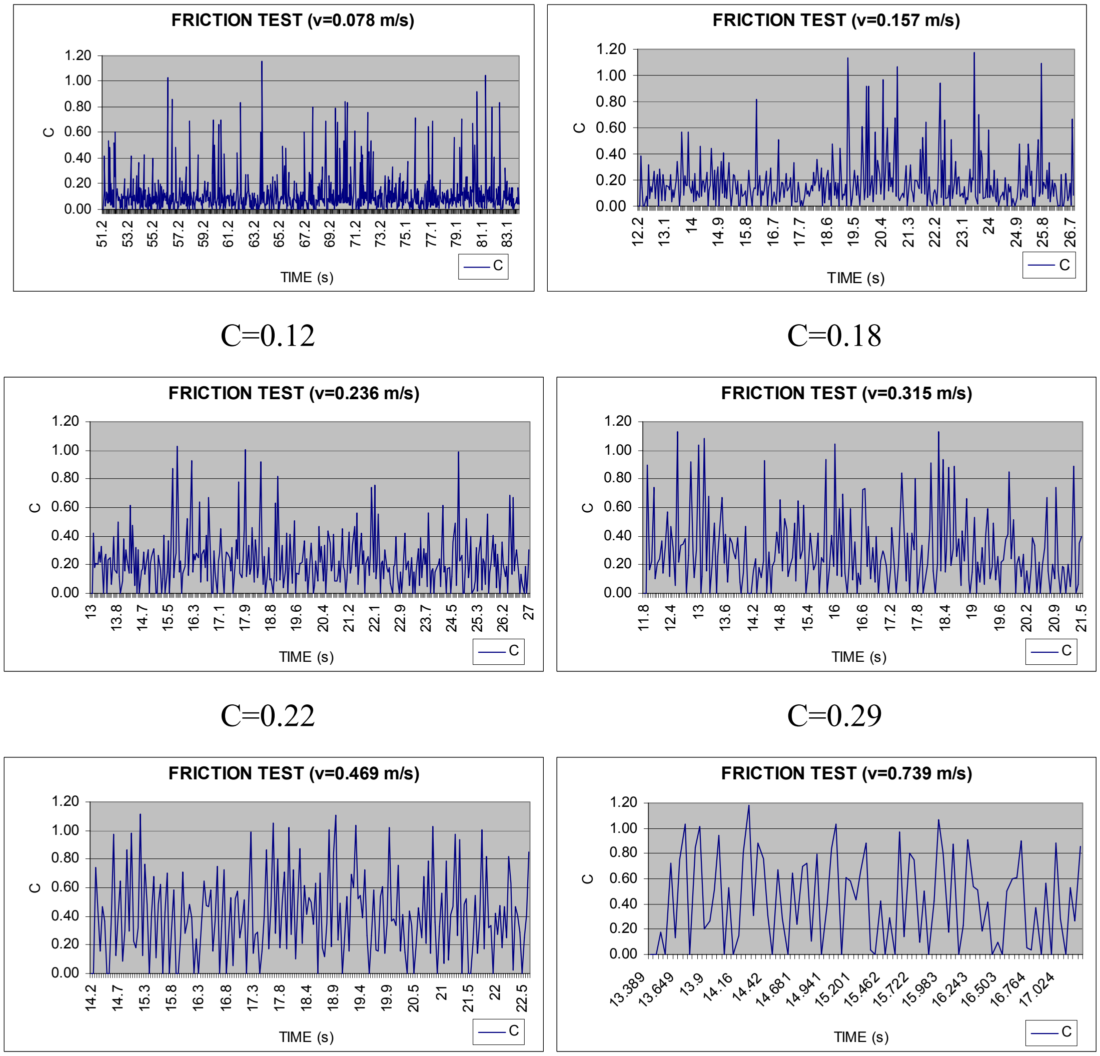

C=0.12

C=0.18

C=0.22

C=0.29

C=0.40

C=0.43

Figure 7.4 Friction test data

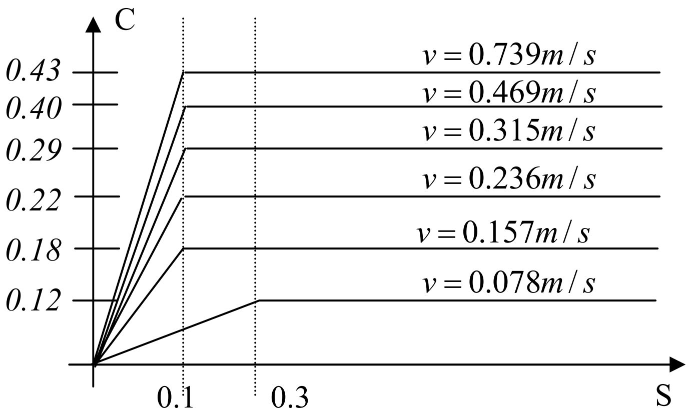

Figure 7.5 Friction coefficient

Finally, the settling time and the initial error are also significant since they affect the performance of the fluoroscope system at the initial steps of the subject.

7.3.1 Dynamic control

In this test the subject stands at point A, after some seconds he/she began walking for a distance of about 4.5 meters, and then he/she stops. Figures 7.6-7.9 show the system response using a controller parameter configuration with proportional gain, Kp=50, integral time Ti=0.01 and null derivative gain. Two tests were carried out with these parameters, the first one with a subject speed of about 0.55 m/s, and the second one at a subject speed of about 0.8 m/s.

The length of the room was an important disadvantage presented during the test since the subject can only walk for 4.5 meters from one wall to the other. This distance limits the ability to run the control system algorithm for more than a few seconds, especially at speeds greater than 0.5 m/s. During the test, it was observed that a subject's walking speed is not constant. This means that the test results are not directly comparable to the ones obtained with the simulation.

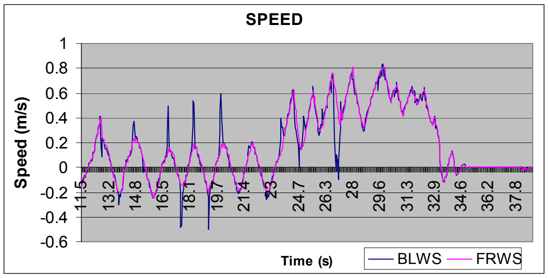

Figure 7.6 Wheels speed 1

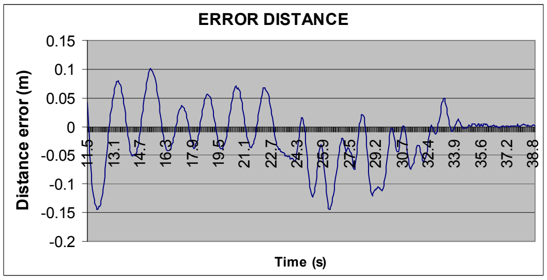

Figure 7.7 Tracking error distance 1

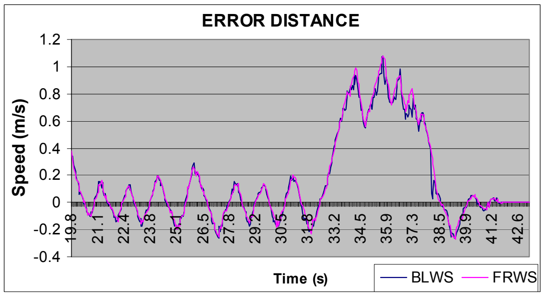

Figure 7.8 Wheels speed 2

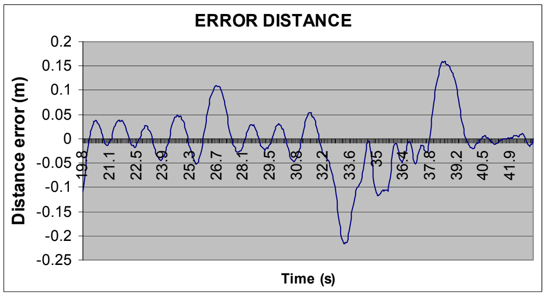

Figure 7.9 Tracking error distance 2

Figure 7.6 illustrates both servomotor wheel speeds and Figure 7.7 illustrates the tracking error generated during the test for a subject speed of 0.55 m/s. BLWS means back left wheel speed, while FRWS means forward right wheel speed.

Figure 7.8 illustrates both servomotor wheel speeds and Figure 7.9 illustrates the tracking error generated during the test for a subject speed of 0.8 m/s.

Some observations need to be discussed. Firstly, the greater the subject speed, the greater the initial tracking error and settling time. Secondly, while the subject is not walking, until time is 23 seconds in test 1 and time is 32 seconds in test 2, the platform oscillates with amplitude of 0.05 m and a frequency of about 1.4 s.

Thirdly, after the subject stops walking, at time = 33 seconds in test 1 and time = 38 seconds in test 2, the platform corrects the tracking error and the wheels also stop. This was not predicted in the simulation when to the friction model was utilized. The fourth observation, of special importance, is that slip in the form of sliding occurred to a lesser degree than when running the kinematic algorithm presented in the next section. Thus, the platform rotation generated by the sliding phenomenon is much smaller than when running the kinematic algorithm. Nevertheless, it was still appreciable. The settling time is the time required by the control system to reduce the error to small values. The fifth observation is that the settling time for the 0.55 m/s case was 1 second, while it was 1.5 seconds for the 0.8 m/s case. Finally, the tracking error after the settling time is mostly between 0.05 and 0.1 meters. The joint tracking algorithm can absorb this error, but improvements are still desirable.

7.3.2 Kinematic closed control loop

In this test the subject stands on point A. After some seconds he/she began walking for a distance of about 4.5 meters, and then he/she stops. Various tests were done to tune the system. The following figures show the system response using a controller parameter configuration with proportional gain, Kp=15, integral time Ti=0.005, and null derivative gain. Among various parameters configuration, this one was chosen for having a small settling time and minor steady state error. It is worth mentioning that in the kinematic closed loop control, the steady state error is not zero due to the presence of wheel slip at reduced speeds. Appendix C includes system response for other controller parameters configuration.

Figures 7.10 and 7.11 show that the control algorithm accomplishes its task of keeping tracking error at low values. Particularly, about two seconds after the person began walking, the tracking error is kept at values lower than 0.05 meters. However, it was observed that the wheel slipped during the tests. After subject has stopped, slipping causes the platform to move back and forth indefinitely.

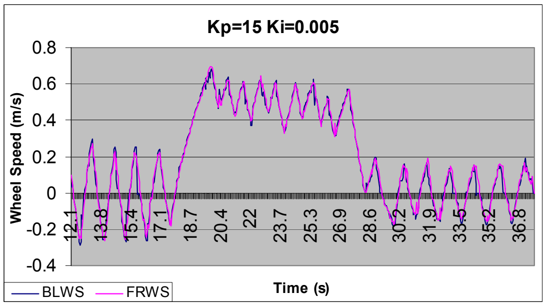

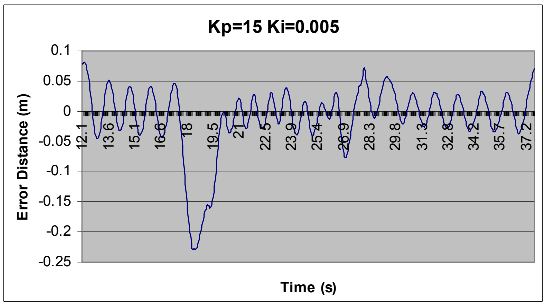

Figure 7.10 Wheels speed 3

Figure 7.11 Tracking error distance 3

This not only generates an oscillating tracking error, but also causes platform rotation. Slipping was greater in the rear left wheel than in the front right wheel due to the small friction force attributed to a reduced normal force. Slipping appeared in the form of spinning at low speeds when the tracking algorithm changes the wheel driving speed direction to reduce the tracking distance error to zero. In fact, the tracking algorithm changes speed much faster than platform stopping speed. For instance, when the platform is still going forward, the algorithm changes the rotational direction of the wheel and makes it go in reverse. The servo amplifiers vary the servomotor speeds quickly. However, the high platform inertia makes it decelerate slowly and spinning occurs. Limiting the controller output, controller output rate, and wheel acceleration would reduce this slipping phenomenon. However, this is a trade off since reducing them would also decrease the system performance, particularly by increasing tracking error while the person is walking. An adaptive controller, which adjusts gains depending on platform speed, could be a solution. An easier solution found, was to establish a control architecture that does not set the wheels' speed. This architecture's LabView code was presented in section 6.4.4, and is proposed and tested in the next section.

7.3.3 Stand-off distance controller

The test results presented in previous sections showed the system performance using the kinematic and dynamic control algorithms. While those tests showed acceptable performance, slipping was observed during the tests due to fast speed changes. Thus, it is observed that a control architecture, which does not fix the wheel servomotor speed, would not produce such fast changes. Stand-off distance control architecture with no speed control is proposed and tested in this section. The only different between this control architecture and the kinematic closed loop control architecture is that the speed loop is not closed. Figure 7.12 shows this control architecture, and it shows that the servomotor wheel feedback is not considered. The only feedback used by the system is the distance measured by the laser. Then, a voltage signal is sent to the FSA but motor speed is not controlled, and therefore left in open loop. Subsequently, this section tests the tracking fluoroscope system running with a stand-off distance control architecture.

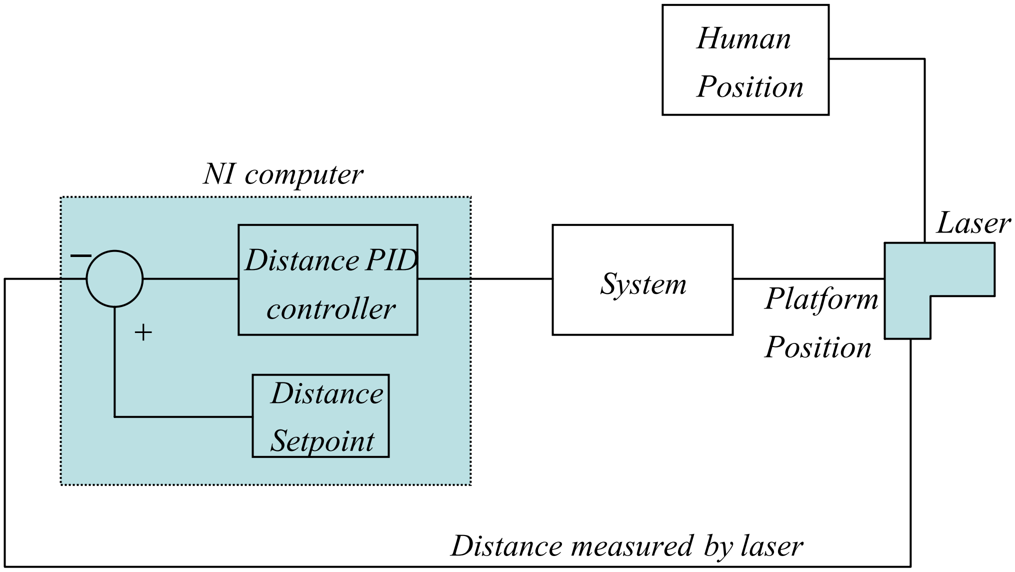

Figure 7.12 Stand-off distance controller

The control system was tuned varying the distance controller gains. After tuning the system, its response was checked for various subject speeds. The following figures show system response to various subject speeds. PID parameter configurations achieve the best results for the current control architecture. System response to similar tests carried out with different stand-off controller gains are presented in Appendix C.

The controller gains are:

Proportional gain Kp= 0.03
Integral time Ti= 0.015
Derivative time Td= 0.01

Three tests were performed with the current controller configuration. In the first one, the subject walks at a speed about 0.42 m/s and the motion card output signal is controlled between -5v and 5v. In the second test, the subject walks at a speed of about 0.36 m/s and the motion card output signal is controlled between -8v and 8v. Finally, in the last test the subject walks at a speed of about 0.63 m/s and the motion card output signal is again controlled between -8v and 8v.

Figures 7.12-7.21 show that this control architecture has improved response than the previous control algorithms. In the first and second tests, the error is always kept under 4 inches, then there is no settling time. Only in the last test is there a non-zero settling time of 1 second. In the other two tests, the error is never greater than 0.1 meters. The dynamic error is much smaller than with the other control algorithms. Furthermore, the steady state error is null and the maximum error is smaller than tests performed in previous sections. Spinning and sliding are not observed at low speeds, so no platform rotation exists. In addition, the platform movement was much smoother than with the other tracking control algorithms. Finally, a qualitative observation is that from the subject’s point of view, the platform feels more stable, comfortable, and safe than in both previous cases.

Test 1 (*v=0.42 m/s, 5,-5v*)

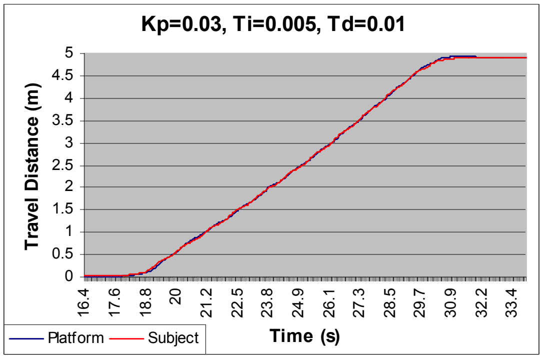

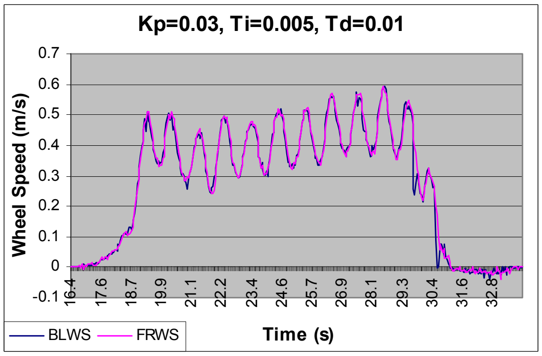

Figure 7.13 Travel distance 1

Figure 7.14 Wheels speed 4

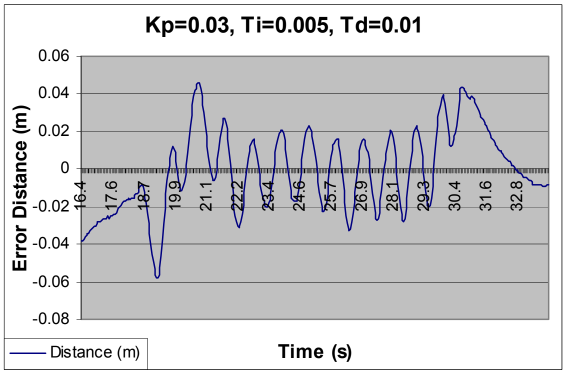

Figure 7.15 Tracking error distance 4

Test 2 (*v=0.36 m/s, 8,-8v*)

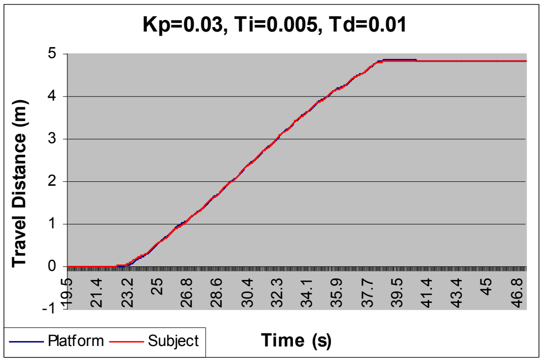

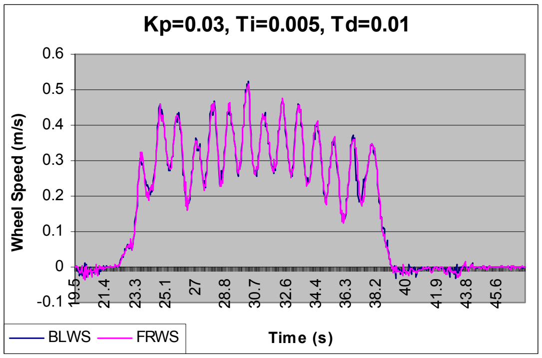

Figure 7.16 Travel distance 2

Figure 7.17 Wheels speed 5

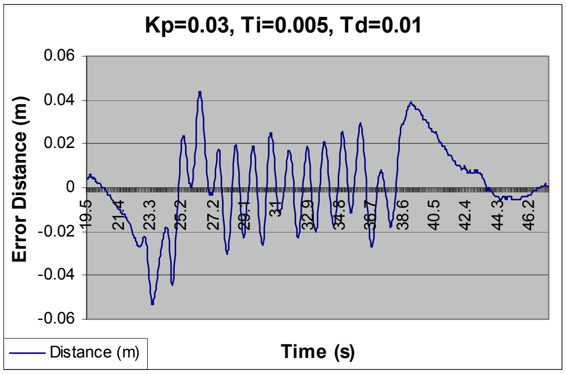

Figure 7.18 Tracking error distance 5

Test 3 (*v=0.63 m/s, 8,-8v*)

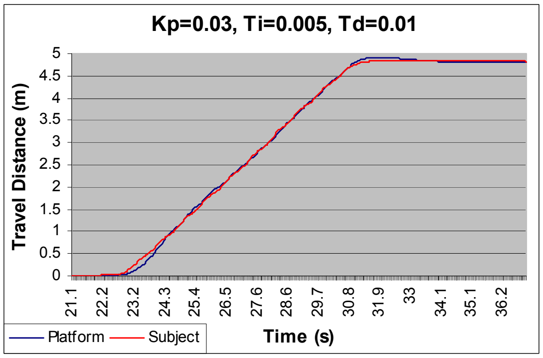

Figure 7.19 Travel distance 3

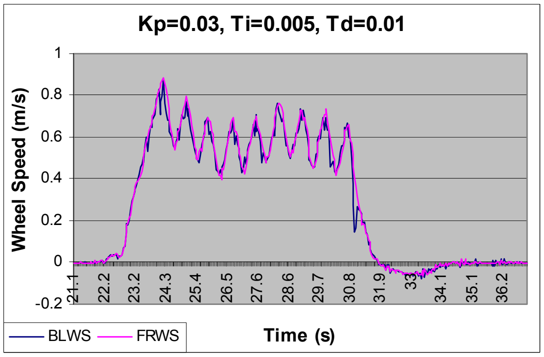

Figure 7.20 Wheels speed 6

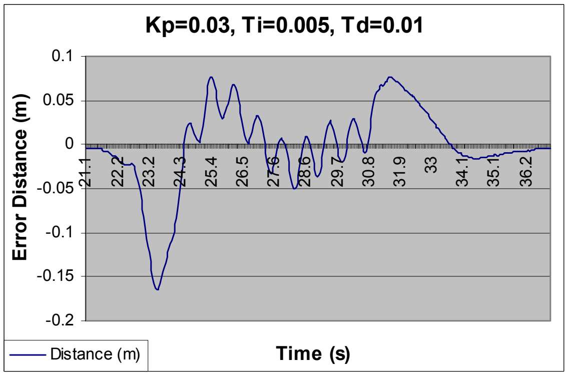

Figure 7.21 Tracking error distance 6

7.4 PLATFORM SETUP TEST

In this test the system ran the setup code presented in chapter 7. The platform rotated exactly 90 degrees in 7 seconds. However, due to small wheel slipping, the center of rotation, defined as the middle point between wheeled servomotors, suffered a translation of almost 10 inches with respect to its original position. The main objective of the platform setup was to rotate it 90 degrees to make it possible run the platform in the longest room dimension or corridor direction. Therefore, this small translation does not affect tests performance. There are, however, various solutions to reduce the center of rotation translation that can be explored in future work. For example, wheel position control and wheel speed control can be applied. Also, the output signal voltage of the motion card can be saturated or the wheel steering angle could be varied.

Chapter 8. Conclusions and future work

8.1 CONCLUSION

The objective of this thesis was to determine the best control architecture and control algorithm for the Tracking Fluoroscope System. To accomplish that objective, this thesis presented the kinematic and dynamic models of the tracking fluoroscope system for the free and for the translational motion modes. Both models were developed, simulated and tested for the translational motion mode. The kinematic model was based in the rigid body calculations, while the dynamic model incorporated a tire friction model that calculates the friction force in function of the wheel slippage. A platform setup algorithm for the platform rotation was also presented and tested. During that test, the platform rotated exactly 90 degrees in 7 seconds.

Simulation carried out in Simulink predicted that the kinematic and dynamic control system would keep the tracking error at values smaller than 0.15 m. Simulations showed steady state error, after the subject stops walking, produced by a deficiency of the friction model at null speed neighborhoods.

Several tests were implemented to study the system response. First, the platform friction coefficient, C, was determined. A series of tests were carried out at various speed and platform accelerations to compute the value of C. During the tests, the slip remained at low values, and then the friction force was always in its linear region.

Secondly, the dynamic control system was tested. The control system reduced sliding and spinning with respect to the kinematic control system. However, not all sliding and spinning was eliminated; platform rotations continued to a limited extent. The settling time for the algorithm is on the order of 1.5 seconds, but it depends slightly on the subject speed. The initial steady state error is around 0.05 meters, and the final steady state error is null, contrasting the steady state errors predicted in its simulation. The tracking error (error after the settling time) has peaks of about 0.1 meters but it is usually around 0.05 m/s. Finally, the maximum error for speeds of 0.8 m/s is 0.2 meters, while for medium speeds of 0.4 m/s is 0.15 meters.

A third set of tests was completed using the kinematic control system. This control architecture exhibited high sliding and spinning at null subject speed. This condition induced a platform alternate movement combined with platform rotation. The settling time for this algorithm is 2 seconds. The initial and final steady state errors were in the order of 0.05 meters. Furthermore, the maximum error was worse than the dynamic case, about 0.22 meters. Despite these disadvantages, this algorithm exhibits better performance than the dynamic control observed in other indicators. For example, the tracking error is smaller than the one obtained by dynamic control, and its peaks never surpass 0.05 m.

Finally, even though dynamic and kinematic control systems showed satisfactory results, a stand-off distance controller was introduced to overcome the disadvantages presented by these control systems. The stand-off distance controller showed no sliding or spinning unless high speeds were combined with sudden stops. Neither platform oscillations nor platform rotation were observed. The settling time was null for small speeds since the error is always below 0.02 meters, which showed the great performance of the algorithm. For higher speeds, the algorithm had a settling time of 1 second. The initial and final steady state errors were insignificant. The tracking error for high speeds was smaller than the dynamic and kinematic speed closed loop algorithms and its peaks never overcome 0.05 meters. The maximum error for high speeds was 0.15 meters, while for reduced speeds it was 0.05 meters. This method seems to be more stable and smoother than the other control schemes from the subject point of view. In conclusion, the stand-off controller scheme showed enhanced performance, and it is the preferred control method for use at TFS.

8.2 FUTURE WORK

The future work can be directed in two main areas—improvement for current systems, and expansion to a new free motion control system. For the current stand-off controller system, no straight-forward implementation is necessary since its results are remarkable. However, if the results obtained by the dynamic and kinematic control systems require enhancement, various improvements may be implemented for those control systems.

First, a wheel friction test under controllable conditions would give an accurate friction model of the motor-in-wheel units, and subsequently improving the dynamic model. Also related to that, better traction properties at the wheel would strongly increase the performance since current units have low friction/traction properties. Another improvement that can be done related to the friction force is to equalize the wheel normal force. Normal force at the wheels is currently unbalanced since the weight distribution cannot be varied from back to forth. To solve this situation, the motor can be dissembled, and then the plate that holds them to the platform can be machined to reduce its thickness.

Second, replacing the old free wheel, used in the dynamic control system test to measure the platform speed, would improve dynamic control system performance, since its encoder signal was not very consistent.

The third option for system improvements would be the inclusion of two controlling tools to eliminate the steady state errors. The incorporation of an adaptive controlling strategy would reduce them. Varying distance controller’s gains at low speeds and low tracking error, respect to the distance controller’s gains at high speeds, can definitively minimize the steady state errors, also minimizing the settling time. This process was manually done by decreasing the controller gains when the platform was moving back and forth, and the platform stopped. In addition, the inclusion of a slip observer would increase system performance since that real time information could be used to modify speed commands being sent to the drivers.

In fourth point, a complete dynamic model considering lateral wheel forces and caster wheel models will provide a better understanding of the system dynamics. It is worth mentioning that to carry out that control system, potentiometers and encoders will need to be installed at the caster wheels.

Finally, for the free motion mode implementation, an orientation gauge device needs to be integrated to the TFS. Various devices can be used to measure the orientation between the platform and the subject. Among them, the laser scanner and the stereo vision camera are the most plausible. The kinematic and dynamic system equations developed for free motion mode in chapter 2, only need to be integrated with the platform orientation and stand-off distance controllers.

References

[1] J. C. Alexandery J. H. Maddocksz; “On the Kinematics of Wheeled Mobile Robots”, Int. J. Robotics Res., vol. 8, No. 5, pp. 15-27, Aug. 1989.

[2] Johann Borenstein; “Control and Kinematic Design of Multi-Degree-of-Freedom Mobile Robots with Compliant Linkage”, IEEE Transactions on Robotics and Automation, Vol. 1 I , No. 1. Feb. 1995

[3] G. Campion, G. Bastin, B. D’ AndrCa-Novel, “Structural Properties and Classification of Kinematic and Dynamic Models of Wheeled Mobile Robots”, IEEE Transactions on Robotics and Automation, Vol. 12, No. 1, Feb. 1996

[4] R. Rajagopalan; “A Generic Kinematic Formulation for Wheeled Mobile Robots”, Journal of Robotic Systems 14(2), 77–91 (1997)

[5] R. L Williams, B.A. Carter, P Gallina and G Rosati; “Dynamic Model With Slip for Wheeled Omnidirectional Robots”, IEEE Transactions on Robotics and Automation, Vol. 18, NO. 3, June 2002

[6] John Van de Vegte; “Feedback Control Systems”, Third edition

[7] J. Yi, L. Alvarez, X. Claeys, R. Horowitz, “Emergency Braking Control with an Observer-based Dynamic Tire/Road Friction Model and Wheel Angular Velocity Measurement”, Vehicle System Dynamics 2003, VOL. 39, NO. 2, pp. 81-97

[8] S. Solyom, A. Rantzer, J. Ludemann, “Synthesis of a Model-based Tire Slip Controller ”, Vehicle System Dynamics 2004, VOL. 41, NO. 6, pp. 475-499

[9] C. Canudas-De-Wit, P. Tsiotras, E. Velenis, M. Basset, G. Gissinger, “Dynamic Friction Models fro Road/Tire Longitudinal Interaction”, Vehicle System Dynamics 2003, VOL. 39, NO. 3, pp. 19-226

[10] H. B. Pacejka; “Tyre models for Vehicle Dynamics Analysis”, Proceeding 1st International Colloquium on Tyre Models for Vehicle Dynamics Analysis, Oct. 1991

Appendixes

Appendix A - Unique rigid body yaw rate.

To show that the yaw rate of a rigid body is unique, let consider the acceleration of a point P of the rigid body and the acceleration of the center of gravity of the rigid, CG. The yaw rate at points P and CG, ω_P and ω_{CG} respectively, are assumed dissimilar. The vector d is the one that goes from CG to P as Figure A.1 shows.

$$\vec{a}_P = \vec{a}_{CG} + \dot{\vec{\omega}}_{CG} \times \vec{d} + \vec{\omega}_{CG} \times \left(\vec{\omega}_{CG} \times \vec{d}\right)$$

$$\vec{a}_{CG} = \vec{a}_P + \dot{\vec{\omega}}_P \times \left(-\vec{d}\right) + \vec{\omega}_P \times \left(\vec{\omega}_P \times \left(-\vec{d}\right)\right)$$

Combining last equations

$$\vec{a}_P = \vec{a}_P + \dot{\vec{\omega}}_P \times \left(-\vec{d}\right) + \vec{\omega}_P \times \left(\vec{\omega}_P \times \left(-\vec{d}\right)\right) + \dot{\vec{\omega}}_{CG} \times \vec{d} + \vec{\omega}_{CG} \times \left(\vec{\omega}_{CG} \times \vec{d}\right)$$

Operating

$$0 = \left(\dot{\vec{\omega}}_{CG} - \dot{\vec{\omega}}_P\right) \times \vec{d} - \vec{\omega}_P \times \left(\vec{\omega}_P \times \vec{d}\right) + \vec{\omega}_{CG} \times \left(\vec{\omega}_{CG} \times \vec{d}\right)$$

Doing the cross product at the last two terms of the right side of last equation:

$$\vec{\omega}_P \times \left(\vec{\omega}_P \times \vec{d}\right) = -\omega_P^2 * \vec{d}$$

$$\vec{\omega}_{CG} \times \left(\vec{\omega}_{CG} \times \vec{d}\right) = -\omega_{CG}^2 * \vec{d}$$

Replacing them in the previous equation

$$0 = \left(\dot{\vec{\omega}}_{CG} - \dot{\vec{\omega}}_P\right) \times \vec{d} + \left(\omega_P^2 - \omega_{CG}^2\right) * \vec{d}$$

Since vectors of last equation are in different directions:

$$0 = \left(\dot{\vec{\omega}}_{CG} - \dot{\vec{\omega}}_{P}\right) \times \vec{d}$$

$$0 = \left(\omega_P^2 - \omega_{CG}^2\right) * \vec{d}$$

Finally, since d is not null

$$\dot{\omega}_{CG} = \dot{\omega}_P$$

$$\omega_{CG} = \omega_P$$

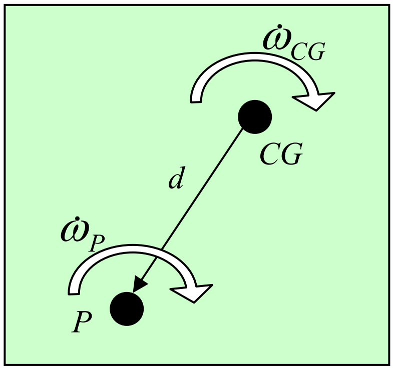

Figure A.1 Rigid body and points acceleration

Appendix B - Electric circuit model for field-controlled DC servomotor

This chapter presents the electric circuit model for field-controlled dc servomotor, as an extension of the armature-controlled dc servomotor model presented in chapter 3. Table B.1 includes servomotor parameters showed by Figure B.1.

Applying the first Kirchoff law to the electric circuit:

$$V_f = L_f * \frac{di_f}{dt} + R_f * i_f \qquad \text{Eq. B.1}$$

For a constant armature voltage, the torque developed by the dc servomotor is directly proportional to the current, then:

$$\boxed{T = K_t * i_f} \qquad K_t \text{ is the motor torque constant} \qquad \text{Eq. B.2}$$

Table B.1 Field-controlled motor model

R_f is the motor field resistance	i_f is the motor field current
L_f is the motor field inductance	V_f is the input motor field voltage

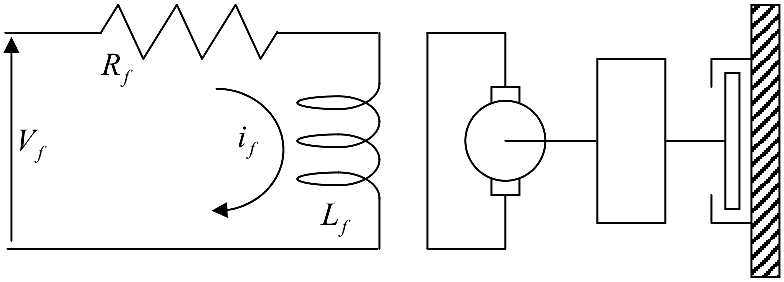

Figure B.1 Field-controlled motor model

Substituting i_f in Eq. B.1 by Eq. B.2;

$$V_f = \frac{L_f}{K_t} * \frac{dT}{dt} + \frac{R_f * T}{K_t}$$

Figure B.2 shows the Simulink model of a field-controlled DC servomotor. Figure B.3 includes both, motor and load models together in a single Simulink diagram.

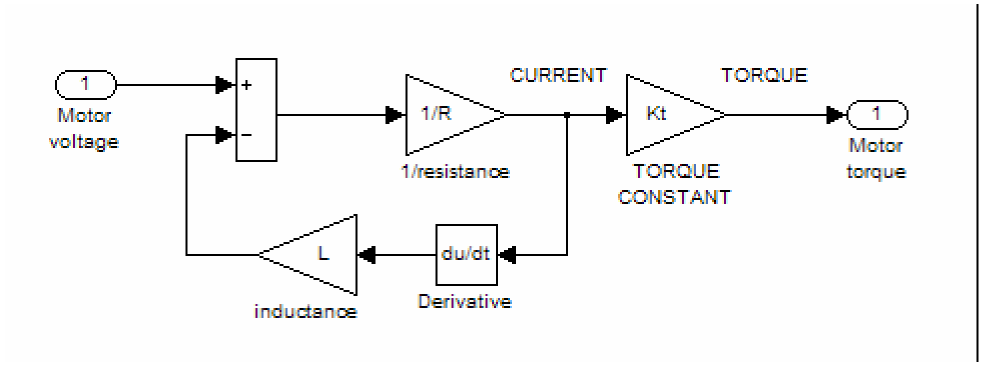

Figure B.2 Simulink Field-controlled motor model

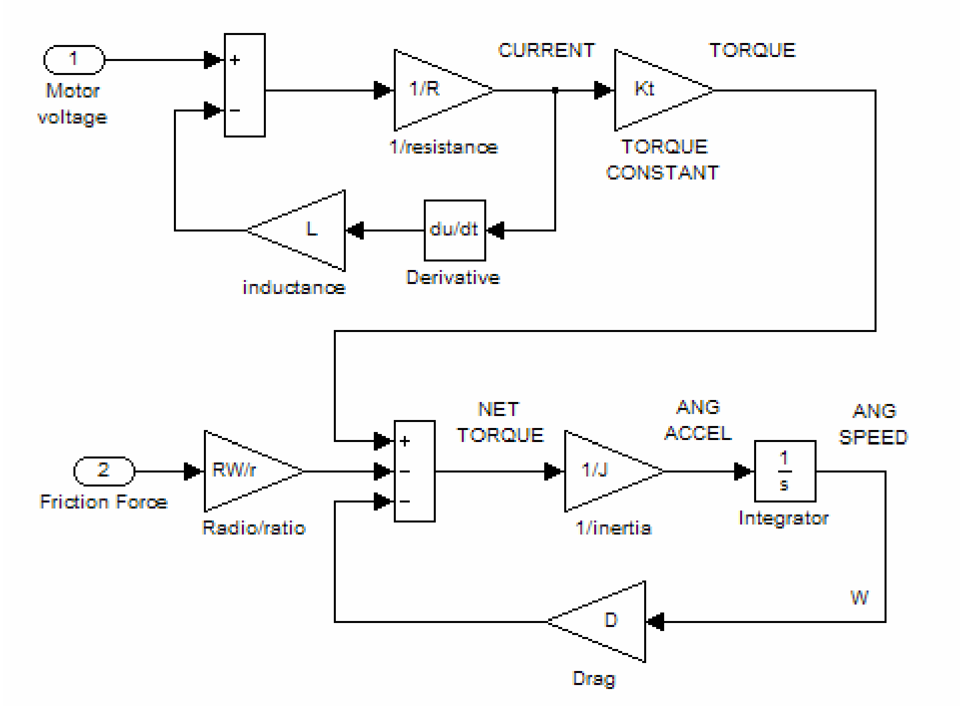

Figure B.3 Simulink Field-controlled motor + load model

Appendix C – Test results for additional controller parameters

This appendix includes several controller parameters configuration for the control model proposed, showing the system response to diverse subject speeds. Figures C.1 to C.18 show the system response for various controller parameters configuration.

- Kinematic close control loop

Kp=5 Ki=0.01 Kd=0.001

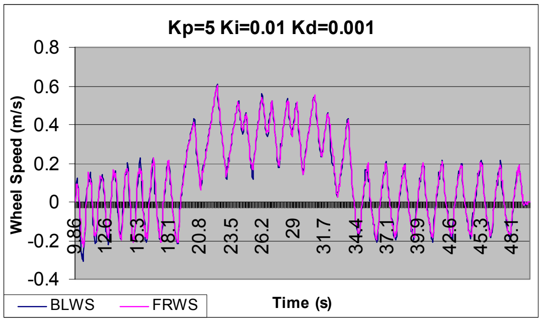

Figure C.1 Wheels speed 7

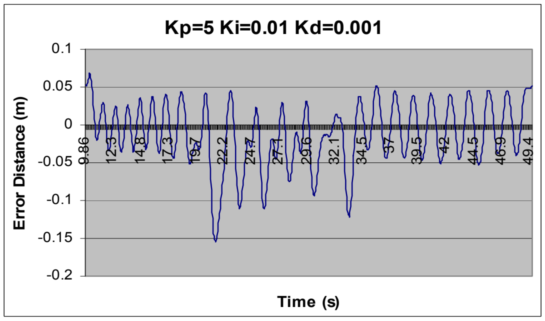

Figure C.2 Tracking error distance 7

Kp=20 Ki=0.01 Kd=0.001 (Increasing Kp respect to last test)

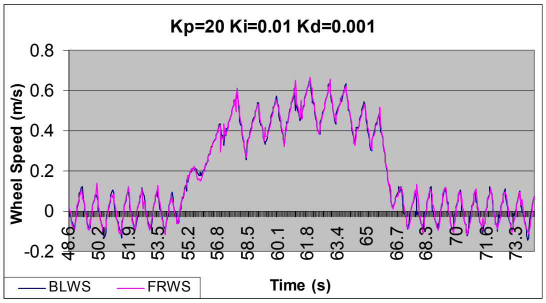

Figure C.3 Wheels speed 8

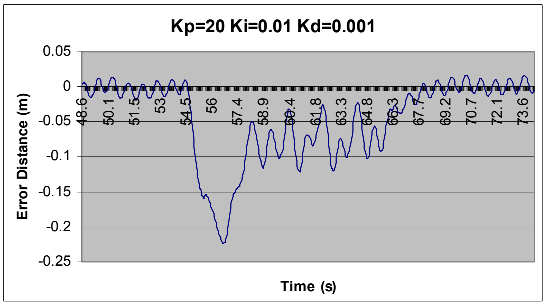

Figure C.4 Tracking error distance 8

Kp=15 Ki=0.001 Kd=0.001 (Decreasing Ki and Kp respect to last test)

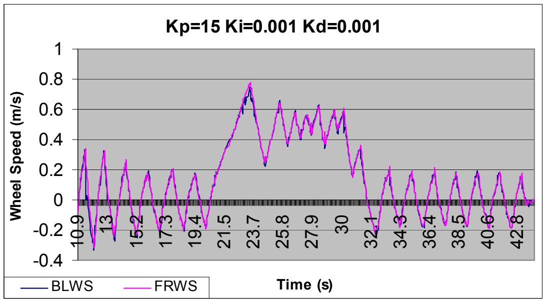

Figure C.5 Wheels speed 9

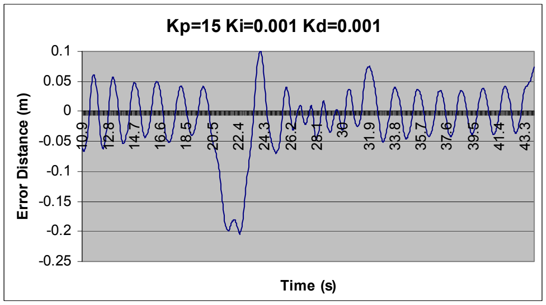

Figure C.6 Tracking error distance 9

Kp=15 Ki=0.005 Kd=0.001 (Increasing Ki respect to last test)

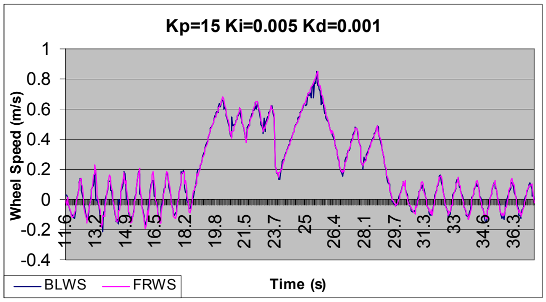

Figure C.7 Wheels speed 10

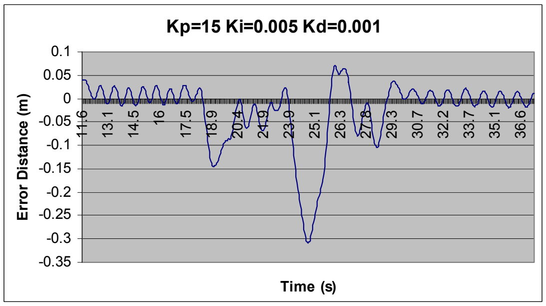

Figure C.8 Tracking error distance 10

- Stand off controller

Kp=0.03 at slow speed

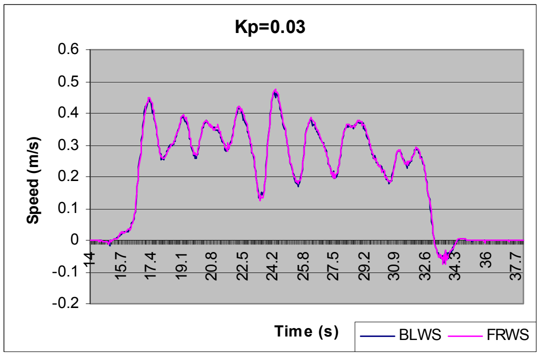

Figure C.9 Wheels speed 11

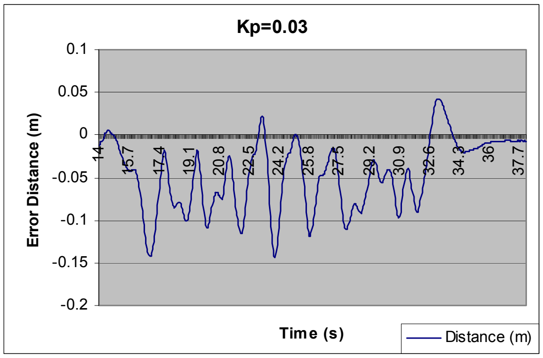

Figure C.10 Tracking error distance 11

Kp=0.03 at higher speed

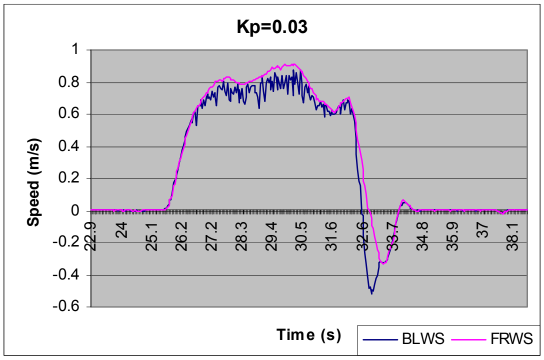

Figure C.11 Wheels speed 12

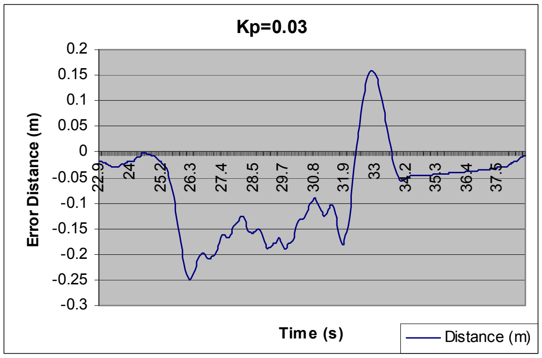

Figure C.12 Tracking error distance 12

KP=0.03 KI=0.01 at high speed

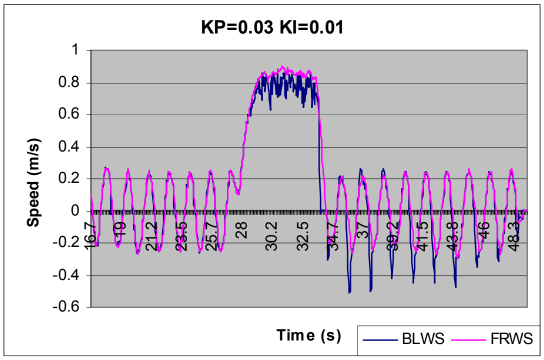

Figure C.13 Wheels speed 13

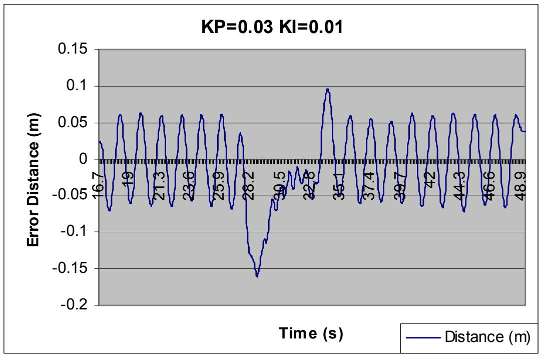

Figure C.14 Tracking error distance 13

KP=0.03 KI=0.001 KD=0.01 at medium speed

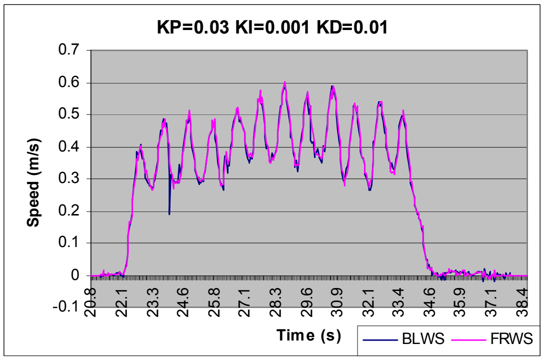

Figure C.15 Wheels speed 14

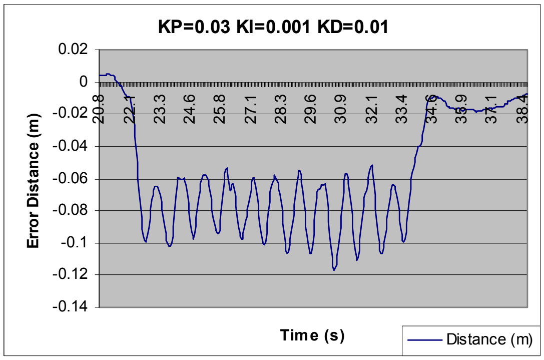

Figure C.16 Tracking error distance 14

KP=0.03 KI=0.001 KD=0.01 at higher speed

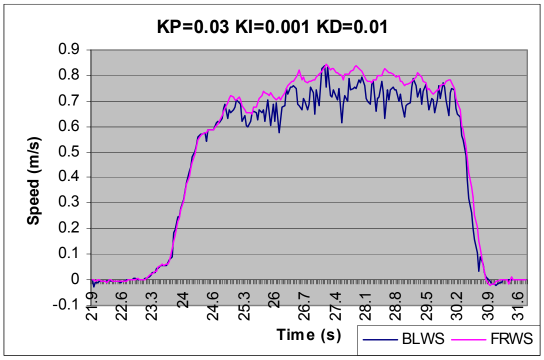

Figure C.17 Wheels speed 15

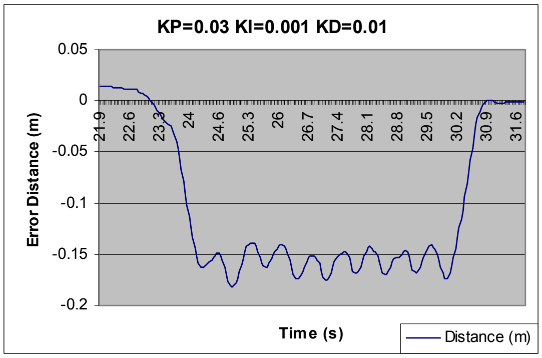

Figure C.18 Tracking error distance 15

Vita

Gabriel Preliasco was originally born in Montevideo, Uruguay in 1978. He grew up in a typical neighborhood of Montevideo, where children spend the whole day playing at the sidewalks or parks after school. Being young his mother, teacher, and father, mechanic, taught him about the responsibilities of each person has inside and outside of her/his house. He attended to the primary public school system. In the third year of the high school, he switched from the public high school system to one of the best private schools. He did the college at the same institution and after that he enrolled at the Universidad de la República that is the public university and the best one too. He finished his dual Industrial/Mechanical Engineering degree with the best class grades. Before graduating he worked as teacher grade 1 for the quality control course. He did his internship in Circular, the Rockwell system integrator for Uruguay, where he was afterward hired during his last undergraduate year. He worked in that company until he got the Fulbright scholarship and others to do his graduate studies at the United States of America. Gabriel got married in December 2003, and he is currently finishing his Masters of Science in Mechanical Engineering at the University of Tennessee.